Energy Reports 8 (2022) 5820–5851

Contents lists available at ScienceDirect

Energy Reports

journal homepage: www.elsevier.com/locate/egyr

Review article

Review on two-terminal and four-terminal crystalline-silicon/perovskite tandem solar cells; progress, challenges, and future perspectives

Ehsan Raza [a,b], Zubair Ahmad [a,*]

[a] Qatar University Young Scientists Center (QUYSC), Qatar University, 2713, Doha, Qatar
[b] Department of Electronics, University of Peshawar, 25120, Peshawar, Pakistan

ARTICLE INFO

Article history:
Received 9 July 2021
Received in revised form 26 March 2022
Accepted 7 April 2022
Available online xxxx

Keywords:
Perovskite solar cells
Crystalline silicon solar cells
Shockley–Queisser limit
Two terminal silicon/perovskite tandem solar cells
Four terminal silicon/perovskite tandem solar cells
Power conversion efficiency

ABSTRACT

Silicon (Si) solar cells are the dominant and well-developed solar technology holding more than 95% share of the photovoltaic market with efficiencies over 26%. Still, this value is far away from the Shockley–Queisser limit of 33.15% for single-junction devices. A prominent way to surpass this limit and boost the device performance is to combine different bandgap materials in a tandem configuration. The rapid emergence of perovskite solar cells (PSCs) as one of the most exciting research fields with over 25% efficiency has attracted the focus of the scientific community. The solution-processability, bandgap tunability, and outstanding optoelectronic properties of perovskites mark them a potential pair with silicon to develop tandem solar cells (TSCs). In nearly seven to eight years of development, Si/perovskite TSCs have achieved record certified efficiencies of over 29%. This review emphasizes on two and four-terminal Si/perovskite TSCs. Initially, the advancement of efficiencies to date is discussed, including a comparison of numerous perovskite and silicon material choices. Then, the evolution of PSCs with Si (homojunction and heterojunction) bottom devices and their impact on the performance of TSCs is summarized. The suitable candidates for the perovskite and Si cells are proposed for Si/perovskite TSCs. Next, factors influencing the performance of tandems, such as fabrication issues on textured surfaces, parasitic absorption, reflection losses, nonideal perovskite absorber layer bandgap, device instability, and large-area fabrication, are highlighted. To reduce the electrical and optical losses for highly efficient tandems, an investigation of anti-reflecting coatings, current matching mechanisms, transparent electrodes, and recombination layers is discussed. Finally, based on these findings, future guidelines are proposed to boost the efficiencies beyond 30%. To the best of our knowledge, this is the first detailed study on two and four-terminal Si/perovskite TSCs. These findings would open new avenues for the research community with detailed information on Si/perovskite tandem cells.

Contents

* Corresponding author.
E-mail address: zubairtarar@qu.edu.qa (Z. Ahmad).

https://doi.org/10.1016/j.egyr.2022.04.028

1. Introduction

Harvesting solar energy and providing sustainable, clean, and green energy to the world at low cost is one of the most promising strategies for environment-friendly energy generation. In recent decades, the emergence of photovoltaic (PV) technology has paved the way towards green alternatives to fulfill the energy demands with the fastest growing market and dramatically decreasing costs. However, this technology is not the most widely used as a primary electrical energy source due to the limited energy conversion efficiency, large covering area, and higher overall system cost than traditional non-renewable energy resources (Sahin et al., 2007; Rau et al., 2014; Alharbi and Kais, 2015; Hossain et al., 2019). Though, during the past 10 years, the overall cost of PV systems (production, installation, and maintenance) has been reduced drastically (Hossain et al., 2019).

Currently, the PV market is dominated by single-junction crystalline silicon (c-Si) based solar technology for many reasons such as non-toxic behavior, earth abundancy, and good reliability of silicon material and mature manufacturing technology processes (Battaglia et al., 2016; Werner et al., 2018). In two decades, single-junction c-Si-based solar cells demonstrated almost stable behavior in energy conversion efficiency (with a minimal increase), i.e., 24.7% in 1999 (Zhao et al., 1999) to over 26% (Single-crystal, non-concentrator) in 2017 (Yoshikawa et al., 2017a,b). Furthermore, these efficiencies from single-junction silicon-based solar cells are bounded by theoretical Shockley–Queisser (SQ) limit of 29.4% for c-Si (Richter et al., 2013) and 33% (Shockley and Queisser, 1961) for single-junction solar cells. Two main factors that limit the performance of single-junction solar cells are: the non-absorbance of photons having energies lower than the bandgap and thermalization losses. To achieve the SQ limit and harvest a maximum number of photons efficiently, various approaches have been adapted. One of the strategies is to integrate absorber materials having different bandgaps in a multi-junction structure. The simplest method, which involves combining a high bandgap material on top of a low bandgap material, is called tandem structure.

In tandem structure, high bandgap material is used as a top sub-cell to absorb high energy (short wavelength) photons, while low bandgap material is used as a bottom sub-cell to absorb low energy (high wavelength) photons transmitted through the top sub-cell. This process allows a maximum number of photons to be harvested by utilizing a broad solar spectrum. For the bottom subcells, c-Si solar cells are ideal candidates due to their cost-competitive manufacturing based on their market dominance, high open-circuit voltage (V_{oc}) of up to 0.75 V (Taguchi et al., 2013), high efficiency (Yoshikawa et al., 2017a,b), and suitable bandgap (1.1 eV) (Werner et al., 2018). Various materials have been proposed and employed in the quest for the top subcell, such as III–V class semiconductors, because of their high efficiency and tunable bandgap. By combining GaAs and GaInP from III–V semiconductors as top sub-cell with c-Si bottom sub-cell, efficiency > 32% (Cariou et al., 2018) has been recently reported in dual junction configuration. In addition, triple junction configuration based on dual junction GaAs/GaInP as top sub-cell and c-Si as bottom sub-cell have demonstrated over 35% efficiency (Essig et al., 2017). However, high manufacturing costs related to III–V class semiconductors limit their deployment towards space-based applications such as satellites or high-concentration photovoltaic systems (Yamaguchi et al., 2018). A suitable replacement for III–V class semiconductors was proposed with the emergence of perovskite solar cells (PSCs).

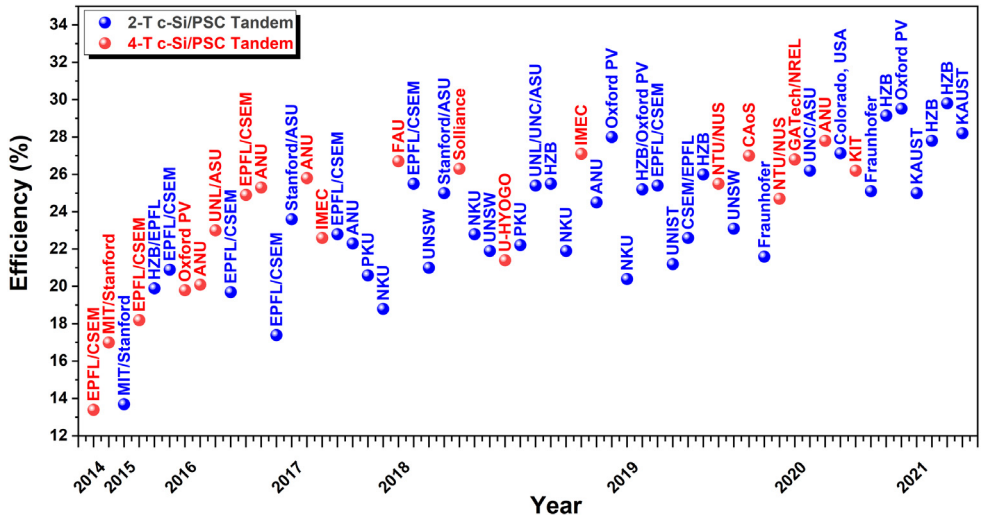

Fig. 1. Variation in Efficiency values of 2-T and 4-T c-Si/per TSCs with respect to reported time and the contribution of the Universities/ Research Institutes. ANU: The Australian National University; ASU: Arizona State University; CSEM: Swiss Centre for Electronics and Microtechnology; CAoS: Chinese Academy of Sciences; EPFL: École polytechnique fédérale de Lausanne; FAU: Friedrich-Alexander University; GATech: Georgia Institute of Technology; HZB: Helmholtz-Zentrum Berlin; IMEC: Interuniversity Microelectronics Centre; KIT: Karlsruhe Institute of Technology; MIT: Massachusetts Institute of Technology; NKU: Nankai University, China; NREL: National Renewable Energy Laboratory; NTU: Nanyang Technological University; NUS: National University of Singapore; PKU: Peking University; UNSW: University of New South Wales; UNL: University of Nebraska-Lincoln; U-HYOGO: University of Hyogo, Japan; UNIST: Ulsan National Institute of Science and Technology; UNC: University of North Carolina, USA; KAUST: King Abdulaziz University of Science and Technology.

Perovskites are semiconducting materials with the general formula ABX_3, where A is a cation, B is an anion, and X is a halide. These materials are considered highly promising absorber materials for next-generation solar cells. PSCs have attracted massive attention from the research community due to the abrupt increase in power conversion efficiency (PCE) from 3.81% in 2009 (Kojima et al., 2009; Chu et al., 2019) to 25.7% in 2021 (Jeong et al., 2021). Furthermore, solution processing such as spin coating and slot die coating, vacuum deposition including thermal evaporation and chemical vapor deposition, as well as low-cost processing features are also important parameters. Besides high efficiencies, the outstanding optoelectronic features, including high optical absorption coefficient, tunability of a bandgap over a broad spectrum range (Unger et al., 2017), high V_{oc} (Tress, 2017), long charge carrier diffusion lengths (Stranks et al., 2013), mark them as a potential contender with state-of-the-art c-Si solar cells in a tandem architecture. Over 20,000 reported publications concentrating on PSCs had been accumulated by the end of 2021 (Science, 2021).

Fig. 1 presents the noteworthy progress in efficiency values in both configurations of silicon/perovskite tandem solar cells (Si/per TSCs) with contributions from different universities and research institutes. Over the past seven to eight years, tandem technology has emerged as a potential technology overcoming the efficiencies from well-established single-junction solar cells. Such development was made possible by rapid progress in perovskite-based solar cells. Over the years, many research groups have been actively involved in developing highly efficient and stable PSCs. This has accelerated the performance development of perovskite-based TSCs, as revealed in Fig. 1.

This review aims to provide a detailed study on two and four-terminal c-Si/per TSCs. First, the latest development in efficiency values of Si/per TSCs is presented. Then, the evolution of PSCs with c-Si (homojunction and heterojunction) bottom devices and their impact on tandem cells performance is summarized. Finally, suitable perovskite top-cells and c-Si bottom cells are proposed for c-Si/per TSCs. In addition, challenges, and limitations in these architectures, such as absorption losses, reflection losses, fabrication issues on textured surfaces, and most importantly, instability issues, have been highlighted. In particular, an investigation of anti-reflecting coatings, current matching mechanisms, transparent electrodes, wide-bandgap PSCs, and recombination layers are discussed. Based on these factors, future directions towards commercialization, non-toxic, cost-effective, highly stable c-Si/per tandem devices have been proposed. We believe that this study will provide extensive information and guidelines on two and four-terminal c-Si/per TSCs to both researchers and beginners in this field.

2. Types of crystalline silicon/perovskite tandem solar cells

Generally, crystalline silicon/perovskite tandem solar cells (c-Si/per TSCs) can be divided broadly into three major configurations, as shown in Fig. 2.

The types of c-Si/per TSCs are described as follows:

- Two terminal (2-T) monolithically connected
- Four terminal (4-T)
  - Mechanically stacked
  - Optical splitting
  - Reflective design
- Three terminal (3-T)

2.1. Two terminal (2-T) monolithically connected

In the two-terminal (2-T) c-Si/per TSCs, the two sub-cells are connected in series, such that the perovskite top sub-cell is directly fabricated on top of the bottom silicon subcell through a recombination junction or interface layer in between the two sub-cells (Fig. 2a) (Mailoa et al., 2015). The silicon bottom subcell performs as a substrate for the top perovskite sub-cell. In this design, the top sub-cell absorbs high energy (short wavelength) photons while transmitting low energy (long wavelength) photons to the bottom sub-cell. Here tandem design has only two terminals making integration in a photovoltaic (PV) module and system at a low fabrication cost. However, current matching is a major issue in this design since two sub-cells are connected

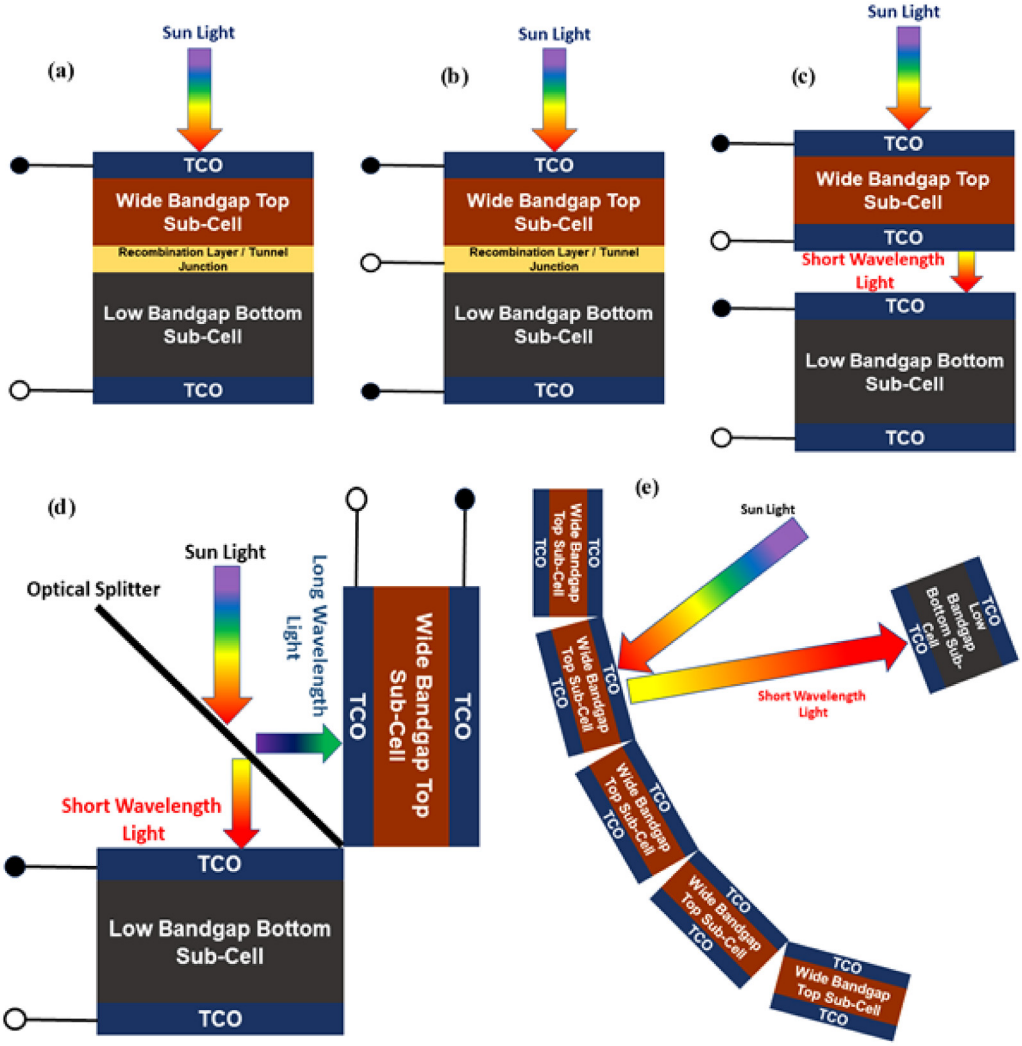

Fig. 2. Schematic design of c-Si/per tandem structures: (a) two-terminal monolithically integrated; (b) three-terminal (c) four-terminal mechanically stacked (d) four-terminal optical spectral splitting; (e) four-terminal reflective tandem.
Source: Reprinted (adapted) with permission from Werner et al. (2018).

in series via a recombination layer or tunnel junction. Due to the current matching requirement, the ideal top cell bandgap is constrained to a narrow range of 1.7–1.8 eV, making the system more sensitive to spectral variations (Dupre et al., 2018). Secondly, as the top sub-cell is fabricated directly onto the bottom sub-cell, the layers in the top sub-cell should be fabricated using a sophisticated procedure to avoid damage to the bottom sub-cell. Moreover, the fabrication of highly conductive and optically transparent layers between two sub-cells is also challenging.

2.2. Four terminal (4-T)

2.2.1. Mechanically stacked

Four terminal (4-T) c-Si/per TSCs are also a class in tandem architectures (Bailie et al., 2015). Similar to the 2-T tandem class, the two sub-cells in this structure are vertically stacked. However, they are optically coupled but electrically independent of each other. Each sub-cell has its own separate two terminals so that they can be operated and optimized separately. This alleviates constraints on the bandgap selection of the top cell and makes the system less susceptible to spectral variations. Consequently, 4-T tandem cells can achieve high efficiencies over a wide bandgap range of 1.6 to 2 eV for the top sub-cell, with an optimal value of 1.81 eV with a c-Si bottom sub-cell (Werner et al., 2018). Current matching and interface or recombination layer between two sub-cells are not required. However, more than one transparent electrode is needed in this design, as shown in Fig. 2c, which may cause more parasitic absorption. In addition to this, since more cable and maximum power point trackers are required in this design, this might increase the overall cost in the design fabrication process (Yamaguchi et al., 2018).

2.2.2. Optical splitting

In the 4-T optical splitting design (Uzu et al., 2015), a dichroic mirror is used, splitting the high energy photons toward the perovskite sub-cell and low energy photons to the silicon sub-cell, as shown in Fig. 2d. The advantage of this type of design is no need for more transparent electrodes. However, the higher cost of optical splitter hinders the economic viability of this tandem structure (Werner et al., 2018).

2.2.3. Reflective design

Another class in 4-T c-Si/per TSCs is reflective tandem (Li et al., 2017). A recently introduced concept of PV Mirror (Zhengshan et al., 2015), in which the cheapest sub-cell is placed in curved order and a short-pass or a long-pass dichroic mirror is used to

Table 1
Evolution of efficiency from two terminal c-Si/per TSCs based on single and multiple cations perovskite top and SHJ bottom sub-cells. (PCE values are taken from reverse scan direction). PCE: power conversion efficiency, SHJ: silicon heterojunction, 2-T: Two-terminal. The area is mentioned in cm^2.

Perovskite Top Cell	Silicon Bottom Cell	Tandem Type	PCE (%)	Year	Device Area	Ref
$FAMAPbI_{3-x}Br_x$	SHJ	2-T	19.9	2015	0.16	Albrecht et al. (2016)
$MAPbI_3$	SHJ	2-T	20.9	2015	0.17	Werner et al. (2015c)
			19.2		1.22	
$MAPbI_3$	SHJ	2-T	20.5	2016	1.43	Werner et al. (2016b)
			22.8	2017	0.25	
$CsFAPbI_{3-x}Br_x$	SHJ	2-T	21.8	2017	1.43	Sahli et al. (2018a)
			19.1	2017	12.96	
$FAMAI_{3-x}Br_x$	SHJ	2-T	20.6	2017	0.03	Fan et al. (2017)
$FAMAPbI_{3-x}Br_x$	SHJ	2-T	18.8	2017	0.13	Zhu et al. (2018b)
			16.52		1	
$CsFAPbI_{3-x}Br_x$	SHJ	2-T	25.5	2018	1.419	Sahli et al. (2018b)
$CsFAPbI_{3-x}Br_x$	SHJ	2-T	25.0	2018	1.00	Bush et al. (2018)
$CsFAMAPbI_{3-x}Br_x$	SHJ	2-T	22.8	2018	0.13	Zhu et al. (2018a)
$CsFAMAPbI_{3-x}Br_x$	SHJ	2-T	22.22	2018	0.06	Qiu et al. (2018)
$CsFAMAPbI_{3-x}Br_x$	SHJ	2-T	25.4	2018	0.422	Chen et al. (2019)
$CsFAMAPbI_{3-x}Br_x$	SHJ	2-T	25.5	2018	0.81	Jošt et al. (2018)
$CsFAMAPbI_{3-x}Br_x$	SHJ	2-T	21.9	2018	0.13	Hou et al. (2019a)
$CsRbFAMAPbI_{3-x}Br_x$	SHJ (poly-Si)	2-T	24.5	2018	1.00	Shen et al. (2018)
$CsFAMAPbI_{3-x}Br_x$	SHJ	2-T	20.4	2019	0.13	Hou et al. (2019b)
$CsFAMAPbI_{3-x}Br_x$	SHJ	2-T	25.2	2019	1.088	Mazzarella et al. (2019)
$CsFAPbI_{3-x}Br_x$	POLO Junction	2-T	25.4	2019	1.42	Nogay et al. (2019)
$CsFAPbI_{3-x}Br_x$	SHJ	2-T	22.6	2019	57.4	Kamino et al. (2019)
$CsFAMAPbI_{3-x}Br_x$	SHJ	2-T	26.0	2019	0.77	Köhnen et al. (2019)
$FACsPbI_{3-x}Br_x$	SHJ	2-T	21.6	2019	0.25	Bett et al. (2019)
$CsMAPb(I_{3-x}Br_x)$	SHJ	2-T	26.2	2020	0.42	Chen et al. (2020)
$CsFAMAPbI_{3-x}Br_x$	SHJ	2-T	26.3	2020	1.43	Lamanna et al. (2020)
$[CsFAPb(I_{3-x}Br_x)]_{1-y}(MAPbCl_3)_y$	SHJ	2-T	27.13	2020	1	Xu et al. (2020a)
$FAMACsPb(I_{3-x}Br_x)_3$	SHJ	2-T	26.7	2020	0.188	Kim et al. (2020)
$FACsPbI_{3-x}Br_x$	SHJ	2-T	25.1	2020	0.25	Schulze et al. (2020)
$CsFAMAPbI_{3-x}Br_x$	SHJ	2-T	29.05	2020	1.064	Al-Ashouri et al. (2020)
$CsFAMAPbI_{3-x}Br_x$	SHJ	2-T	25	2021	1.03	De Bastiani et al. (2021)
$CsFAMAPbI_{3-x}Br_x$	SHJ	2-T	27.80	2021	0.16	Köhnen et al. (2021)
$CsFAMAPbI_{3-x}Br_x$	SHJ	2-T	28.2	2021	1	Liu et al. (2021)

reflect the light towards the more expensive sub-cell (Fig. 2e). This concept presents high flexibility in terms of manufacturing and system integration and can be implemented in solar energy harvesting technologies such as solar thermal collectors. However, the solar tracking performance used in this approach will be poor in collecting the diffuse light present in the solar spectrum (Werner et al., 2018).

2.3. Three terminal (3-T)

In c-Si/per TSCs, a less common design that combines the advantages of 2 and 4-T tandems is known as a three-terminal (3-T) tandem cell (Park et al., 2019; Santbergen et al., 2019). The 3-T tandem design was initially proposed by Nagashima et al. (2000). In this architecture, the bottom silicon sub-cell has interdigitated back contacts that form two terminals, while a front top electrode is formed on top of the perovskite sub-cell, as shown in Fig. 2b (Santbergen et al., 2019).

3. Recent developments

3.1. Two Terminal (2-T) Si/perovskite tandem cells

In the current global PV market, crystalline silicon (c-Si) solar cells technology is the leading technology holding 95% of the total share (Jošt et al., 2020). Therefore, unlike other contenders, silicon receives huge attention as a bottom sub-cell in tandem configuration. c-Si bottom cells for tandem configurations are classified as homojunction (temperature compatibility >400 °C) and heterojunction solar cells (temperature compatibility <250 °C). c-Si solar cells based on homojunction have dominated the PV market for decades. The first c-Si/per TSC was designed using a silicon homojunction cell developed with the high-temperature process. However, silicon heterojunction (SHJ) solar cells offer a variety of advantages. For instance, features such as very high efficiency and high open-circuit voltage (V_{oc}) have attracted the application of SHJ towards c-Si/per TSCs. The single-junction cell record is currently held by SHJ with a certified PCE of 26.6% and a V_{oc} of 740 mV (Yoshikawa et al., 2017a,b). Additionally, the deposition of top sub-cell layers on planar surfaces of the bottom sub-cell using spin coating requires the bottom sub-cell in the n–i–p configuration. In this regard, SHJ solar cells deliver more flexibility in terms of any polarity to be used (Descoeudres et al., 2020). However, on the other side, the low thermal stability of surface passivation by intrinsic amorphous silicon restricts the temperature tolerance of the SHJ solar cell technology, thus limiting the succeeding processing temperatures below 200 °C. Table 1 presents detailed information on 2-T c-Si/per TSCs with SHJ bottom cells. The subsequent sections will present detailed progress on c-Si/per TSCs based on SHJ and homojunction solar cells.

In 2015, Mailoa et al. (2015) demonstrated a 2-T monolithic c-Si/per TSC with 13.7% stable efficiency for 1 cm^2 . Since then, numerous efforts have been performed to improve overall efficiency, and a considerable number of publications on c-Si/per tandem devices have been soared. In 2018, oxford PV reported 28% certified efficiency for 2-T c-Si/per TSC (NREL, 2019). To date, 29.80% efficiency from monolithic 2-T c-Si/per TSC has been reported (NREL, 2021). Fig. 3 is a true representation of the detailed evolution of PCE values in 2-T c-Si/per TSCs. In Fig. 3, the reported PCE values are presented in bars showing the development of efficiencies in 2-T c-Si/per TSCs during the years 2014–2021. This

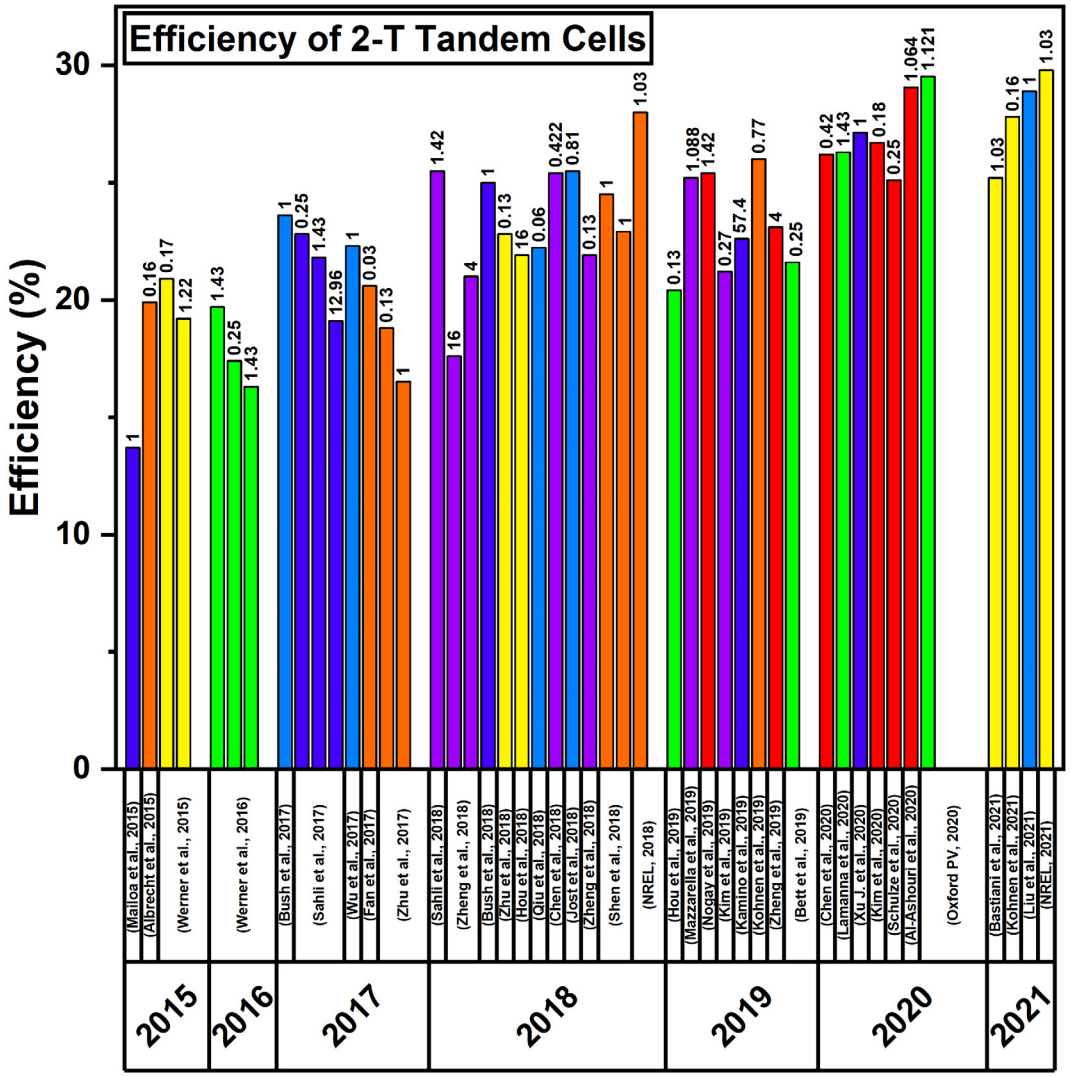

Fig. 3. Evolution of PCE in 2-T TSCs with respect to published year. Reverse scan values are considered here. The numbers mentioned on top of the bars represent the devices area (mentioned in cm^2). The references are mentioned for the comparison.

indicates that PCE values improved from 13.7% to over 29% in a short time, suggesting the potential of tandem technology to achieve above 30% PCE in the future. The numbers mentioned on top of the bars represent the experimental reported tandem devices area in cm^2, which predicts that the device areas also improved with the enhancement of efficiencies. Additionally, for broader understanding, the PCE values with device area less and greater than 1 cm^2 are drawn in Figs. 4(a) and 4(b), respectively.

3.1.1. Silicon Hetero Junction (SHJ)

To address the high-temperature processing (∼500 °C) incompatibility with the best performing silicon heterojunction (SHJ) technology, Albrecht et al. (2016) have developed 2-T c-Si/per TSC. They combined planar perovskite top cell with SHJ bottom cell at the low-temperature process and achieved device efficiency of over 18%. Werner et al. (2015c) processed device fabrication of monolithic planar c-Si/per heterojunction tandem cells at temperature values below 150 °C (Fig. 5a-b). They achieved higher efficiency with improved current density values and reduced hysteresis and reported efficiencies of up to 21.2 and 19.2% for cell areas of 0.17 and 1.22 cm^2, respectively. Sahli and fellows have studied the use of nanocrystalline silicon (nc-Si:H) layers as a recombination junction to avoid the optical losses and shunt resistances as produced by transparent conducting oxides (TCOs) (Sahli et al., 2018a). They used $Cs_{0.19}FA_{0.81}Pb(Br_{0.22}I_{0.78})_3$ perovskite to combine with SHJ bottom cell to form tandem structure and achieved 22.8% and 21.8% efficiencies for device areas of 0.25 cm^2 and 1.43 cm^2, respectively. Zhu et al. (2018b) have demonstrated transparent electrodes with simultaneously good optical transparency and electrical conductivity at low-temperature treated perovskite/SHJ tandem device with a matched J_{sc} of 15.11 mA/cm^2 measured without any anti-reflective foil (ARF). They observed high J_{sc} by carefully adjusting the thickness of the MoO_x buffer layer and the sputtering power of ITO. Using this approach, they achieved 18.81% and 16.52% efficiencies for active device areas of 0.13 cm^2 and 1 cm^2, respectively.

S. Zhu and fellows reported a solvent engineering method to optimize the light absorption and transmittance in perovskites for TSCs (Zhu et al., 2018a). They observed the balanced absorbance and transmittance in the perovskite absorber for the 40% volume ratio of DMSO in the mixed solvent. By adopting solvent engineering techniques on c-Si/per TSCs using a 40% volume ratio of DMSO, they achieved 22.80% efficiency. To boost up light absorption, Hou et al. (2019a) demonstrated light management ARFs using polydimethylsiloxane (PDMS) polymer with inverted random pyramidal textures having three different pyramid size

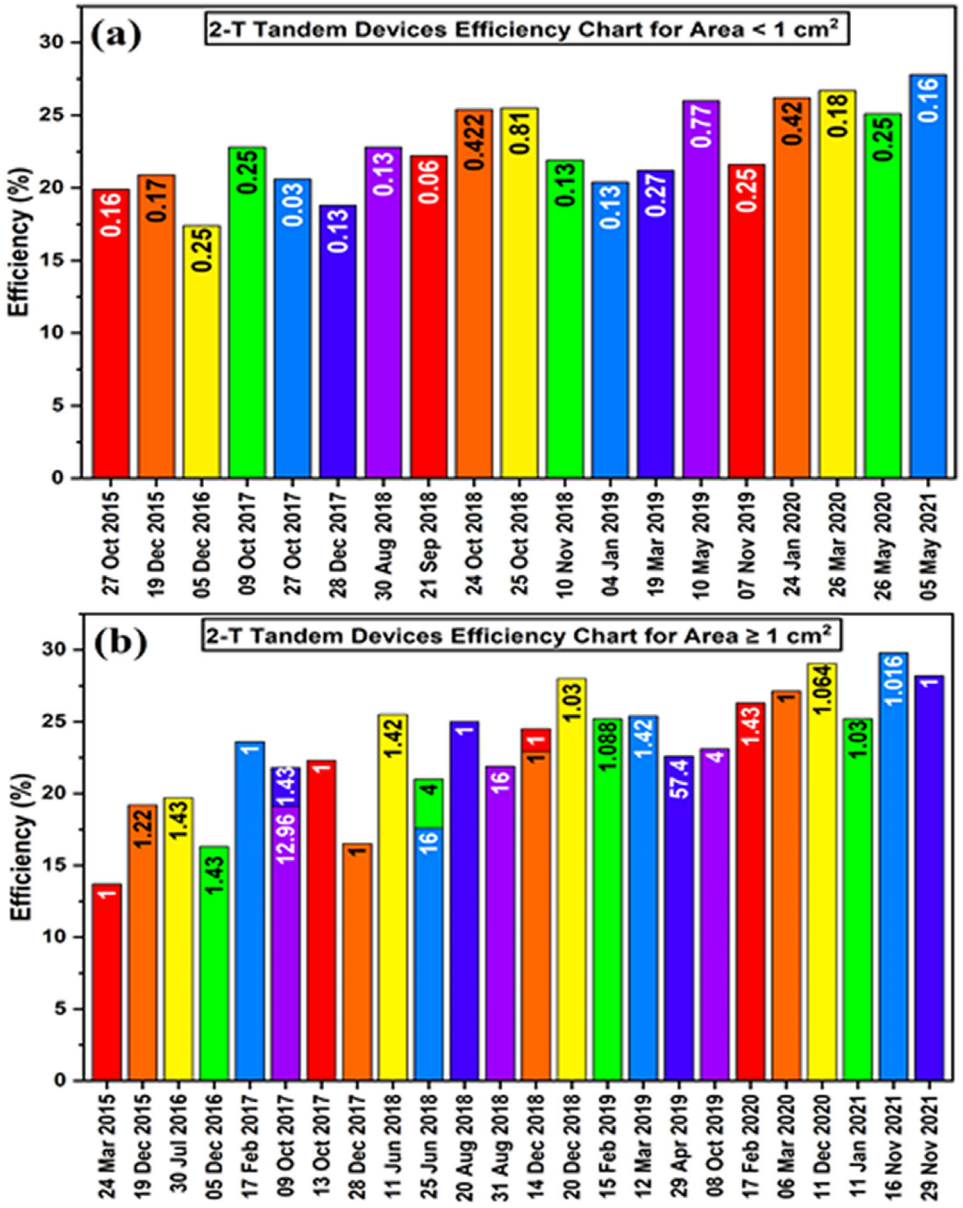

Fig. 4. Evolution of PCE of 2-T Tandem devices for areas (a) < 1 cm^2 (b) ≥ 1 cm^2. Reverse scan values are considered here. The numbers mentioned inside the bars represent the devices area (mentioned in cm^2).

ranges (1–3 μm, 3–8 μm, 8–15 μm). By using a 3-8 μm pyramid size textured layer with $CsFAMAPbI_{3-x}Br_x$ based perovskite composition as top sub-cell, they increased J_{sc} value to 16.89 mA/cm^2 and efficiency value to 21.93% as compared to the J_{sc} of 15.17 mA/cm^2 and PCE of 19.38% values with devices without PDMS layer. To achieve improved V_{oc} while maintaining high efficiency of over 20%, simultaneously, Hou et al. (2019b) fabricated c-Si/per monolithic TSC under a low-temperature process. They demonstrated a V_{oc} of 1.83 V and an efficiency of 20.43% using Cs-doped perovskite with widened bandgap and reduced trap density.

Up to this point, the reported results of 2-T SHJ/per tandems (n–i–p top cells) have been presented with efficiency values below 23%. However, many other research groups developed 2-T SHJ/per TSCs by employing the top sub-cells with p–i–n polarity and reported a notable enhancement in efficiency values. Therefore, beyond this point, 2-T SHJ/per TSCs with p–i–n top sub-cells polarity and efficiency values over 23% will be discussed.

At the beginning of 2017, Bush et al. (2017) designed their device structure to absorb maximum light energy in the visible spectrum and a near-infrared spectrum. They fabricated a monolithic 2-T c-Si/per TSC with a 1-cm^2 aperture area to achieve enhanced efficiency and improved thermal and environmental stability. Combining infrared-tuned SHJ bottom cell with cesium formamidinium (CsFA) lead halide perovskite, 23.6% efficiency was achieved. In the following year, Sahli et al. (2018b) addressed the issues such as higher potential production costs, higher reflection losses, and non-ideal light trapping in the infrared part due to the polished surface of bottom silicon cells. They developed a tandem structure by fully texturing both sides of the bottom silicon cell and top perovskite subcell. For the top perovskite cell deposition on textured surfaces, a hybrid two-step deposition method was developed. This method is a combination of sequential co-evaporation and spin coating. In this method, porous lead iodide (PbI_2) and cesium bromide (CsBr) layers were deposited by co-evaporation, while formamidinium iodide (FAI) and formamidinium bromide (FABr) solutions were deposited

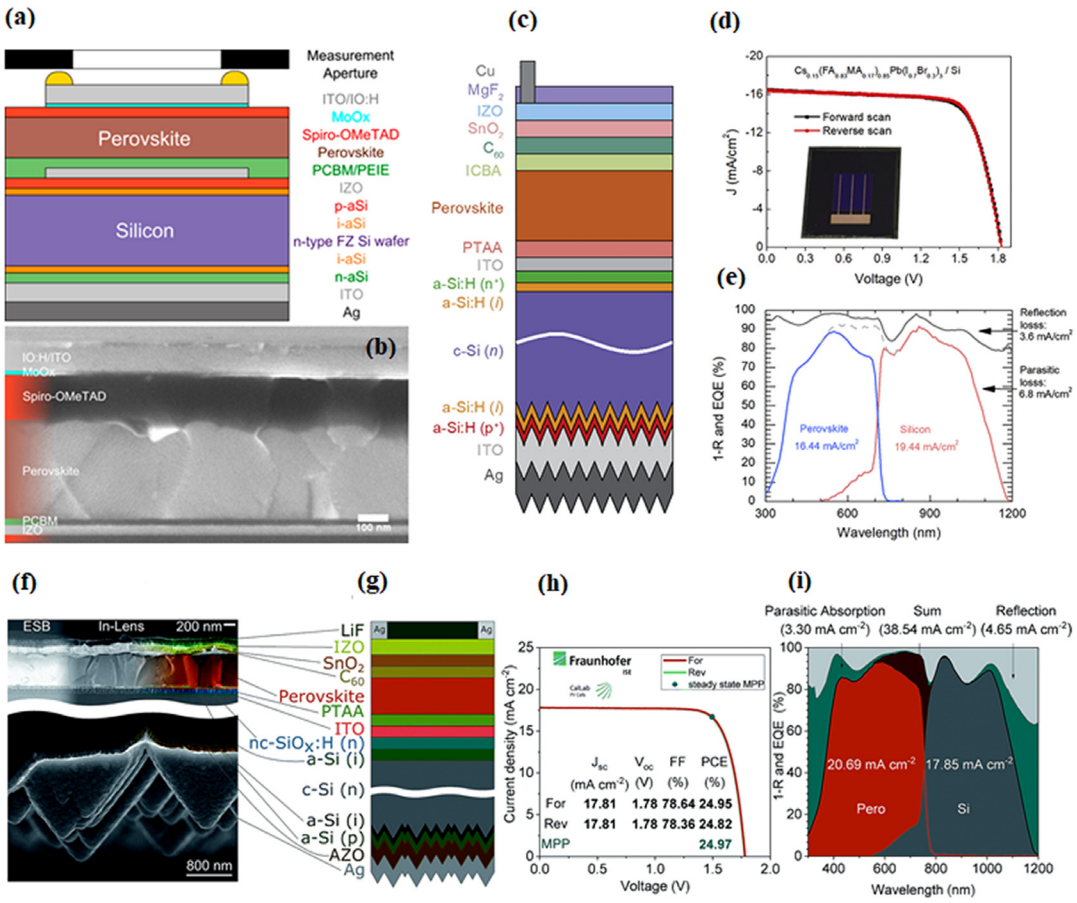

Fig. 5. Different published structures of 2-T c-Si/perovskite tandem Solar cells based on silicon heterojunction (SHJ) technology. (a) Schematic design of the planar monolithic c-Si/perovskite heterojunction tandem cell using n–i–p configuration for top sub-cell and IZO as recombination layer between two sub-cells (b) Cross-sectional SEM image of the perovskite top cell, Reprinted (adapted) with permission from Werner et al. (2015c) Copyright 2015, American Chemical Society. (c) Schematic structure of 2-T c-Si/perovskite tandem cell with both sides planar top sub-cell in p–i–n configuration and textured rear side of the bottom sub-cell (d) J–V characteristics of the 25.4% cell employing $Cs_{0.15}(FA_{0.83}MA_{0.17})_{0.85}Pb(I_{0.7}Br_{0.3})_3$ perovskite absorber layer, tandem device shown in the inset (e) EQE and 1–R curve, Reprinted from Chen et al. (2019) with copyright 2019, permission from Elsevier (f) Colored cross-sectional SEM image of the top cell (upper panel) and back side of the bottom cell (lower panel) of monolithic tandem solar cell with textured back side (g) schematic design layout employing nc-SiO_X:H as an interlayer (h) J–V characteristics (Certified) measured by Fraunhofer Institute for Solar Energy Systems (ISE), the inset table demonstrates the certified performance parameters, 24.97% steady state efficiency value after 400 sec maximum power point (MPP)-tracking (i) EQE and 1–R reflection spectra of the certified tandem solar cell, the integrated current densities and their sum as indicated.
Source: Republished with permission of The Royal Society of Chemistry, from Köhnen et al. (2019).

using spin coating. Using this approach, they reduced primary reflection losses, enhanced light trapping in the infrared, and achieved 25.24% certified efficiency. Under constant illumination, their device retained 90% of its initial power conversion output after 270 h at maximum power point (MPP) tracking.

In contrast to previous work, which claimed 23.6% efficiency (Bush et al., 2017), this time, K. A. Bush and co-workers boosted up the V_{oc} to 1.77 V and J_{sc} to 18.4 mA/cm^2 by using proper optical optimization ended up with 25% efficient c-Si/per TSC on 1 cm^2 active area (Bush et al., 2018). To reduce front surface reflection and parasitic absorption, they implemented thin layers of top transparent electrodes and PDMS stamp with random, pyramidal texture as an anti-reflective coating for boosting light harvesting. Metal fingers were introduced to minimize series resistance losses. Later that year, Jošt et al. (2018) employed textured light management (LM) foil on the front side of the PSC in a tandem structure. By employing LM foil, they reduced the reflection losses, enhanced light trapping, and significantly improved the device efficiency from 23.4% to 25.5%. They observed that the LM foil on top of the cell performed better than the flat anti-reflective coating under perpendicular illumination conditions. The V_{oc} loss is a significant hindrance in c-Si/per TSCs. Many research efforts have been implemented to reduce these losses. Chen et al. (2019) demonstrated one of such efforts in which they employed a grain engineering technique by introducing additives to the perovskite in 2-T c-Si/per TSC (Fig. 5c–e). MACl and MAH_2PO_2 additives in the $Cs_{0.15}(FA_{0.83}MA_{0.17})_{0.85}Pb(I_{0.7}Br_{0.3})_3$ perovskite precursors were used, resulting in a PCE of 22.4%, a high V_{oc} of 1.83 V, and a small J_{sc} of 16.4 mA/cm^2. This small $J_{sc}$was affected due to the rear reflector, blue parasitic absorption by IZO, and ICBA/C_{60}, along with a blue shift of 12 nm. With $Cs_{0.15}(FA_{0.83}MA_{0.17})_{0.85}Pb(I_{0.8}Br_{0.2})_3$ perovskite composition, these J_{sc} and PCE values were improved to 17.8 mA/cm^2 and 25.4%, respectively. In the same year, 28.0% efficient tandem cell having a cell area of 1.03 cm^2 was reported by Oxford PV (PV, 2018).

In early 2019, Mazzarella et al. (2019) developed an optical interlayer based on nanocrystalline silicon oxide (nc-SiO_x:H) and proposed that proper optimized (refractive index & thickness) interlayer can improve current in the bottom sub-cell. With a refractive index of 2.6 (at 800 nm) and 110 nm thickness, they achieved a current gain of 1.4 mA/cm^2 in the bottom sub-cell, demonstrating a certified and stabilized PCE of 25.2%. Nogay et al. (2019) demonstrated thermally stable monolithic 2-T c-Si/per TSC (with 1.43 cm^2 active area) based on p-type c-Si bottom

cells compatible with low-quality wafers and industrial processes. They reported 25.4% power conversion efficiency (25.1% steady-state value) with other parameters defined as V_{oc} 1.74 V, J_{sc} 19.5 mA cm^{-2}, FF 74.7%. In their work, a different class of SHJ bottom cell, namely TopCon/POLO/poly-Si-based cell, was used for the contacts of the c-Si cell rather than low-temperature PECVD-grown a-Si:H or nc-Si:H films. By mid-2019, optically and electrically optimized n-type front contact with reduced reflection and parasitic absorption was studied by Köhnen et al. (2019). They modified the perovskite absorber and front electrode thicknesses to achieve higher PCE and FF and reported a certified PCE of 25% (Fig. 5f-i). The SnO_2 layer was used to prevent moisture and oxygen from penetrating the solar cell and protect the underlying layers from damage during the sputtering. Furthermore, they minimized the reflection losses by employing an n-type nc-SiOx:H as an interconnecting layer between perovskite and silicon cells with a refractive index of 2.7 at 633 nm. The mixed cations and halide $Cs_{0.05}(MA_{0.83}FA_{0.17})Pb(I_{0.83}Br_{0.17})_3$ composition was used as perovskite absorber layer, whereas the float zone (FZ) n-type c-Si wafer with a polished front surface and the rear textured surface was used as a bottom absorber layer.

Earlier in 2020, B. Chen and fellows reported the highly efficient blade coating technique for the deposition of high bandgap perovskite absorber layer on textured silicon cells (Chen et al., 2020). A monolithic c-Si/per TSC was developed using a nitrogen-assisted blading process by fabricating a perovskite layer on top of the textured silicon wafer having pyramids of < 1 μm in height. The tandem device demonstrated 26% efficiency, reducing reflection loss to 2.3 mAcm^{-2} and a matched J_{sc} of over 19 mAcm^{-2}. Lamanna et al. (2020) developed an innovative and highly efficient 2-T c-Si/per TSC, which involves mechanically stacked graphene-doped mesoscopic perovskite top sub-cell with the double-sided textured SHJ bottom sub-cell. The graphene-assisted mesoscopic PSC increased FF and V_{OC} by reducing the series resistance and increasing the electron injection. Besides this, the chemical stability of the mesoscopic perovskite was also enhanced due to incorporation of graphene. The champion tandem device exhibited 26.3% PCE with a stabilized value of 25.9% over an area of 1.43 cm^2. Xu et al. (2020a) demonstrated 27% efficiency from a 2-T c-Si/per TSC with an area of 1 cm^2. They incorporated (1.67 eV) wide-bandgap planar perovskite top cells using triple-halide alloys (chlorine, bromine, iodine) with front side polished SHJ bottom cell. Kim et al. (2020) demonstrated 26.7% efficient monolithic 2-T c-Si/per TSC. An anion engineering of the 2D/3D additives in the PSC exhibited over 80% stabilized behavior from the initial value over 1000 h of testing. Similarly, Schulze et al. (2020) developed a monolithic c-Si/per TSC by employing a MA-free high bandgap (≈ 1.68 eV) perovskite absorber layer. When combined $FA_{0.75}Cs_{0.25}Pb(I_{0.8}Br_{0.2})_3$ perovskite-based top sub-cell in planar p–i–n arrangement with SHJ bottom sub-cell, a 25.1% efficiency was achieved. In 2020, Helmholtz-Zentrum Berlin (HZB) demonstrated a monolithic c-Si/per TSC having an active area of 1.06 cm^2 with a certified efficiency of 29.15% (Al-Ashouri et al., 2020). By employing Me-4PACz ([4-(3,6-dimethyl-9H-carbazol-9-yl)butyl]phosphonic acid) as an hole transport layer (HTL), they improved hole extraction and achieved an excellent PCE value. In this work, they used a triple cation perovskite absorber based on $Cs_{0.05}(FA_{0.77}MA_{0.23})_{0.95}Pb(I_{0.77}Br_{0.23})_3$ composition with 1.68 eV bandgap. The tandem cell maintained 95% of its initial efficiency value after 300 h under the MPP tracking without encapsulation in ambient air. Recently, the highest recorded PCE from HZB was surpassed by Oxford PV by achieving 29.52% PCE value (certified by the National Renewable Energy Laboratory, NREL) (PV, 2020). During the revision process of this article, a research group at HZB claimed the highest certified efficiency value of 29.80% for 2-T c-Si/per TSC (NREL, 2021). Albeit, the scientific publications with all related information have not yet been reported for these achievements.

3.1.2. Homojunction

In 2015, Mailoa et al. (2015) demonstrated a 2-T monolithic c-Si/per multijunction solar cell with 13.7% stable efficiency for 1 cm^2 (Fig. 6a-b). As a recombination junction interband tunnel junction was used. Tunnel junction was formed by depositing highly n-doped (n^{++}) amorphous hydrogenated silicon (a-Si:H). This junction facilitated electron tunneling through the electron selective contact from the perovskite top cell into the p-type emitter of the Si bottom cell. For the PSC, $MAPbI_3$ perovskite with a 1.61 eV bandgap was used. A top electrode based on a mesh of silver nanowires (AgNWs) was used, and a 111 nm thick anti-reflection coating of LiF was thermally evaporated. A year later, in 2016, Werner et al. (2016a) used thermally stable zinc tin oxide (ZTO) as a recombination layer to combine mesoscopic perovskite with homojunction silicon cell in tandem structure for temperature up to 500 °C. Using ZTO, they achieved 16% efficiency along with V_{oc} of 1643 mV, J_{sc} of 15.3 mA/cm^2, and FF of 64.8% for a device with an aperture area of 1.43 cm^2. In 2017, Wu et al. (2017) overcame the limitations in mesoscopic homojunction Si/per TSCs. They developed the monolithic tandem design by introducing passivated front and rear surfaces and rear side texturing. A modified vacuum flash method was used to deposit high-quality quadruple cation perovskite ($Cs_{0.07}Rb_{0.03}FA_{0.765}MA_{0.135}PbI_{2.55}Br_{0.45}$) to obtain good uniform films with low pinhole density. By this design, they reported the highest steady-state efficiency of 22.5% with mesoscopic perovskite/homojunction silicon TSCs.

In 2018, Zheng et al. (2018a) integrated low-temperature processed planar $MAPbI_3$ PSC on a homojunction silicon solar cell in a monolithic tandem structure. Without using an extra interface layer on large areas, they achieved stabilized efficiencies of 20.5% and 17.1% for 4 cm^2 and 16 cm^2 device areas, respectively. A low temperature and solution-processed SnO_2 was used that served as an electron transport layer (ETL) and a recombination layer. In continuation to their previous work (Zheng et al., 2018a), this time, they demonstrated 21.8% steady-state efficiency with the largest cell area of 16 cm^2 (Zheng et al., 2018b). A mixed perovskite $(FAPbI_3)_{0.83}(MAPbBr_3)_{0.17}$ was replaced with previously reported $MAPbI_3$ to achieve higher V_{oc} and reduced hysteresis. In addition, using the back-side texturing concept, the current density of the tandem device was improved. At the end of 2018, Shen et al. (2018) have demonstrated a third and distinct strategy to fabricate efficient monolithic 2-T c-Si/per TSCs without the use of interface and recombination junction. In this approach, the top perovskite subcell was placed in direct contact with Si bottom cell. This interlayer-free idea offers advantages of simple processing with reduced optical losses as presented by TCOs and tunnel junction interlayers. Stabilized efficiencies of 22.9% and 24.1% (J–V parameters: PCE 24.5%, V_{oc} 1.76 V, J_{sc} 17.8 mA cm^{-2}, FF 78.1%) were reported for homojunction and passivating contact heterojunction devices, respectively.

In 2019, Kim and fellow workers developed a 2-T c-Si/per TSC based on p-type homojunction Si cells to fabricate low-cost and highly efficient monolithic tandem cells (Fig. 6f–g) (Kim et al., 2019). By employing a perovskite layer of $(FAPbI_3)_{0.8}(MAPbBr_3)_{0.2}$ with 310 nm thickness and HTL based on poly[bis(4-phenyl)(2,4,6-trimethylphenyl)amine] (PTAA), a 21.19% PCE was reported. Later on, in 2019, Zheng et al. (2019) successfully illustrated the use of low-cost down-shifting $(Sr,Ba)_2SiO_4:Eu^{2+}$ phosphor incorporated with an antireflection film of PDMS (Fig. 6 c–e). They reported 23.1% PCE, 81% FF with J_{sc} of 16.5 mA cm^{-2}, and V_{oc} of 1732 mV.

In Table 2, detailed information on 2-T Si/per TSCs with Si homojunction bottom cells is presented. In contrast to SHJ bottom cells, a small amount of work has been performed on TSCs based on Si homojunction solar cells. Also, the highest PCE values have been achieved with SHJ solar cells.

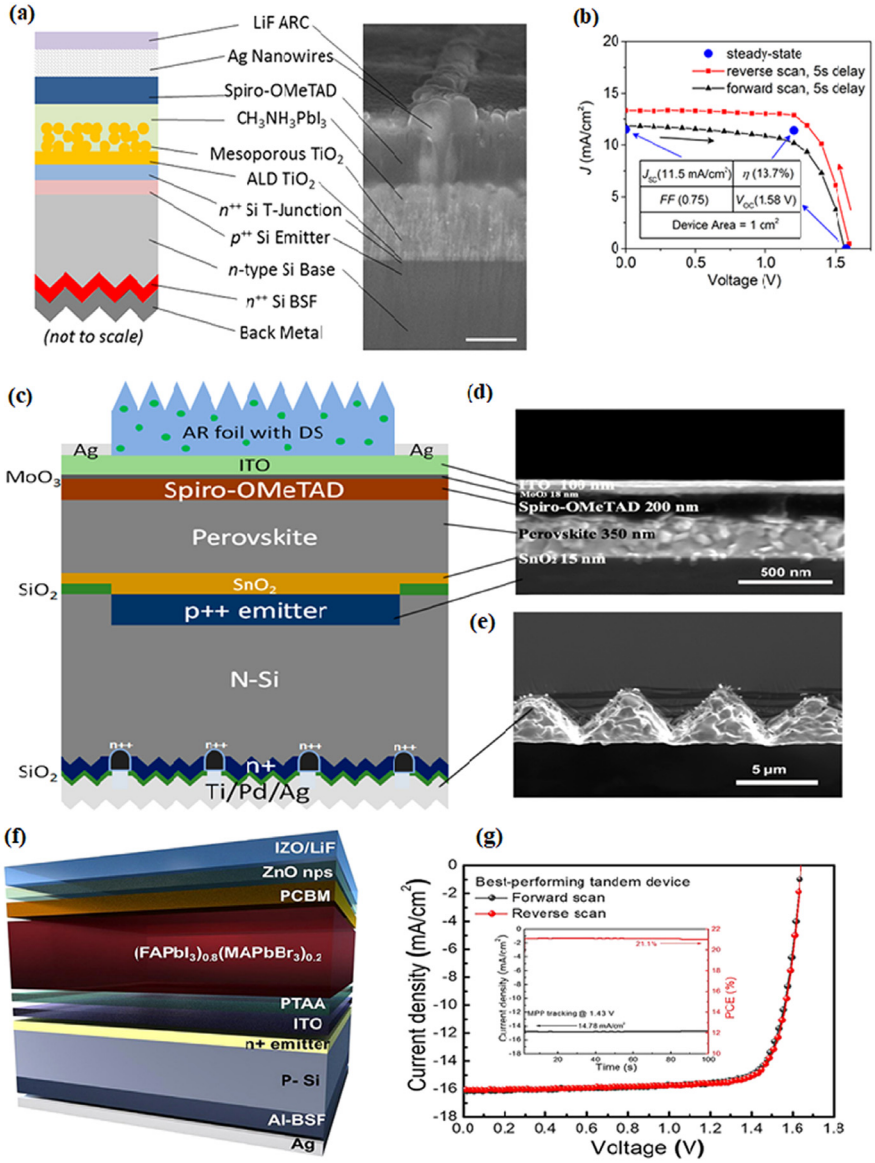

Fig. 6. Different published structures of 2-T c-Si/per TSCs based on silicon homojunction technology (a) The device structure of a 2-T monolithically grown c-Si/per multijunction solar cell with an n-type Si base and a highly doped (n^{++}) amorphous hydrogenated silicon (a-Si:H) formed by PECVD for the interband tunnel junction to facilitate electron tunneling from the electron selective contact in the perovskite top cell into the p-type emitter of the Si bottom cell, the corresponding SEM image taken at 45° tilt to show the Ag nanowire mesh (500 nm scale bar). (b) J–V characteristics of the 2-T c-Si/per multijunction solar cell under AM1.5G illumination with forward and reverse-bias scan directions having 5 s measurement delay per data point and the corresponding table of solar cell parameters, Reprinted from Mailoa et al. (2015) with the permission of AIP Publishing. (c) Schematic of c-Si/per homojunction solar cell with a down-shifting anti-reflective PDMS film, cross-sectional SEM images of the (d) perovskite top sub-cell and (e) the textured rear silicon bottom sub-cell, Reprinted (adapted) with permission from Zheng et al. (2019) Copyright 2019, American Chemical Society. (f) Schematic of a fully planar monolithic Si/per tandem structure, with 310 nm thick $(FAPbI_3)_{0.8}(MAPbBr_3)_{0.2}$ perovskite absorber layer, PTAA as HTL and PCBM as ETL, fabricated on the p-type homojunction silicon cell (g) J–V and maximum power point tracking characteristics (inset) of the best-performing monolithic Si/per tandem devices, Reprinted from Kim et al. (2019), copyright 2019, with permission from Elsevier.

Table 2
Evolution of efficiency from 2-T c-Si/per TSCs based on single and multiple cations perovskite top and silicon homojunction bottom sub-cells. (PCE values are taken from reverse scan direction). *represents steady-state efficiencies, PCE: power conversion efficiency, 2-T: Two-terminal. The area is mentioned in cm^2.

Perovskite Top Cell	Silicon Bottom Cell	Tandem Type	PCE (%)	Year	Device Area	Ref
$MAPbI_3$	Homojunction	2-T	13.7*	2015	1.00	Mailoa et al. (2015)
$MAPbI_3$	Homojunction	2-T	17.4 16.3	2016	0.25 1.43	Werner et al. (2016b)
$CsRbFAMAPbI_{3-x}Br_x$	Homojunction	2-T	22.3	2017	1.00	Wu et al. (2017)
$MAPbI_3$	Homojunction	2-T	21.0 17.6	2018	4.00 16.00	Zheng et al. (2018a)
$FAMAPbI_{3-x}Br_x$	Homojunction	2-T	21.9	2018	16.00	Zheng et al. (2018b)
$CsRbFAMAPbI_{3-x}Br_x$	Homojunction	2-T	22.9	2018	1.00	Shen et al. (2018)
$FAMAPbI_{3-x}Br_x$	Homojunction	2-T	21.2	2019	0.27	Kim et al. (2019)
$FAMAPbI_{3-x}Br_x$	Homojunction	2-T	23.1	2019	4.00	Zheng et al. (2019)

3.2. Four terminal (4-T) Si/perovskite tandem cells

In Nov 2014, Löper et al. (2015) used the concept of 4-T c-Si/per TSCs for the first time. To avoid sputter damage during the ITO deposition to the underneath layers and provide lateral conductivity to the metallization, they used MoO_x capped with ITO. $MAPbI_3$ in a mesoporous structure with a transparent MoOx/ITO electrode was used for the top sub-cell. Similarly, a-Si:H/c-Si heterojunction was used as a bottom sub-cell. By combining these two sub-cells, a 13.4% efficiency was reported, with 6.2% and 7.2% contribution from the top and bottom cells, respectively. Later on, in the same year, Bailie et al. (2015) used a transparent AgNWs electrode on a perovskite subcell to achieve a semi-transparent device. The semi-transparent sub-cell was set in a mechanically stacked tandem arrangement on copper indium gallium diselenide (CIGS) and low-quality multi-crystalline silicon (mc-Si) to obtain solid-state polycrystalline TSCs. First, AgNWs solution was spray deposited on flexible Polyethylene terephthalate (PET) film at a temperature of 60 °C. After that, AgNWs were transferred from PET to the perovskite layer by mechanically transfer method. For this, a 500 g of downward force was used by a single 1/4-in. diameter ball bearing followed by a careful rolling of ball bearing over the active area of the perovskite. The tandem cell (mc-Si/Per) demonstrated an efficiency of 17% (a combined sum of 12.7% and 4.3%). By mid of 2015, Werner et al. (2015a) demonstrated low power and reproducible low temperature processed IZO having extraordinary electrical and optical characteristics with high near-infrared transparency. By combining the IZO layer with an evaporated MoO_x buffer layer in a PSC, over 10% efficiency with more than 60% transmittance in the 800–1200 nm wavelength range was reported. In the 4-T tandem configuration, when $MAPbI_3$ based perovskite absorber layer in mesoporous configuration was mechanically stacked with a-Si/c-Si heterojunction bottom sub-cell, a 19.6% collective efficiency was achieved.

Early in 2016, D. P. McMeekin and fellows addressed poor optical and thermal stability-related issues in perovskite materials with an optical bandgap of ∼1.75 eV (McMeekin et al., 2016). The $[HC(NH_2)_2]_{0.83}Cs_{0.17}Pb(I_{0.6}Br_{0.4})_3$ perovskite material having an optical band gap of ∼1.74 eV with high crystallinity and high compositional photostability was used. The fabricated device exhibited V_{oc} of 1.2 V with PCE of over 17% for small areas and 14.7% for 0.715 cm^2 cells. Duong et al. (2016a) presented optimum contact parameters with outline directions towards the development of future transparent contacts for tandem cells through a detailed investigation of electrical and optical power losses. By optimizing sputtered ITO as front and rear contacts, semitransparent PSCs with steady-state efficiency exceeding 12% and enhanced transmittance of >80% in the 800–1000 nm wavelength range were developed. A top perovskite and filtered passivated emitter rear locally diffused (PERL) silicon bottom sub-cells yielded a combined efficiency of 20.1% in a mechanically stacked configuration. In mid-2016, Chen et al. (2016) presented the use of highly optical transparent and electrical conductive ultrathin metal electrodes in PSCs. Later on, combining this semitransparent PSC with a-Si/c-Si heterojunction solar cell in 4-T configuration, a 23% combined efficiency was achieved (16.5% efficiency from top PSC and 6.5% efficiency from the Si cell) with 0.075 cm^2 aperture area of the top sub-cell. Werner et al. (2016b) developed low-temperature NIR-transparent PSCs with steady-state efficiencies up to 16.4% and 14.5% for aperture areas of 0.25 cm^2 towards the potential future industrialization step 1.015 cm^2, respectively (Fig. 7b). Later on, these cells were applied in mechanically stacked 4-T SHJ/per TSCs and exhibited efficiencies up to 23% and 25.2% for 1.015 cm^2 and 0.25 cm^2 top cell aperture areas, respectively. For an aperture area of 1.43 cm^2 for top PSC, with full textured bottom Si cell, a 20.5% PCE was achieved (Fig. 7e-f). By the end of 2016, Peng et al. (2017) developed a one-step solution-based technique to fabricate a high-quality ETL based on indium-doped titanium oxide (In-TiO_x) material (Fig. 7c-d). By employing In-TiO_x as ETL, they developed highly efficient solar cells based on $MAPbI_3$ and $Cs_{0.05}(MA_{0.17}FA_{0.83})_{0.95}$-$Pb(I_{0.83}Br_{0.17})_3$ and achieved PCE values of 18.9% and 20.1%, with significant FF values of 0.771 and 0.791, respectively. With this optimized ETL in a semi-transparent PSC, a steady-state efficiency of 16.6% was established, with a 24.5% efficiency from a 4-T Si/per TSC. The top perovskite sub-cell used in the tandem configuration was based on Cs-mixed halide perovskite. The bottom silicon sub-cell was highly efficient interdigitated back contact (IBC) silicon.

Early in 2017, Duong et al. (2017) explored a new cation, namely rubidium (Rb), in a novel multication structure with the formamidinium/methylammonium/cesium (FA/MA/Cs) and obtained 1.73 eV bandgap PSCs. With minimal hysteresis, they achieved steady-state efficiency of 17.4% for opaque cells. Later on, semi-transparent PSCs were designed with a steady-state efficiency close to 16.0% with improved average transparency of ≈84% in the range of 720 and 1100 nm. When this cell was combined with 23.9% efficient silicon cell, a 26.4% efficiency (10.4% from the silicon cell) was achieved in a mechanically stacked tandem arrangement. In the same year, Jaysankar et al. (2017) addressed limitations in transparent electrodes relating to sheet resistance and optical transparency when developing large area semi-transparent cells. They developed a scalable 4-T c-Si/per TSC by adopting the module-on-cell concept, where a perovskite solar module with interconnected sub-cells was combined with a Si solar cell (Zhang et al., 2015). Initially, a cell-on-cell structure with an aperture area of 0.13 cm^2 was developed. Later on, module-on-cell architecture was fabricated by combining a semitransparent $MAPbI_3$ perovskite solar module having an aperture area of 4 cm^2 on top of an IBC c-Si solar cell with the same area.

At the beginning of 2018, Quiroz et al. (2018) demonstrated all-solution processed PSCs with enhanced infrared transparency. They introduced Copper(I) thiocyanate (CuSCN), replacing PEDOT:PSS as an HTL. Similarly, aluminum-doped zinc oxide (ZnO:Al) nanoparticles (NPs) as the electron selective top layer (to decouple the AgNWs from the iodine-containing perovskite) were employed in their work. With reduced parasitic and optical absorption from the CuSCN and solution-processed AgNWs as the bottom electrode, a semi-transparent solar cell was developed with efficiencies up to 17.1%. Finally, in a 4-T c-Si/per mechanically stacked configuration with PERL and IBC as bottom cells, 26.7% and 25.2% efficiencies by perovskite-PERL and perovskite-IBC were reported, respectively. Zhang et al. (2018) developed 4-T c-Si/per TSC by employing $(Cs_{0.05}(MA_{0.17}FA_{0.83})_{0.95}Pb(I_{0.9}Br_{0.1})_3)$ based top sub-cell and IBC c-Si bottom cell. With p–i–n planar configuration top sub-cell, proper optimization of the ITO material properties, and light management, a 25.7% efficiency was achieved. They improved the limited NIR transmittance up to 92% of the semitransparent top sub-cell. For the HTL preparation, a ∼20 nm thick layer of NiO NPs capped by PTAA was used. Similarly, two layers of ∼40 nm thick PCBM and ∼30 nm thick ZnO NPs were used for the ETL deposition. Later on in the same year, Kanda et al. (2018) compared the optic and photovoltaic characteristics of flat and textured silicon surfaces in mechanical stacking of 2 and 4-T c-Si/per tandem structures. They demonstrated reduced reflectance (2.7% → 0.8%) of the textured silicon surface compared to the flat silicon surface in the 750–1050 nm wavelength range. Moreover, an increase in the average IPCE value from 83% to 88% and J_{sc} value from 13.7 mA cm^{-2} to 14.8 mA cm^{-2} was also observed. When they employed a textured c-Si solar cell with $MAPbI_3$ perovskite in a

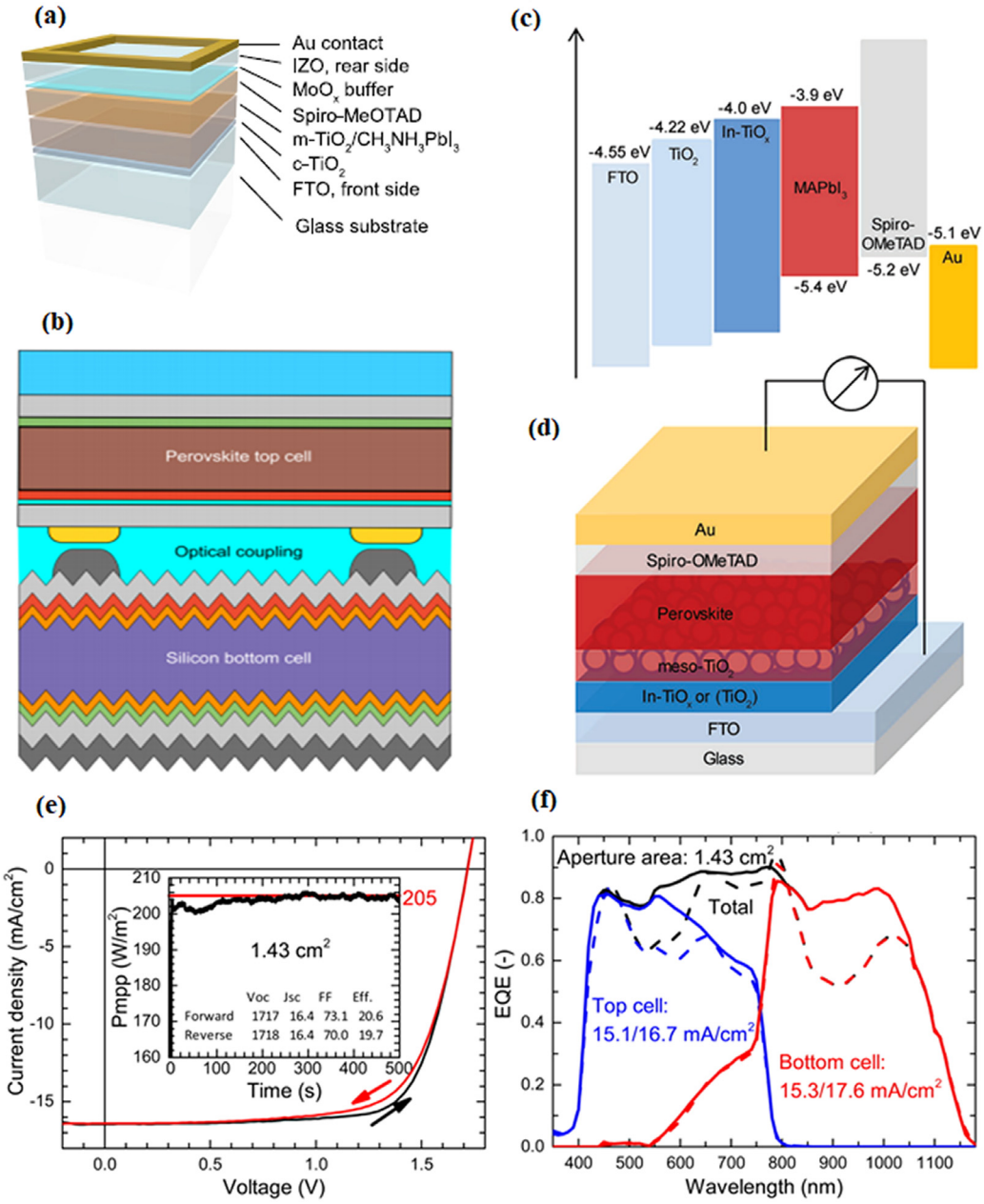

Fig. 7. (a) Schematic illustration of a PSC structure with thermally evaporated (MoO_x) as a buffer layer and a transparent rear electrode and top Au contact. Reprinted from Werner et al. (2015a), copyright 2015, with permission from Elsevier, (b) schematic drawing of the 4-terminal mechanically stacked tandem cell with a NIR-transparent planar perovskite top cell, and a double side textured silicon heterojunction bottom cell. Reprinted with permission from Werner et al., 2016b. American Chemical Society. (c) Energy level diagram showing $MAPbI_3$ with respect to hole transport layer (Spiro-OMeTAD), electron transport layers (TiO_2 and ln-TiO_x), FTO and Au. (d) Schematic of the standard device structure in n–i–p configuration fabricated on FTO coated glass substrate with gold (Au) layer on top. Reprinted from Peng et al. (2017), copyright 2016, with permission from Wiley. (e) J–V characteristics of a 1.43 cm^2 monolithic tandem with silicon bottom cell, a steady power output under maximum power point tracking is shown in the inset (e) EQE spectra of the same tandem cell, measured with (solid lines) and without (dashed lines) antireflective foil.
Source: Reprinted with permission from Werner et al. (2016b).

4-T mechanically stacked configuration, a 21.4% efficiency was achieved. To harvest solar energy efficiently, perovskites having bandgaps in the range of 1.7 and 1.8 eV are optimal for tandem designs with c-Si. However, in such wide-bandgap PSCs, it is crucial to reach high V_{oc} since these wide-bandgap perovskites face V_{oc} deficits of more than 0.65 V. At the end of 2018, Jaysankar et al. (2018) examined the factors affecting V_{oc} in wide-bandgap mixed halide PSCs. In their work, $CsFAPbI_{3-x}Br_x$ based PSC with a bandgap of 1.72 eV was demonstrated, which showed V_{oc} of 1.22 eV. They revealed that the ionization potential of HTL not only affects V_{oc}, but perovskite/ HTL interface quality has a direct influence on V_{oc}. Additionally, the passivation of the perovskite/ HTL interface quality was enhanced by introducing Al_2O_3 in between perovskite/HTL layers. The Al_2O_3 passivation improved V_{oc} and FF of the solar cell and boosted the PCE from 11.7 to 13.8% for cell are of 0.13 cm^2. Moreover, the $CsFAPbI_{3-x}Br_x$ based solar cells demonstrated an average transmittance of 90% between the 700–1200 nm wavelength range. When the reference $CsFAPbI_{3-x}Br_x$ based solar cells were combined with IBC c-Si solar cells in 4-T configuration, 27.1% efficiency was achieved. To develop 4 cm^2

tandem solar modules in module-on-cell configuration, with the same top and bottom dimensions, the devices demonstrated an overall PCE of 25.3%.

A year later, a group from Nanyang Technological University, Singapore (NTU), in collaboration with the National University of Singapore, Singapore (NUS), developed a 4-T c-Si/per TSC and demonstrated 25.5% efficiency (Dewi et al., 2019b). Their champion device was based on $Cs_{0.05}(MA_{0.17}FA_{0.83})_{0.95}Pb(I_{0.83}Br_{0.17})_3$ top sub-cell absorber layer with a bandgap of 1.58 eV and with an industrial-relevant low-cost n-type Si-based bottom sub-cell. After a few months, Wang et al. (2019) developed a molybdenum trioxide (MoO_3) sandwiched gold nanomesh (MoO_3/Au/MoO_3) multilayer transparent electrode fabricated by mild thermal evaporation. The semitransparent PSC based on MoO_3/Au/MoO_3 demonstrated 18.3% efficiency. When $MAPbI_3$ based semi-transparent cell was combined with heterojunction silicon solar cell in mechanically stacked tandem configuration, 27.0% efficiency was achieved. At the end of 2019, Dewi et al. (2019a) demonstrated the same top and bottom sub-cells in 4-T c-Si/per tandem structures in different measurement schemes and proposed more than 1% variation in overall PCE. Their tandem devices exhibited PCEs of 24.7% and 23.5% when used as filtered and masked measurement schemes, respectively. The perovskite absorber layer used in this work was $Cs_{0.05}(MA_{0.17}FA_{0.83})_{0.95}Pb(I_{0.83}Br_{0.17})_3$ while a low-cost, common industrialized structure, PERC n-type c-Si, was used as a bottom sub-cell.

Early in 2020, Rohatgi et al. (2020) have developed 4-T c-Si/per TSCs using low-cost silicon bottom sub-cell and demonstrated 26.7% efficiency. The champion tandem device incorporated $CsFAMAPbI_{3-x}Br_x$ semi-transparent PSC as the top sub-cell. While a single side n-TOPCon Si (a diffused boron emitter on the front and tunnel oxide assisted n^+ poly-Si/SiO_x passivated contact on the rear) cell as bottom sub-cell. Soon after this, Duong et al. (2020) investigated surface coating and bulk incorporation strategies to combine 2D and 3D perovskites. Using a surface coating scheme, a semitransparent PSC was developed by combining 2D perovskite-based n-butylammonium (n-BABr) with quadruple-cation mixed-halide-based 3D perovskite ($E_g \approx 1.72$ eV). When the semitransparent solar cell was combined with silicon cell in a mechanically stacked configuration, a combined 27.7% efficiency with IBC silicon bottom cells (size-unmatched) and 26.2% with PERL diffused silicon bottom cells was achieved for a 1 cm^2 (size-matched) tandem. In Mar 2020, Gharibzadeh et al. (2020) demonstrated improved V_{OCs} (≈45 mV enhancement) with stabilized PCEs. The double cation PSC was introduced with engineered bandgap ($FA_{0.83}Cs_{0.17}Pb(I_{1-y}Br_y)_3$; $0.24 \leq y \leq 0.56$, 1.65 eV ≤ Eg ≤ 1.85 eV) and passivated a 2D/3D perovskite heterostructure. When employed the same structure in 4-T c-Si/per tandem configuration, 25.7% efficiency was achieved. During the revision process of this manuscript, Yang et al. (2021) have reported 28.3% efficiency for 4-T c-Si/per TSC. This is the highest value reported so far from 4-T c-Si/per TSCs.

In Fig. 8, a detailed evolution of PCE values in 4-T c-Si/per TSCs is presented. The reported PCE values are displayed in bars showing efficiencies in 4-T c-Si/per TSCs during 2014–2021. The numerical numbers mentioned on top of the bars represent the experimental reported tandem devices area in cm^2, indicating that the device areas also improved with the enhancement of efficiencies. In a few years, the PCE values enhanced from the first reported value of 13.4% in 2014 to over 28% in 2021.

4. Materials for c-Si/perovskite tandem cells and power conversion efficiencies

The subsequent sections will discuss organic–inorganic hybrid perovskites commonly used as materials for top sub-cells in tandem architectures. Various perovskite compositions such as single and multiple cations, their properties, and related issues will be highlighted. Besides the top sub-cells, numerous types of silicon bottom sub-cell will be part of the discussion in this section.

4.1. 2-T Si/perovskite

4.1.1. Top cell

One of the most common and longest used perovskites is methylammonium lead iodide ($CH_3NH_3PbI_3$) or $MAPbI_3$. It is an inorganic–organic hybrid perovskite that forms a tetragonal crystal structure and is compatible with solution processing and evaporation techniques. $MAPbI_3$ is a strong absorbing direct bandgap semiconductor with a bandgap of around 1.5–1.6 eV (Leguy et al., 2016). Furthermore, it is an intrinsic material with high carrier mobilities, shallow defect levels, and ∼1 μm carrier diffusion lengths, which are essential metrics for highly performing solar cells (Herz, 2017). It would be reasonable to mention that $MAPbI_3$ perovskite promoted the opening of TSCs when Mailoa et al. (2015) demonstrated 2-T monolithic c-Si/per multijunction solar cell by utilizing $MAPbI_3$ as a top sub-cell. They presented a 13.7% stable efficiency for 1 cm^2 device area by interconnecting the two sub-cells using a tunnel junction. Similarly, in the same year, Werner et al. (2015c) processed the monolithic planar heterojunction tandem cells at a temperature below 150 °C. $MAPbI_3$ perovskite layer was used as top sub-cell and deposited by a two-step deposition process. The efficiencies of up to 21.2 and 19.2% for tandem cell areas of 0.17 and 1.22 cm^2, respectively, were reported. A year later, another work was reported by the same group, in which they introduced thermally stable (up to 500 °C) ZTO as a recombination layer (Werner et al., 2016a). By utilizing $MAPbI_3$ top sub-cell perovskite absorber layer with homojunction silicon cell in tandem structure, they achieved efficiency values over 16% and 17% for devices with areas of 1.43 and 0.25 cm^2, respectively. By mid-2018, Zheng et al. (2018a) successfully employed low-temperature processed planar $MAPbI_3$ PSC as the top sub-cell in 2-T c-Si/per monolithic tandem cell. Without using an additional interface layer on large areas, they achieved stabilized efficiencies of 20.5% and 17.1% for 4 cm^2 and 16 cm^2 devices, respectively.

Up to this point, $MAPbI_3$was the extensively used perovskite absorber material for the top sub-cell in tandem configuration with a bandgap of ≈1.5 eV. However, this value is lower than the optimal value of ≈1.73 eV required for an ideal top sub-cell in c-Si/per monolithic tandems (Werner et al., 2018). A corresponding increase in Voc can be achieved by improving the bandgap while maintaining material and interface quality. By replacing iodide with bromide, the bandgap of $MAPbI_3$ based perovskites can easily be tuned from 1.55 to over 2 eV (Eperon et al., 2014). However, stability issues were reported in these compounds in terms of photoinduced phase segregation and phase separation (Slotcavage et al., 2016; Hoke et al., 2015; Brunetti et al., 2016; Barker et al., 2017) and a phase transition to a cubic phase at a temperature of 60 ≈ °C (the operational temperature range of the PV module). This does not fulfill the criteria of long-term stability (85 °C) set by the international regulations for commercial PV products (Conings et al., 2015).

To improve efficiency along with stability in $MAPbI_3$ based TSCs, a solution of mixed cations was proposed, which incorporates a combination of FA^+ and MA^+. Even the first perovskite device to exceed 20% PCE was fabricated with a mixture of MA/FA (Chen et al., 2018). In c-Si/per tandem design, this idea was first implemented in 2015, when Albrecht et al. (2016) developed 2-T c-Si/per tandem cell. They used planar perovskite top cell employing $FAMAPbI_{3-x}Br_x$ perovskite (Eg ≈ 1.57 eV) and SHJ bottom

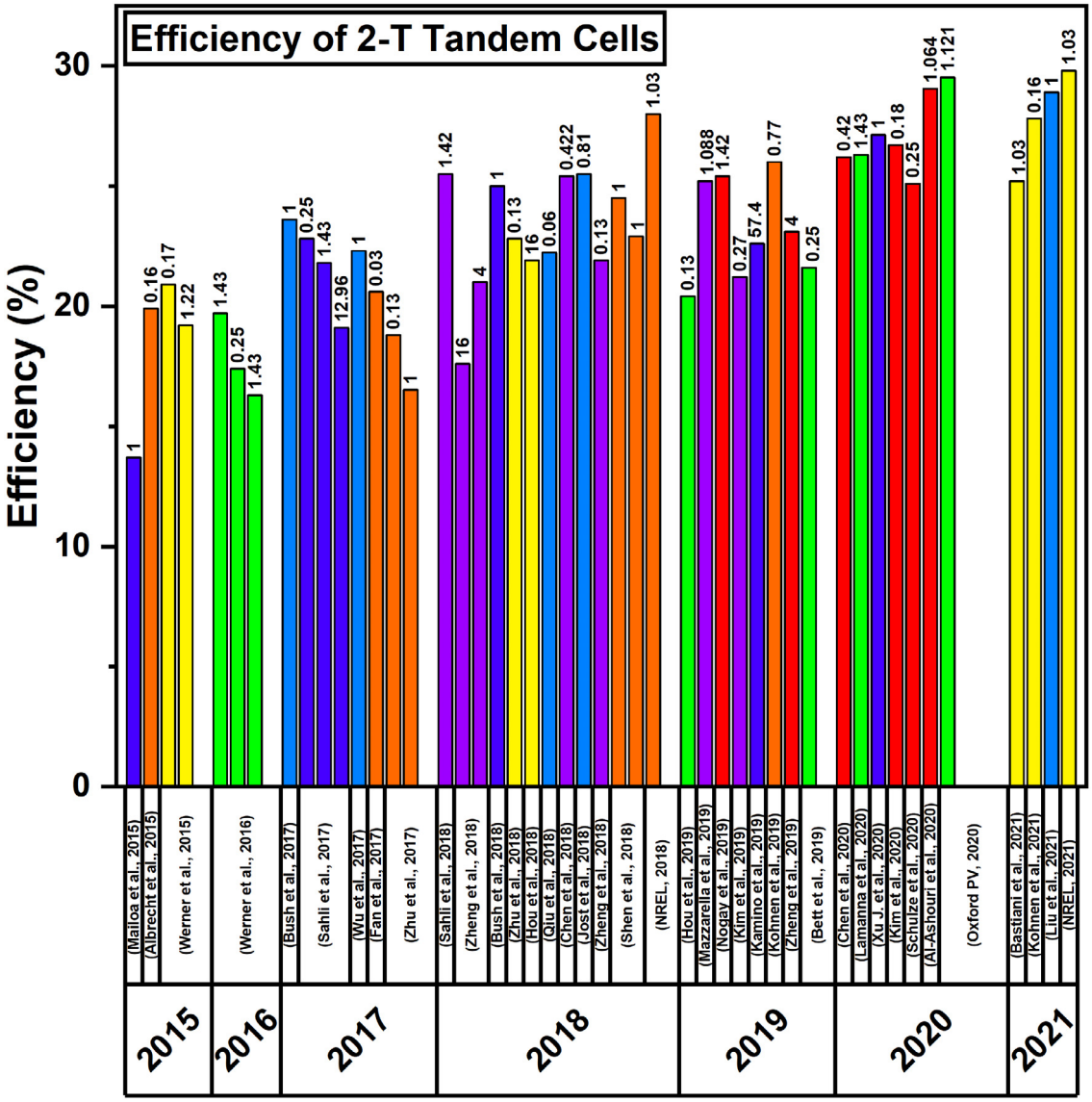

Fig. 8. Evolution of PCE in 4-T c-Si/PSC TSCs with respect to published time. Reverse scan values are considered here. The numbers on top of the bars represent area (mentioned in cm^2) of the developed c-Si/per tandem devices. The references are mentioned for the comparison.

cell at the low-temperature process and achieved device efficiency over 18%. To achieve higher V_{oc} and reduced hysteresis for large size device area, J. Zheng and fellows demonstrated 21.8% steady-state efficiency with the largest cell area of 16 cm^2 by employing a mixed perovskite ($(FAPbI_3)_{0.83}(MAPbBr_3)_{0.17}$) (Zheng et al., 2018b). In another report, Zheng et al. (2019) developed 2-T c-Si/per TSC and implemented $FAMAPbI_{3-x}Br_x$ as the top sub-cell in a tandem configuration having 4 cm^2 area and reported the best values of steady-state efficiency of 23% with a high FF of 81%.

A wide band-gap (1.60 to 1.75 eV) material composed of Cs for the top sub-cell was proposed to tackle long-term stability issues. The Cs doping was performed with $FAPbI_{3-x}Br_x$ and $MAFAPbI_{3-x}Br_x$ perovskites. Recent reports have shown promising results by introducing Cs mixtures, enabling high efficiencies with improved photo, moisture, and thermal stability. For the first time, a mixed cation perovskite absorber layer incorporating the Cs doping concept in c-Si/per tandem structure was established by K. A. Bush and fellows in 2017 (Bush et al., 2017). To achieve enhanced efficiency with improved thermal and environmental stability, they demonstrated $Cs_{0.17}FA_{0.83}Pb(Br_{0.17}I_{0.83})_3$ perovskite (Eg $\approx$ 1.63 eV) as the top sub-cell in monolithic 2-T c-Si/per tandem configuration. By combining top sub-cell (p-i-n configuration) with 1-cm^2 aperture area and infrared-tuned SHJ bottom sub-cell, a 23.6% efficiency was reported. In another work by Sahli et al. (2018b), they improved the PCE to over 25% by fully texturing both sides of the bottom silicon cell and top perovskite subcell. For the top sub-cell, $CsFAPbI_{3-x}Br_x$ based perovskite was used in an inverted configuration. B. Chen and his team used the grain engineering technique by introducing additives to the perovskite in 2-T c-Si/per TSC (Chen et al., 2019). They introduced MACl and MAH_2PO_2 additives in the $Cs_{0.15}(FA_{0.83}MA_{0.17})_{0.85}Pb(I_{0.7}Br_{0.3})_3$ perovskite precursor and achieved 22.4% PCE, a high V_{oc} of 1.83 V, and a small J_{sc} of 16.4 mA/cm^2. With proper optimizing the perovskite composition ($Cs_{0.15}(FA_{0.83}MA_{0.17})_{0.85}Pb(I_{0.8}Br_{0.2})_3$) and $MACl/MAH_2PO_2$ as additives, these J_{sc} and PCE values were improved to 17.8 mA/cm^2 and 25.4%, respectively. Xu et al. (2020a) addressed the low V_{oc} and photoinduced phase segregation issues by introducing (1.67 eV) wide-bandgap planar perovskite top cell using triple-halide alloys (chlorine, bromine, iodine). They demonstrated 27% efficiency from 2-T c-Si/per tandem cell with an area of 1 cm^2. The composition of the top sub-cell was used as $[Cs_{0.22}FA_{0.78}Pb(I_{0.85}Br_{0.15})_3]_{0.97}(MAPbCl_3)_{0.03}$.

Likewise, an alternate cation such as Rb^+ – smaller radii of 1.52 Å than Cs with 1.81 Å radii – has been investigated for highly efficient PSCs with improved thermal and light stability. Wu et al. (2017) developed 2-T c-Si/per monolithic TSC by introducing mesoscopic quadruple cation perovskite ($Cs_{0.07}Rb_{0.03}FA_{0.765}MA_{0.135}PbI_{2.55}Br_{0.45}$) (Eg ≈ 1.62 eV) with a homojunction c-Si bottom sub-cell. By this design, they reported the highest steady-state efficiency of 22.5% for 2-T c-Si/per tandem cell featuring a homojunction. Shen et al. (2018) demonstrated the 2-T c-Si/per TSC without interface and recombination junction. In this approach, they directly placed the top perovskite sub-cell based on $Cs_{0.05}Rb_{0.05}FA_{0.765}MA_{0.135}PbI_{2.55}Br_{0.45}$ absorber layer in direct contact with Si bottom cell. Stabilized efficiencies of 22.9% and 24.1% were reported for homojunction and passivating contact heterojunction bottom devices with 1 cm^2 area, respectively.

4.1.2. Bottom cell

The bottom cell mainly consists of absorption layer, semipermeable (charge transport) layer, transparent front, and back contacts. The absorption layer in bottom cell is silicon, with n and p doped materials forming a p–n junction. Conventionally p-Si refers to crystalline silicon solar cell with n-Si base and p-Si as emitter and vice versa for n-Si solar cells. For tandem applications, c-Si are the most widely used silicon cells consisting of either mono crystalline (single crystal) or poly-crystal (many crystallites) structures. n-type (typically phosphorus-doped) silicon wafers offer several advantages as compared to p-type (typically boron-doped), such as better tolerance to common impurities (Macdonald and Geerligs, 2004), higher bulk lifetime, and no light-induced degradation (LID) (Glunz et al., 2001). n-type silicon solar cells with high efficiency can be potentially more cost-effective than p-type silicon solar cells. As mentioned earlier, the first report on 2-T c-Si/per TSCs was presented by J. P. Mailoa and co-workers, in which, n-type FZ silicon wafer (1–5 Ω cm, 300 μm thickness) (with full area p-type emitter and n-type back surface field (BSF)) was used for the bottom sub-cell (Mailoa et al., 2015). Moreover, the recombination mechanism in the heavily doped regions and metal–silicon contacts restricted the front junction n-type silicon solar cells to achieve high efficiency (Tao and Rohatgi, 2017). Werner et al. (2016b) used n-type FZ Si wafer (1–5 Ω cm, 300 μm thickness) as bottom sub-cell in c-Si/per TSC. The silicon wafer front surface was implanted with boron, and the rear, the textured surface was implanted with phosphorous to form the p-type emitter and n-type BSF regions, respectively. However, the performance of this work was limited by passivation at the front surface of c-Si. To improve surface passivation, a research group at The Australian National University, Canberra, Australia, developed c-Si/per TSC by incorporating an n-type FZ silicon wafer (5 Ω cm) with both sides polished surfaces (Wu et al., 2017). p^+ emitter was used on top of the silicon wafer, and n^+ layer was used at the back side. Both sides surface passivation schemes were developed using Al_2O_3/SiN_x and SiN_x at front and back surfaces, respectively.

M. Jost and co-workers demonstrated the 2-T c-Si/per TSC by incorporating a 260 μm thick n-type c-Si wafer in a rear junction configuration with a polished front side and a textured rear surface (Jošt et al., 2018). To passivate the c-Si surface, 5 nm thick, a-Si layers were grown on both sides of the c-Si wafer. A 5 nm thick p-type a-Si and 95 nm thick n-type nc-SiO_x:H layers were deposited on the textured rear and polished front sides, respectively, using PECVD technique. In similar fashion, many other research groups developed c-Si/per TSCs employing bottom c-Si based on n-type wafers and demonstrated over 25% PCE values.

In the above-mentioned published reports, the entire work was done on n-type c-Si bottom sub-cells besides the dominance of p-type silicon cells in the current PV market. While p-type silicon solar cells dominate the PV market, several academic groups and companies have started investigating p-type c-Si solar cells. Over the past many years, more than 90% of the global PV industry share has been captured by p-type c-Si solar cells, and among which over 70% of p-type c-Si solar cells are based on homojunction with Al-back surface fields (Al-BSFs) (Green, 2016; Pujari et al., 2018). The first report on p-type monocrystalline silicon was demonstrated by Kim et al. (2019) in which they used a p-type 525 μm thick CZ wafer with Al-BSFs as bottom sub-cell. Nogay et al. (2019) demonstrated monolithic 2-T c-Si/per (with 1.43 cm^2 active area) TSC design compatible with low-quality wafers, industrial processes, and thermally stable based on p-type c-Si bottom cell. The tandem device exhibited a 25.1% steady-state PCE value by employing a TopCon/POLO/poly-Si-based cell for the contacts of the c-Si cell rather than low-temperature PECVD-grown a-Si:H or nc-Si:H films.

Table 3 demonstrates detailed J–V parameters for 2-T c-Si/per TSCs. In addition, other parameters such as top and bottom sub-cells selection, devices area with publishing years have been demonstrated. The table indicates the first reported efficiency value of 13.7% achieved from 2-T c-Si/per TSCs. After early reports, c-Si/per tandem technology gained considerable research focus from the scientific community. Initially, the research focused on achieving high-efficiency values with $MAPbI_3$ as an absorber layer for the top sub-cell. Later on, various perovskite compositions were employed, and significant improvement in efficiency values and other factors such as large-scale device fabrication beyond laboratory scale was reported, as indicated. Fig. 9 presents the evolution of efficiency values with various compositions of the perovskite absorber layer. At the initial stage, it exhibits an increased behavior in efficiency values. However, the results demonstrate stable behavior in efficiency values after some time. This specifies that the focus is now towards achieving stable and large-scale devices. It is also shown in the same figure that the majority of the work was performed using SHJ bottom cells.

4.2. 4-T Si/perovskite

4.2.1. Top cell

In 2014, Löper et al. (2015) demonstrated the first example of 4-T c-Si/per TSC design by employing $MAPbI_3$ as a top sub-cell. The reported 13.4% efficiency was a combined sum of 6.2% and 7.2% contributed from the top and bottom sub-cells, respectively. Bailie et al. (2015) used a transparent AgNWs electrode on a perovskite subcell to achieve a semi-transparent device. When combined $MAPbI_3$ based semi-transparent top sub-cell in 4-T mechanically stacked tandem configuration with bottom Si-based sub-cell, they demonstrated 17.9% steady-state efficiency. Werner et al. (2015a) used $MAPbI_3$ in mesoporous configuration with a-Si/c-Si heterojunction bottom cell in tandem configuration and demonstrated over 18% combined efficiency. As mentioned earlier, for an ideal c-Si/per TSC, it is desirable that the bandgap of the top sub-cell should be ∼1.73 eV with 1.1 eV for the c-Si cell (Hossain et al., 2018). However, since the bandgap of $MAPbI_3$ based perovskite is ∼1.55 eV, issues have been raised when attempts were made to tune the bandgap to optimum values (1.7–1.8 eV). For example, at 85 °C temperature (the international standard set by International Electrotechnical Commission, IEC

Table 3
Evolution of efficiency in 2-T c-Si/perovskite Tandem Solar Cells reported from 2015 upto 2021 (PCE values are taken from reverse scan direction), * certified by Fraunhofer or NREL, N/R: Not Reported. ** Other details and J–V parameters are not reported, according to the online publication date.

Year	Perovskite Top Cell	Silicon Bottom Cell	Interface Layer	J_{sc}(mA/cm^2)	V_{oc}(V)	FF	PCE (%)	Steady State/ Certified PCE (%)	Area (cm^2)	Ref.
2015	$MAPbI_3$	Homojunction	n^{++} Si	11.5	1.58	0.75	–	13.7	1.00	Mailoa et al. (2015)
2015	$FAMAPbI_{3-x}Br_x$	SHJ	ITO	14.0	1.78	0.79	19.9	18.1	0.16	Albrecht et al. (2016)
2015	$MAPbI_3$	SHJ	IZO	15.9 16.1	1.69 1.70	0.78 0.71	20.9 19.2	21.2 19.2	0.17 1.22	Werner et al. (2015c)
2016	$MAPbI_3$	SHJ	IZO	16.4	1.72	0.70	19.7	20.5	1.43	Werner et al. (2016b)
2016	$MAPbI_3$	Homojunction	ZTO	15.3 15.3	1.67 1.64	0.67 0.65	17.4 16.3	16.4 16.0	0.25 1.43	Werner et al. (2016a)
2017	$CsFAPbI_{3-x}Br_x$	SHJ	ITO	18.1	1.65	0.79	23.6	23.6*	1.00	Bush et al. (2017)
2017	$CsFAPbI_{3-x}Br_x$	SHJ	nc-Si	16.8 16.5 16.5	1.75 1.78 1.77	0.76 0.74 0.65	22.8 21.8 19.1	22.0 21.2 18.0	0.25 1.43 12.96	Sahli et al. (2018a)
2017	$CsRbFAMAPbI_{3-x}Br_x$	Homojunction	ITO	17.6	1.75	0.72	22.3	22.5	1.00	Wu et al. (2017)
2017	$FAMAI_{3-x}Br_x$	SHJ	ITO	15.3	1.70	0.79	20.6	18.0	0.03	Fan et al. (2017)
2017	$FAMAPbI_{3-x}Br_x$	SHJ	ITO	15.5 14.74	1.71 1.67	0.71 0.67	18.8 16.52	N/R	0.13 1	Zhu et al. (2018b)
2018	$CsFAPbI_{3-x}Br_x$	SHJ	ITO	19.5	1.79	0.73	25.52	25.24*	1.42	Sahli et al. (2018b)
2018	$MAPbI_3$	Homojunction	-	16.1 15.6	1.68 1.66	0.78 0.68	21.0 17.6	20.5 17.1	4.00 16.00	Zheng et al. (2018a)
2018	$CsFAPbI_{3-x}Br_x$	SHJ	ITO	18.4	1.77	0.77	25.0	N/R	1.00	Bush et al. (2018)
2018	$CsFAMAI_{3-x}Br_x$	SHJ	ITO	17.1	1.78	0.74	22.8	N/R	0.13	Zhu et al. (2018a)
2018	$FAMAPbI_{3-x}Br_x$	Homojunction	–	16.2	1.74	0.78	21.9	21.8	16.00	Zheng et al. (2018b)
2018	$CsFAMAPbI_{3-x}Br_x$	SHJ	ITO	16.5	1.65	0.81	22.22	20.6	0.06	Qiu et al. (2018)
2018	$CsFAMAPbI_{3-x}Br_x$	SHJ	ITO	17.8	1.80	0.79	25.4	N/R	0.422	Chen et al. (2019)
2018	$CsFAMAPbI_{3-x}Br_x$	SHJ	ITO	18.5	1.76	0.79	25.5	N/R	0.81	Jošt et al. (2018)
2018	$CsFAMAPbI_{3-x}Br_x$	SHJ	ITO	16.9	1.75	0.74	21.9	N/R	0.13	Hou et al. (2019b)
2018	$CsRbFAMAPbI_{3-x}Br_x$	SHJ (poly-Si) Homojunction	-	17.8 17.2	1.76 1.70	0.78 0.78	24.5 22.9	24.1 22.9	1.00	Shen et al. (2018)
2018	N/R	SHJ	N/R	19.8	1.80	0.79	28.0	28.0**	1.03	NREL (2019)
2019	$CsFAMAPbI_{3-x}Br_x$	SHJ	ITO	16.0	1.83	0.70	20.4	N/R	0.13	Hou et al. (2019a,b)
2019	$CsFAMAPbI_{3-x}Br_x$	SHJ	nc-SiO_x:H	19.02	1.79	0.74	25.2	25.2*	1.088	Mazzarella et al. (2019)
2019	$CsFAPbI_{3-x}Br_x$	SHJ (nc-SiC_x)	nc-Si	19.5	1.74	0.75	25.4	25.1*	1.42	Nogay et al. (2019)
2019	$FAMAPbI_{3-x}Br_x$	Homojunction	ITO	16.1	1.65	0.80	21.2	21.1	0.27	Kim et al. (2019)
2019	$CsFAPbI_{3-x}Br_x$	SHJ	ITO	17.5	1.72	0.75	22.6	22.6	57.4	Kamino et al. (2019)
2019	$CsFAMAPbI_{3-x}Br_x$	SHJ	ITO	19.2	1.76	0.77	26.0	25*	0.77	Köhnen et al. (2019)
2019	$FAMAPbI_{3-x}Br_x$	Homojunction	–	16.5	1.73	0.81	23.1	23	4.00	Zheng et al. (2019)
2019	$FACsPbI_{3-x}Br_x$	SHJ	ITO	15.2	1.83	0.77	21.6	21.6	0.25	Bett et al. (2019)
2020	$CsMAPb(I_{3-x}Br_x)$	SHJ	ITO	19.2	1.82	0.75	26.2	26.1	0.42	Chen et al. (2020)
2020	$CsFAMAPbI_{3-x}Br_x$	SHJ	–	18.81	1.80	0.77	26.3	25.9	1.43	Lamanna et al. (2020)
2020	$[CsFAPb(I_{3-x}Br_x)]_{1-y}(MAPbCl_3)_y$	SHJ	ITO	19.1	1.89	0.75	27.13	27.04	1	Xu et al. (2020a)
2020	$FAMACsPb(I_{3-x}Br_x)_3$	SHJ	ITO	19.2	1.75	0.79	26.7	26.5	0.188	Kim et al. (2020)
2020	$FACsPbI_{3-x}Br_x$	SHJ	ITO	17.7	1.77	0.80	25.1	25.1*	0.25	Schulze et al. (2020)
2020	$CsFAMAPbI_{3-x}Br_x$	SHJ	ITO	19.26	1.90	0.79	29.05	29.15*	1.064	(Al-Ashouri et al., 2020)
2020	N/R	N/R	N/R	20.26	1.88	0.77	–	29.52**	1.121	PV (2020)
2021	$CsFAMAPbI_{3-x}Br_x$	SHJ	ITO	15.36	1.80	0.75	25	25.2	1.03	De Bastiani et al. (2021)
2021	$CsFAMAPbI_{3-x}Br_x$	SHJ	ITO	17.81	1.93	81.05	27.80	27.80	0.16	Köhnen et al. (2021)
2021	–	N/R	2-T	–	–	–	–	29.80**	1.016	NREL (2021)
2021	$CsFAMAPbI_{3-x}Br_x$	SHJ	2-T	19.6	1.87	78.6	28.9	28.2	1.03	Liu et al. (2021)

61646), $MAPbI_3$ is thermally unstable (Conings et al., 2015). In addition, the halide segregation issue in $MAPb[I_{(1-x)}Br_x]_3$ under the light soaking was reported by Hoke et al. (2015). This increases sub-bandgap absorption and a redshift of photoluminescence (PL) under light illumination, which confines the attainable V_{oc}. For the case of $FAPbX_3$ perovskite (a more thermally stable), an increase in the required bandgap did not give rise to the expected improvement in V_{oc} (Eperon et al., 2014). The substitution of iodide with bromide induces a crystal phase transition from a trigonal to a cubic structure. Furthermore, these compositions exhibit charge carrier mobilities of 1 cm^2 V^{-1}s^{-1}, considerably lower than over 20 cm^2 V^{-1}s^{-1} by pure iodide perovskites (Rehman et al., 2015). Hence, these issues restrict such a class of materials in tandem applications.

McMeekin et al. (2016) introduced $FA_{0.83}Cs_{0.17}Pb(I_{0.6}Br_{0.4})_3$ perovskite to address these issues in materials having an optical band gap of ∼1.74 eV with high crystallinity and high compositional photostability. By combining the top sub-cell with a stabilized power output of 12.5% with 7.3% efficiently filtered bottom sub-cell in 4-T c-Si/per tandem design, they demonstrated a combined TSC efficiency of 19.8%. Peng et al. (2017) developed highly efficient solar cells based on $MAPbI_3$ and $Cs_{0.05}(MA_{0.17}FA_{0.83})_{0.95}$-$Pb(I_{0.83}Br_{0.17})_3$. They achieved PCE values of 18.9% and 20.1%, with significant FF values of 0.771 and 0.791, respectively. Similarly, another 4-T c-Si/per TSC was developed by Zhang et al. (2018), in which they achieved 25.7% efficiency. A $(Cs_{0.05}(MA_{0.17}FA_{0.83})_{0.95}$ $Pb(I_{0.9}Br_{0.1})_3)$ based top sub-cell in p–i–n planar configuration was employed.

Duong et al. (2017) explored Rb as an alternative cation to obtain a device with enhanced photostability and improved device performance. Rb has a smaller ionic size of 1.52 Å relative to 1.81 Å of Cs. Moreover, the addition of Rb could boost

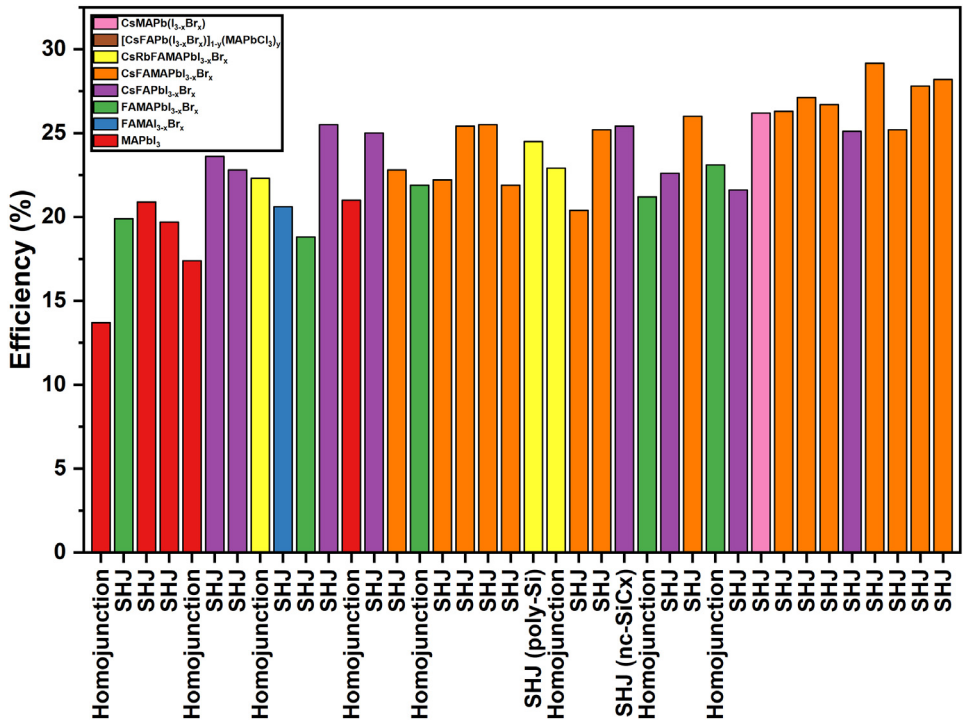

Fig. 9. Evolution of efficiency values with various compositions of the top perovskite and bottom silicon cells in 2-T c-Si/per TSCs.

the device stability by better tuning the Goldschmidt tolerance factor. They exhibited a novel multication structure with the MA/FA/Cs/Rb composition and obtained 1.73 eV bandgap PSCs. Based on these developments, semi-transparent PSCs were fabricated with steady-state PCE of up to 16.0% with improved average transparency of ≈84% in the range of 720 and 1100 nm. When this semi-transparent cell was combined with 23.9% efficient silicon cell, 26.4% (10.4% from the silicon cell) efficiency was achieved in a mechanically stacked 4-T c-Si/per tandem arrangement with negligible hysteresis and improved stability.

4.2.2. Bottom cell

Unlike 2-T, the sub-cells in 4-T c-Si/per TSCs are optically connected but electrically independent from each other, hence, free from the requirement of the current matching and providing ease in optimization for the top and bottom sub-cells, separately. The design concept of the top perovskite sub-cell requires the maximum and efficient transmission of light to the bottom silicon sub-cell. The silicon bottom sub-cell should display an outstanding response to infrared (IR) light to effectively utilize the transmitted light. In addition, silicon bottom sub-cell should also present well-passivated surfaces and contacts. On 4-T c-Si/per TSCs, the first report was presented by P. Löper and co-workers in which they demonstrated 13.4% efficiency (6.2% from the top cell and 7.2% from the bottom cell) (Löper et al., 2015). A 250 μm thick phosphorus-doped FZ c-Si wafer was used as a bottom sub-cell. For the best surface passivation, intrinsic and doped a-Si:H layers were deposited on both sides of the wafer. Bailie et al. (2015) developed 4-T c-Si/per TSC by incorporating mc-Si wafers with high impurity content. The emitter with low sheet resistance (in contrast with ∼100 Ω/□ in the industry) reduces shading losses by increasing bus bar spacing.

For silicon-based tandem applications, amorphous silicon/crystalline silicon (a-Si/c-Si) heterojunction cell is considered an excellent choice due to its high V_{OC} resulting from the separation of the highly recombination-active (Ohmic) contacts from the bulk of the silicon absorber (De Wolf et al., 2012). Werner et al. (2015a) developed a 4-T c-Si/per TSC by employing $MAPbI_3$ in a mesoporous configuration as top sub-cell with a-Si/c-Si heterojunction as a bottom sub-cell and demonstrated a combined efficiency of 19.6%. B. Chen at the Department of Mechanical and Materials Engineering University of Nebraska-Lincoln, USA and co-workers improved the performance of the bottom silicon cell in mechanically stacked tandem configuration by introducing infrared-enhanced silicon heterojunction cells (Chen et al., 2016). They combined infrared-enhanced SHJ cell with a semi-transparent PSC in a mechanically stacked configuration and demonstrated 23% collective efficiency from both cells (16.5% efficiency from top perovskite sub-cell and 6.5% efficiency from the bottom silicon cell).

In order to improve the passivation quality and reduce the recombination at the rear surface, Duong et al. (2016a) developed 4-T c-Si/per TSCs using top perovskite and filtered PERL silicon bottom sub-cell. By this approach, they achieved 20.1% (a combined efficiency from top and bottom sub-cells) efficiency. IBC cells present a simple path to achieve high-efficiency values. In addition, IBC cells are increasingly regarded as a promising road towards large-scale industrial development (Franklin et al., 2016). Taking this into account, Peng et al. (2017) reported 4-T c-Si/per TSC with a 24.5% efficiency by incorporating Cs-mixed halide perovskite as top perovskite sub-cell and highly efficient IBC silicon bottom sub-cell. The fabricated IBC silicon cell was based on a 1.5-Ω cm CZ n-type material. Similarly, a report on the mechanically stacked TSC was published by T. Duong and fellows exhibiting 26.4% combined efficiency (Duong et al., 2017). In this report, PSC with Rb as an alternative cation having 1.73 eV bandgap was stacked on top of IBC silicon bottom sub-cell based on CZ n-type silicon wafer. Quiroz et al. (2018) developed 4-T c-Si/per TSC with PERL and IBC as bottom cells and demonstrated 26.7% and 25.2% efficiencies by perovskite-PERL and perovskite-IBC, respectively. Jaysankar et al. (2018) employed $CsFAPbI_{3-x}Br_x$ based PSC with a bandgap of 1.72 eV as the top sub-cell. They combined the top PSC with IBC c-Si solar cell in a 4-T configuration and achieved 27.1% efficiency. Gharibzadeh et al. (2020) employed the $(FA_{0.83}Cs_{0.17}Pb(I_{1-y}Br_y)_3; 0.24 \leq y \leq 0.56$, 1.65 eV ≤ Eg ≤ 1.85

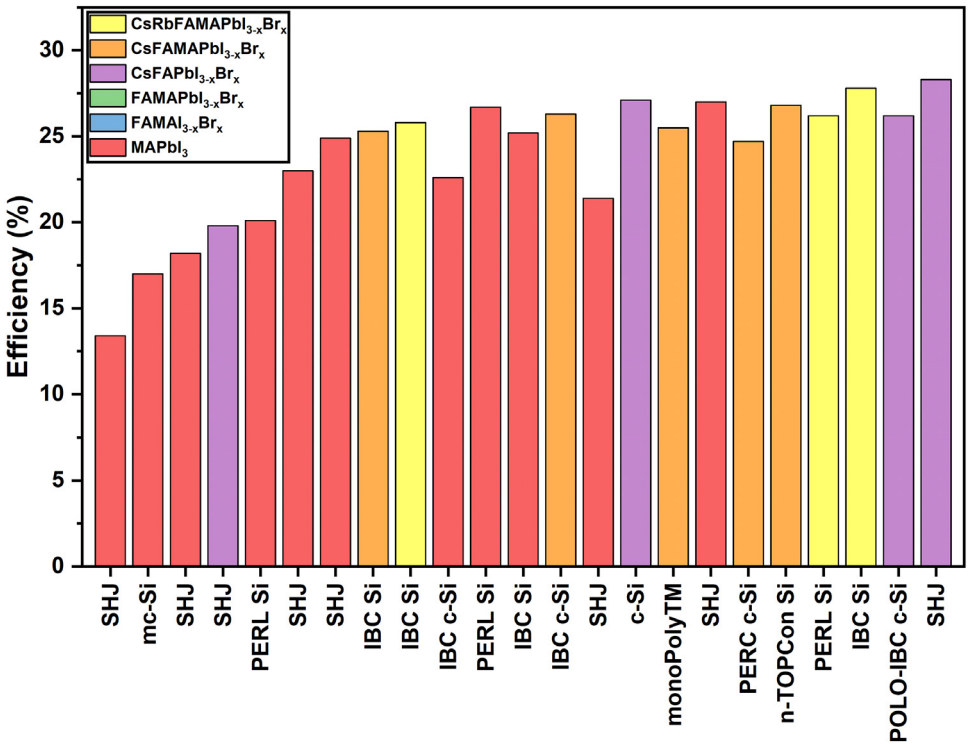

Fig. 10. Evolution of efficiency values with various compositions of the top perovskite and bottom silicon cells in 4-T c-Si/per TSCs.

eV) passivated with a 2D/3D perovskite heterostructure in 4-T c-Si/per tandem configuration and achieved 25.7% efficiency. The bottom silicon cell was fabricated on a 300 μm thick FZ p-type wafer ($\rho = 1.3\ \Omega$ cm) with polycrystalline silicon on oxide-IBC (POLO-IBC) scheme.

Dewi et al. (2019b) developed a 4-T c-Si/per TSC and demonstrated 25.5% efficiency. Their champion device was based on $Cs_{0.05}(MA_{0.17}FA_{0.83})_{0.95}Pb(I_{0.83}Br_{0.17})_3$ top sub-cell absorber layer with a bandgap of 1.58 eV and with an industrial-relevant low-cost n-type Si-based bottom sub-cell. The Si bottom cell was developed on a 6 in. n-type pseudo-square silicon wafer with 180 μm thickness and 2 Ω cm resistivity. The industrial relevant and cost-effective monoPolyTM technology (rear side contact passivation) was deployed for the n-type silicon bottom sub-cell. Up to this point, most of the reported data demonstrated high-efficiency values based on c-Si/per TSCs comprised of a-Si heterojunction (HIT), IBC, and PERL bottom Si sub-cell structures. However, increased recombination losses are associated with these structures. To overcome recombination losses, Rohatgi et al. (2020) developed a 4-T c-Si/per TSC using a low-cost silicon bottom sub-cell and demonstrated 26.7% efficiency. The 4-T c-Si/per tandem device incorporated $CsFAMAPbI_{3-x}Br_x$ based semi-transparent PSC as top sub-cell and a single side n-TOPCon Si (a diffused boron emitter on the front and tunnel oxide assisted n^+ poly-Si/SiO_x passivated contact on the rear) cell as bottom sub-cell. This technology minimizes the complexity and cost related to HIT and IBC silicon cells and virtually removes the doping and metal-induced recombination at the rear surface to enhance its efficiency and response at longer wavelengths.

In Table 4, detailed information on 4-T c-Si/per TSCs with various top and bottom solar cells is presented. In addition, complete J–V parameters of top and bottom cells, including cell areas, are also shown in Table 4. Fig. 10 demonstrates different top perovskite sub-cells concerning bottom sub-cells used for 4-T c-Si/per TSCs. Early reports indicate that c-Si/per TSCs gained considerable research focus from the scientific community. Initially, the research focused on achieving high-efficiency values with $MAPbI_3$ as an absorber layer for the top sub-cell. Later on, numerous multi-cation and bottom silicon technologies were employed, and significant enhancements in efficiency values were reported. Fig. 11 is drawn based on different compositions used in c-Si/per TSCs and their impact on efficiency values. It is indicated that most of the work was performed with $MAPbI_3$ as the top sub-cell in tandem configuration. However, the trend has been changed from scientists and the research community towards multiple cation compositions due to the issues related to $MAPbI_3$ composition (as mentioned earlier).

5. Challenges, limitations, and related perspectives

Besides considerable higher PCEs in both 2-T and 4-T c-Si/per TSCs, few limitations hinder the successful development of these tandem cells from laboratory scale towards commercialization. These limitations are mentioned below and discussed one by one in detail in the following sections.

5.1. 2-T Si/Perovskite

5.1.1. Absorption losses

5.1.1.1. Transparent Electrodes& Optical Transparency
5.1.1.2. Parasitic Absorption in charge transport layers

5.1.2. Reflection losses

5.1.2.1. Anti-reflecting coatings
5.1.2.2. Textured c-Si surfaces

5.1.3. Fabrication Issues
5.1.4. Power conversion efficiency

5.1.4.1. Open circuit voltages
5.1.4.2. Short circuit current density and current matching
5.1.4.3. Fill factor

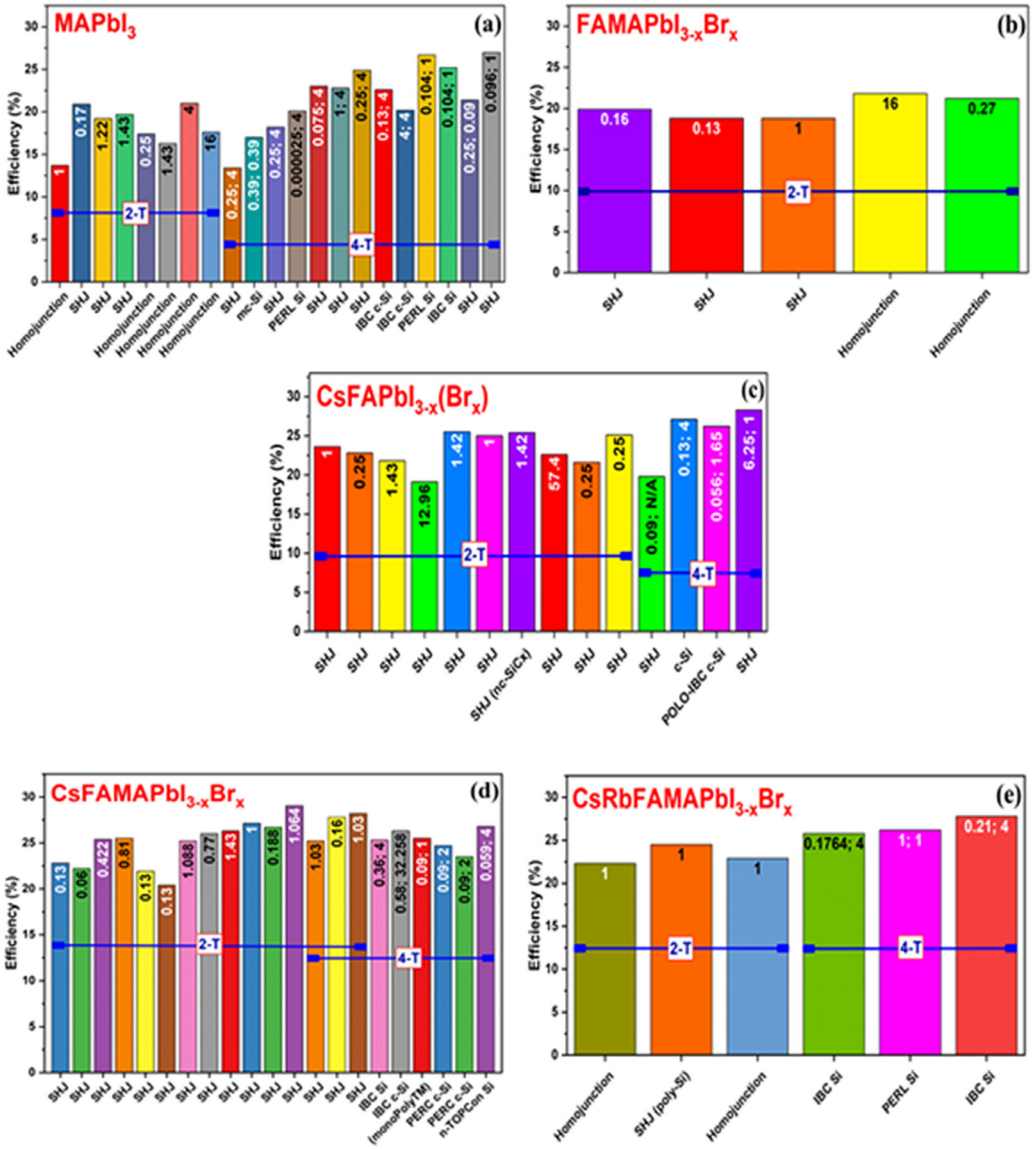

Fig. 11. 2-T and 4-T c-Si/per TSCs efficiencies with single and multiple cations top sub-cells and various bottom silicon sub-cells (a) $MAPbI_3$(b) $FAMAPbI_{3-x}Br_x$ (c) $CsFAPbI_{3-x}Br_x$ (d) $CsFAMAPbI_{3-x}Br_x$ (e) $CsRbFAMAPbI_{3-x}Br_x$ as different top sub-cells. The numbers inside the bars represent area (mentioned in cm^2) of the developed c-Si/per TSCs.

5.1.5. Selection of perovskite material, absorber Thickness
5.1.6. Wide bandgap perovskite solar cells
5.1.7. Inter-band tunneling/recombination junction

5.2. 4-T Si/perovskite

5.2.1. Optical absorption

5.3 Stability issues

5.3.1. Perovskite material stability
5.3.2. Stability of charge transport layers and electrodes
5.3.3. Thermal and environmental stability
5.3.4. Bias dependent degradation mechanisms

5.4. Upscaling

5.1.1. Absorption losses

5.1.1.1. Transparent electrodes & optical transparency. Transparent electrodes are important factors for both 2-T and 4-T c-Si/per tandems. These transparent electrodes must have low sheet resistance and be highly transparent for transmitting the maximum amount of light in a wide spectrum range (UV–VIS) and in the near-infrared (NIR) spectral region for top PSC and bottom silicon sub-cell, respectively. Numerous reports have been published based on transparent electrodes using various materials to improve the transmittance of light. Several research groups demonstrated AgNWs mesh-based electrodes fabricated using spray coating and mechanical transfer deposition techniques (Bailie et al., 2015; Guo et al., 2015; Ahn et al., 2017). However, due to the reaction between silver halide complexes and ions from the perovskite layer, concerns related to stability were raised rapidly (Kato et al., 2015; Bush et al., 2016). Moreover, the complex fabrication techniques and small level reproducibility of AgNWs are other factors that might affect their application towards large-scale fabrication of c-Si/per tandem devices. On the other side, graphene oxide grown by chemical vapor deposition exhibited high transparency. Still, their high sheet resistance up to 350 Ω sq^{-1} (Lang et al., 2015; You et al., 2015)

Table 4
Evolution of efficiency in 4-T c-Si/per Tandem Solar Cells reported from 2014 upto 2021 (PCE values are taken from reverse scan direction), * certified by Fraunhofer or NREL, N/R: Not Reported. ** Module on Cell Value.

Year	Perovskite Top Cell	Silicon Bottom Cell	J_{sc} (Top: Bottom) (mA/cm^2)	V_{oc}(Top: Bottom) (V)	FF (Top: Bottom)	PCE (Top+ Bottom) (%)	Steady State/ Certified PCE (%)	Area (Top: Bottom) (cm^2)	Ref.
2014	$MAPbI_3$	SHJ	14.5; 13.7	0.821; 0.689	0.519; 0.767	6.2 + 7.2 = 13.4	N/R	0.25; 4	Löper et al. (2015)
2014	$MAPbI_3$	mc-Si	17.5; 11.1	0.102; 0.547	0.667; 0.704	12.7 + 4.3 = 17	17.9	0.39; 0.39	Bailie et al. (2015)
2015	$MAPbI_3$	SHJ	17.5; 14.6	0.870; 0.690	0.68; 0.776	10.4 + 7.8 = 18.2	N/R	0.25; 4	Werner et al. (2015a,b,c)
2016	$FACsPbI_{3-x}Br_x$	SHJ	N/R; 13.9	N/R; 0.69	N/R; 0.764	12.5 + 7.3 = 19.8	N/R	0.09; N/R	McMeekin et al. (2016)
2016	$MAPbI_3$	PERL Si	18.8; 16.9	0.95; 0.64	0.69; 0.73	12.2 + 7.9 = 20.1	N/R	0.000025; 4	Duong et al. (2016a,b)
2016	$MAPbI_3$	SHJ	20.6; 12.3	1.08; 0.679	0.741 + 0.779	16.5 + 6.5 = 23.0	N/R	0.075; 4	Chen et al. (2016)
2016	$MAPbI_3$	SHJ	19.3; 15.5 20.1; 15.98	1.057; 0.692 1.072; 0.693	0.70; 0.794 0.74; 0.79	14.3 + 8.5 = 22.8 16.1 + 8.8 = 24.9	23 25.2	1; 4 0.25; 4	Werner et al. (2016a,b,c)
2016	$CsMAFAPbI_{3-x}Br_x$	IBC Si	21.5; 14.2	1.10; 0.69	0.735; 0.81	17.4 + 7.9 = 25.3	24.5	0.36; 4	Peng et al. (2017)
2017	MA/FA/Cs/Rb	IBC Si	19.4; 18.8	1.13; 0.69	0.7; 0.8	15.4 + 10.4 = 25.8	26.4	0.1764; 4	Duong et al. (2017)
2017	$MAPbI_3$	IBC c-Si	20.1 ± 0.4; 15.3 18.2 ± 0.1; 15.3	0.980 ± 0.003; 0.660 0.6396 ± 0.05; 0.660	0.73 ± 0.02; 0.81 0.72 ± 0.03; 0.81	14.4 ± 0.2 + 8.2 = 22.6 ±0.3 12.0 ± 0.3 + 8.2 = 20.2**	N/R N/R	0.13; 4 4; 4	Jaysankar et al. (2017)
2018	$MAPbI_3$	PERL Si IBC	21.0; 17.7 21.0; 17.0	1.098; 0.674 1.098; 0.633	0.741; 0.801 0.741; 0.752	17.1 + 9.6 = 26.7 17.1 + 8.1 = 25.2	N/R N/R	0.104; 1 0.104; 1	Quiroz et al. (2018)
2018	$CsMAFAPbI_{3-x}Br_x$	IBC c-Si	19.4; 17.7	1075; 705	0.781; 0.80	16.3; 10 = 26.3	25.7	0.09; 5 in.	Zhang et al. (2018)
2018	$MAPbI_3$	SHJ	20.7; 15.0	1.0; 0.615	0.712; 0.728	14.7; 6.7 = 21.4	21.4	0.25; 0.09	Kanda et al. (2018)
2018	$CsFAPbI_{3-x}Br_x$	c-Si	15.4 ± 0.11; 24.1 ± 0.03	1.22 ± 0.02; 0.678 ± 0.002	0.734 ± 0.4; 0.812 ± 0.1	13.8 ± 0.1 + 13.3 ± 0.03 = 27.1 ± 0.1	27.1 ± 0.1	0.13; 4	Jaysankar et al. (2018)
2019	$CsMAFAPbI_{3-x}Br_x$	(monoPolyTM)	21.5; 15.2	1.06; 0.63	0.775; 0.811	17.7 + 7.8 = 25.5	N/R	0.09; 1	Dewi et al. (2019a,b)
2019	$MAPbI_3$	SHJ	19.8; 15.6	1.156; 0.698	0.799; 0.80	18.3 + 8.7 = 27.0	N/R	0.096; 1	Wang et al. (2019)
2019	$CsMAFAPbI_{3-x}Br_x$	PERC n-typec-Si	21.52; 15.41 21.52; 15.36	1.060; 0.598 1.060; 0.507	0.77; 0.76 0.77; 0.74	17.7 + 7.0 = 24.7 17.7 + 5.8 = 23.5	N/R	0.09; 2 0.09; 2	Dewi et al. (2019a,b)
2020	$CsFAMAPbI_{3-x}Br_x$	n-TOPCon Si	20.5; 16.6	1.11; 0.675	0.786; 0.796	17.9 + 8.9 = 26.8	26.7	0.059; 4	Rohatgi et al. (2020)
2020	$Rb_{0.05}Cs_{0.095}MA_{0.1425}FA_{0.7125}PbI_2Br$	IBC Si PERL	18.0; 19.6 17.5; 18.6	1.205; 0.697 1.205; 0.675	0.789; 0.78 0.76; 0.80	17.1 + 10.7 = 27.8 16.1 + 10.1 = 26.2	27.7 26.2	0.21; 4 1; 1	Duong et al. (2020)
2020	$FACsPbI_{3-x}Br_x$	POLO-IBC c-Si	19.7; 15.6	1.16; 0.66	0.787; 0.802	18.0 + 8.2 = 26.2	25.7	0.056; 1.65	Gharibzadeh et al. (2020)
2021	$CsFAPbI_{3-x}$	SHJ	21.9; 14.5	1.13; 0.69	0.797; 0.83	19.8 + 8.5 = 28.3	N/R	6.25; 1	Yang et al. (2021)

restricts their successful implementation in c-Si/per tandem cells. Apart from the advantage of process simplicity being offered by other transparent electrodes such as thin evaporated metal layers, i.e., Au (Kanda et al., 2016), Cu/Au (Chen et al., 2016), and MoO_x/Au/MoO_x (Yang et al., 2015b), there is a limitation of strong parasitic absorption related to these transparent electrodes, especially in the perovskite-based top cell sub-bandgap spectral region. For example, a perovskite top cell based on Cu/Au bilayer as transparent electrode demonstrated sub-bandgap absorption between 20 and 30% in the wavelength range of 800–1200 nm, in which silicon bottom cell absorbs.

TCO based on sputtered ITO layer was demonstrated in semi-transparent perovskite cells (Löper et al., 2015). However, the high annealing temperature > 200 °C requirement for ITO deposition was not suitable for sensitive materials used in PSCs. To overcome the post thermal treatment issue, the ITO was replaced with an amorphous TCO based on IZO (Werner et al., 2015c,b) owing to the high carrier mobility of >50 cm^2 V^{-1} s^{-1}, high conductivity and a reasonable low carrier density for limiting free-carrier absorption in the infrared spectrum range. Other appropriate high mobility TCOs based on AZO (Fu et al., 2015) and hydrogenated indium oxide (IO:H) (Werner et al., 2016a) were also presented. Another type of most commonly used TCO based on FTO was employed by the majority of the perovskite community. Even though FTO exhibits high chemical and thermal stability, it is not well adapted for c-Si/per tandem applications due to its high free-carrier absorption in the near-infrared spectral region. In a 4-T tandem configuration, in which FTO was employed as a transparent electrode, the current in the bottom sub-cell was drastically reduced, compared to the less absorbing cell with ITO as TCO (Werner et al., 2015a).

Another major limitation was the fabrication method used in transparent electrodes by sputtering. When these transparent electrodes were deposited on top of the perovskite layers, there were slight chances of damaging the underneath charge transport layers. To address this issue, buffer layers were introduced in between organic charge transport layers and transparent electrodes. MoO_x is a class of thermally evaporated transition metal oxides (TMOs), generally used as a p-type contact and a buffer layer to protect underlying soft layers during the sputtering process (Fu et al., 2015; Löper et al., 2015; Werner et al., 2016a,c). However, during the sputtering process, the MoO_x was affected by Ar plasma exposure, which increased the absorption of MoO_x due to a large number of oxygen vacancies (Werner et al., 2016c). A more resilient metal oxide based on tungsten oxide (WO_x) was proposed as a replacement to MoO_x. Alternate options could be ZnO nanoparticles (Bush et al., 2016; Fu et al., 2016) and SnO_2 thin films deposited by atomic layer deposition (Bush et al., 2017).

5.1.1.2. Parasitic absorption in charge transport layers. Issue related to c-Si/per TSCs is parasitic absorption by charge transport layers, such as the most commonly used spiro-OMeTAD as the HTL. Spiro-OMeTAD layer demonstrated strong parasitic absorption in the blue and UV spectral region during the illumination. When the sprio-OMeTAD layer was placed on top of the perovskite absorber layer in n–i–p architecture in a monolithic tandem cell, the device performance was limited with a current loss of 1–2 mA cm^{-2}. To reduce the parasitic absorption by spiro-OMeTAD layer, a variety of HTLs based on small molecule semiconductors i.e. N,N'-bis(naphthalen-1-yl)-N,N'-bis(phenyl)-benzidine (NPB), 2,2',7,7'-Tetra(N,N-ditolyl) amino-9,9- spirobifluorene (spiro-TTB), or N4,N4,N400,N400-tetra([1,10-biphenyl]-4-yl)-[1,10:40,100-terphenyl]-4,400-diamine (TaTm) (Belisle et al., 2016; Momblona et al., 2016) along with the inorganic NiO_x and copper thiocyanate materials (i.e. CuSCN) with high bandgaps were proposed (Jung et al., 2015; Ke et al., 2015; Liu et al., 2016). Similarly, with lower parasitic absorption, thin layers based on fullerenes, such as buckyball (C_{60}) or phenyl-C_{61}-butyric-acid-methyl-ester (PCBM), were demonstrated as potential ETLs in both the p–i–n (Werner et al., 2016b) and the n–i–p (Fu et al., 2016; Bush et al., 2017) arrangements.

With reduced parasitic and optical absorption from the CuSCN as HTL and solution-processed AgNWs as the bottom electrodes, Quiroz et al. (2018) developed a semi-transparent solar cell with an efficiency of up to 17.1%. Finally, in a 4-T c-Si/per mechanically stacked tandem configuration with PERL and IBC as bottom cells, 26.7% and 25.2% efficiencies by perovskite-PERL and perovskite-IBC, respectively, were reported. To further reduce parasitic absorption in the charge transport layers, many efforts would be required to search for stable organic or inorganic materials owing to high optical bandgap with reduced thicknesses, which form deposition on perovskite absorber layer without inducing damage.

5.1.2. Reflection losses

Since light passes through the top perovskite sub-cell to reach the bottom silicon sub-cell in both 2 and 4-T c-Si/per tandem configurations. Therefore, it is desired to enhance NIR light transmitted through top perovskite cell to bottom silicon cell without any losses. Mainly reflection losses are caused due to the polished front surfaces (front transparent electrode and the flat Si bottom-cell). Moreover, the differences in refractive index at the front surface (between the front electrode and air) and the interfaces in the top and bottom sub-cells layers stack cause reflection losses. Other factors affecting reflection losses originate from the thickness and refractive index of TCO layers when used as intermediate/recombination junction between top and bottom sub-cells in c-Si/per tandems (Albrecht et al., 2016; Werner et al., 2016a). By tuning the refractive index of TCO layers, reflection losses can be reduced; as reported, the nc-SiO_x:H layers ($1.8 < n < 4$) were replaced with TCOs ($n \approx 1.8–2$) in thin-film silicon TSCs (Söderström et al., 2009; Haug and Ballif, 2015). Similarly, results demonstrated reduced parasitic absorption and reflection losses in the red and infrared region, including improved photogenerated current in the silicon bottom cell using nc-SiO_x:H layer as an interference/recombination junction between Si/per monolithic TSCs (Sahli et al., 2018a,b). Jošt et al. (2018) employed textured LM foil on the front side of the PSC in a tandem structure (Fig. 12a). By employing this LM foil, they reduced the reflection losses, enhanced light trapping, and significantly improved the device efficiency from 23.4% to 25.5%.

Besides optimizing the thickness and refractive index of TCOs and other layers, a few light management approaches can be employed to avoid/reduce the reflection losses:

1. Anti-reflecting coatings
2. Textured c-Si surfaces

5.1.2.1. Anti-reflecting coatings. Using anti-reflecting coatings (ARCs) is a great idea to reduce reflection losses. In ARCs, lithium fluoride (LiF) and magnesium fluoride (MgF_2) are the best suitable choices and are widely used due to their high transparency and low refractive index (Shanmugam et al., 2020; Xu et al., 2020b). For example, S. Albrecht and co fellows reduced the reflection losses at the air/ITO interface of monolithic c-Si/per TSC by thermally evaporated LiF layer on top of the cell. By introducing the LiF layer as ARC, they reported 1.5 mA/cm^2 higher photogenerated current in the bottom silicon sub-cell. In addition, with ARC, the two sub-cells demonstrated closed matched current, i.e., 14.7 and 14.0 mA/cm^2, from the top perovskite and bottom silicon sub-cells under AM 1.5G spectra, respectively (Albrecht et al., 2016). Similarly, to reduce the front side reflection, Bett et al. (2019) applied the 90 nm MgF_2 as ARC using thermal evaporation on top of the monolithic c-Si/per TSC. By this approach,

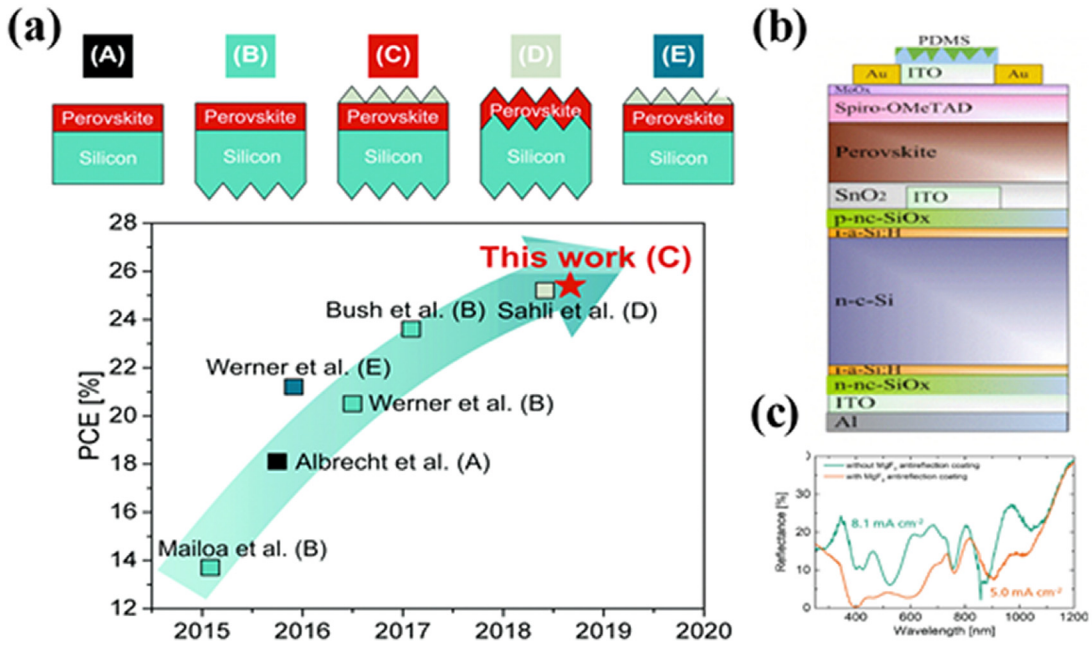

Fig. 12. Various reported textured configurations for experimentally realized c-Si/perovskite tandem solar cells and their effect on the PCE enhancement as indicated in the figure. Device schematics represent the location of the texture position. Device (A) is a fully flat device. Device (B) is a back-side textured device. Device (C) is a back-side textured device with the LM foil. Device (D) is a both-side textured device whereas device (E) is a fully flat device with the LM foil. Republished with permission of Royal Society of Chemistry, from Jošt et al. (2018), Copyright 2018; permission conveyed through Copyright Clearance Center, Inc. (b) The schematic of the monolithic c-Si/perovskite tandem solar cell with AR foil of PDMS on top of the structure, Reprinted from Hou et al. (2019a), Copyright 2018, with permission from Elsevier. (c) Reflectance of tandem solar cells without and with MgF_2 ARC. The ARC strongly reduces the reflection losses from 8.1 mA cm^{-2} to 5.0 mA cm^{-2}, Reprinted from Bett et al. (2019), Copyright 2019, with permission from Wiley.

they reduced the combined reflection losses from 8.1 mA/cm^2 to 5.0 mA/cm^2 (Fig. 12c).

Reports found that the formation of patterned PDMS scattering layer on the top surface of a solar cell could overcome the reflection losses (Escarré et al., 2012; Jošt et al., 2017; Manzoor et al., 2017; Bush et al., 2018; Lipovšek et al., 2018). To boost up light absorption, Hou et al. (2019a) have demonstrated light management ARC using PDMS polymer with inverted random pyramidal textures having three different pyramid size ranges (1–3 μm, 3–8 μm, 8–15 μm) (Fig. 12b). Using a 3-8 μm pyramid size textured layer, they increased Jsc value to 16.89 mA/cm^2 and efficiency value to 21.93% compared to the J_{sc} of 15.17 mA/cm^2 and PCE of 19.38% values with devices without PDMS. To achieve higher efficiency with improved current density, Werner et al. (2015c) processed device fabrication of monolithic planar c-Si/per heterojunction tandem cells at temperature values below 150 °C and reported efficiencies of up to 21.2 and 19.2% for cell areas of 0.17 and 1.22 cm^2, respectively. During the characterization, they applied microtextured ARF on the front side of the device. The reported J–V parameters with and without ARF are mentioned in Table 5 for both device areas with 0.17 and 1.22 cm^2. Using the ARF, the reflection losses were drastically reduced and the current was increased by ∼ 10% in the top cell and by ∼ 16% in the bottom cell.

5.1.2.2. Textured c-Si surfaces. One of the additional measures to achieve high power conversion efficiencies is efficient light management in Si/per TSCs. Besides applying anti-reflective coatings or foils on the front surface of the top perovskite sub-cell in tandem design, numerous strategies have been adopted to reduce the reflection losses at the bottom silicon sub-cell. In this regard, textured silicon wafers can be exploited for efficient light management. Back-side, front side, and both-sides texturing of perovskite top cell and bottom silicon cell come under this category (Fig. 13b–f).

For the first time, a monolithic c-Si/per TSC with a backside textured bottom silicon cell was developed by a joint collaboration among Stanford University, USA, Arizona State University, USA, Massachusetts Institute of Technology, USA, and the University of Oxford, UK (Bush et al., 2017). The champion device exhibited 23.6% PCE with improved thermal and environmental stability. To overcome increased potential production costs, strong reflection losses, and weak light trapping incurred due to polished front surface of bottom c-Si sub-cells, F. Sahli and coworkers developed fully textured monolithic c-Si/per TSCs (Sahli et al., 2018b). The double side texturing concept minimized the reflection losses up to 1.64 mA/cm^2 from 3.14 mA/cm^2 induced by the polished front side of bottom cells in the wavelength range (λ = 360–1200 nm). In addition, Kanda et al. (2018) compared the optic and PV characteristics of flat and textured silicon surfaces in mechanically stacked c-Si/per TSCs. They proposed that textured silicon surfaces reduce the reflection more effectively in the wavelength range (750–1050 nm) and enhance the current density value relative to flat silicon surfaces.

5.1.3. Fabrication issues

In 2-T c-Si/per TSCs, the top perovskite cell is fabricated directly on the bottom silicon cell. The current should be matched in both sub-cells for best performance. This is possible if the sub-cells are integrated into a well-aligned configuration, and there are no reflection losses and current leakage issues. However, the process of developing top cell layers is limited by the bottom silicon cell for several reasons. For instance, planar surfaces, required temperature, employed solvents, and fabrication schemes. This complicates the development of the tandem structure process since all the layers are monolithically stacked. Numerous research efforts have been demonstrated to address fabrication issues in monolithic tandem structures. One of such efforts was presented by Lamanna et al. (2020), in which they developed a state-of-the-art and highly efficient 2-T c-Si/per TSC. They designed mesoscopic perovskite top sub-cell in a mechanically stacked configuration with the double-sided textured SHJ bottom sub-cell. The

Table 5
J–V Parameters for c-Si/per TSC with and without anti-reflective foil (ARF) in both forward and reverse direction for area 0.17 and 1.22 cm^2, Measured at a Scan Rate of 100 mV/s.
Source: Reprinted (adapted) with permission from (Werner et al. 2015).
© 2015 American Chemical Society

S. No.		Aperture Area (cm^2)	Direction	V_{oc} (mV)	J_{sc} (mA/cm^2)	FF (%)	PCE (%)
1	w/o ARF	1.22	Reverse	1694	13.4	72.9	16.6
2		1.22	Forward	1700	13.4	75.5	17.2
3	with ARF	1.22	Reverse	1701	16.1	70.1	19.2
4		1.22	Forward	1703	16.1	70.9	19.5
5	w/o ARF	0.17	Reverse	1668	13.6	76.7	17.4
6		0.17	Forward	1670	13.8	78.6	18.1
7	with ARF	0.17	Reverse	1690	15.9	77.6	20.9
8		0.17	Forward	1692	15.8	79.9	21.4

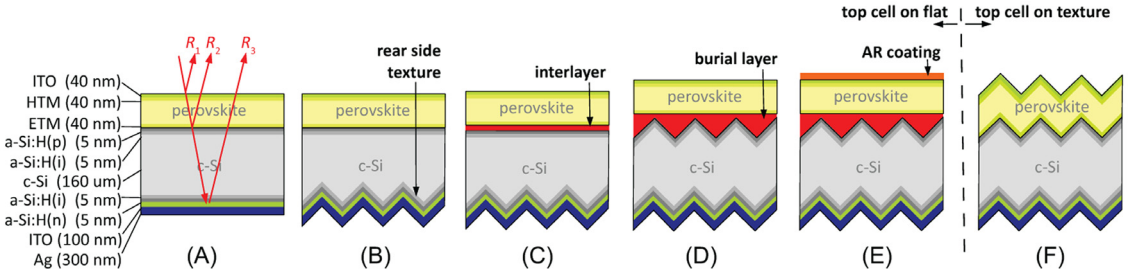

Fig. 13. C-Si/per tandem devices with flat and textured surfaces, (A) both sides flat surface, (B–C) rear side textured (D–F) Front and rear sides textured. The layer thicknesses and the reflection losses R_1, R_2, and R_3 are shown.
Source: Reprinted/Adapted with permission from Santbergen et al. (2016) © The Optical Society.

champion tandem device exhibited 26.3% PCE with a stabilized value of 25.9% over an area of 1.43 cm^2.

5.1.4. Power conversion efficiency

The efficiency of a solar cell is defined as the ratio of the output power (P_{out}) to the input power, (P_{in}) and can be determined by the following equations.

$$\eta = \frac{P_{out}}{P_{in}} \tag{1}$$

$$P_{out} = V_{oc} I_{sc} FF \tag{2}$$

$$\eta = \frac{V_{oc} I_{sc} FF}{P_{in}} \tag{3}$$

Where: η represents efficiency
I_{sc} represents short-circuit current;
V_{oc} represents open-circuit voltage and
FF represents fill factor

From Eq. (3), it is clear that the efficiency of solar cells is strongly dependent on values of V_{oc}, I_{sc}, and FF. Greater these values highest will be the efficiency. However, losses in these values will limit the performance of c-Si/per TSCs to achieve higher efficiency values. In the subsequent sections, our point of discussion will be related to losses associated with V_{oc}, I_{sc}, and FF.

5.1.4.1. Open circuit voltage. The V_{oc} is related to the bandgap of the absorber material such that increasing the bandgap increases the V_{oc}. In c-Si/per TSCs, reduced V_{oc} produced by the high bandgap (Eg ≈ 1.60–1.85 eV) perovskite top sub-cell is a crucial factor limiting device performance. Photo-induced halide segregation, Br-related trap states, and non-optimized contact layers are the main factors influencing the voltage losses (Leijtens et al., 2018; Jošt et al., 2020). Dedicated research efforts have been focused on overcoming these issues by optimizing compositional, interfacial, optical, and architecture engineering. By adopting proper optimization in device contacts and the perovskite composition, K. A. Bush and co-fellows minimized the V_{oc} losses to over 0.58 V compared to previously reported loss of 0.66 V by the same group (Bush et al., 2017, 2018). However, this value is still far from the ideal S–Q voltage loss of 0.27 V (Bush et al., 2018). In addition, Chen et al. (2019) introduced MACl and MAH_2PO_2 additives in the wide bandgap perovskite precursor and reduced V_{oc} deficit to 0.49 V. Jaysankar et al. (2018) have examined the factors affecting V_{oc} in wide-bandgap mixed halide PSCs based on $CsFAPbI_{3-x}Br_x$ perovskites with a bandgap of 1.72 eV. The passivation of the perovskite/ HTL interface quality was enhanced by introducing Al_2O_3 in between perovskite/ HTL layers, which improved V_{oc} and reduced V_{oc} deficit to 0.5 V in wide bandgap $CsFAPbI_{3-x}Br_x$ based solar cell. Another major issue related to V_{oc} deficit in wide-bandgap PSCs is the unmatching of energy levels. Since an increase in the bandgap typically changes the conduction band to higher energy levels. Therefore, suitable charge extraction/transportation layers must be employed to increase V_{oc} to achieve energy conversion efficiencies as high as 18.5% with a bandgap of 1.71 eV (Lin et al., 2017).

5.1.4.2. Short circuit current density and current matching. In 2-T c-Si/per TSCs, the two sub-cells are connected in series such that perovskite top sub-cells are fabricated on bottom silicon sub-cells; therefore, the two sub-cells should generate matched current to achieve maximum output power. If the current in the two sub-cells is unmatched, then the overall current in a tandem cell will be limited by the sub-cell producing a low current. The theoretical upper limit (S–Q limit) of the J_{sc} is found to be 46 mA/cm^2 for the single junction c-Si solar cells (Hossain et al., 2018, 2019). Based on these findings, the maximum J_{sc} generation in each sub-cell should be 23 mA/cm^2 in c-Si/per monolithic TSCs under the matched current condition. E. Kohnen and fellows improved the c-Si/per TSC performance and enabled the matched current densities of the two sub-cells (Köhnen et al., 2019). By optical optimization and fine-tuning of the thicknesses of the perovskite absorber layer, top front electrode (IZO), and the intermediate layer (nc-SiO_x:H), a stabilized PCE value of 26.0% (enhanced from 25.0%) with improved J_{sc} by 1.4 mA/cm^2 was

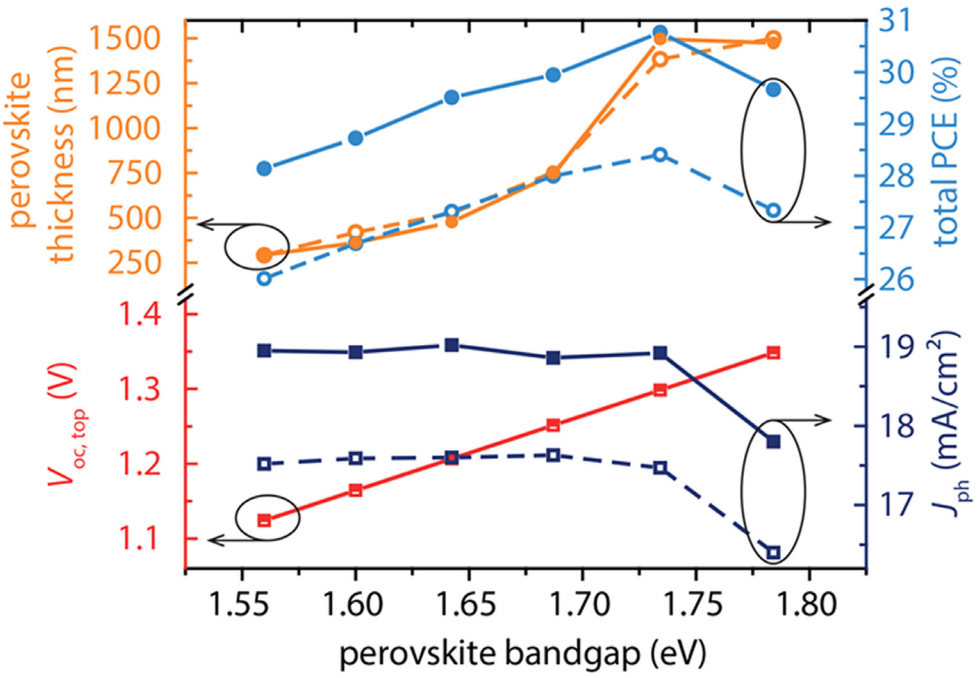

Fig. 14. Perovskite top sub-cell bandgap and its impact on, V_{oc} and optimized film thickness of the perovskite sub-cell (Left scale), J_{sc} and tandem cell efficiency (Right scale) in silicon/perovskite tandem solar cells. Dashed lines represent the regular structure, and solid lines represent the inverted structure.
Source: Reprinted/Adapted with permission from Jäger et al. (2017) © The Optical Society.

demonstrated. In addition, integrated current density value of 39.46% ($J_{perovskite} = 20.19$ mA/cm^2 & $J_{c-si} = 19.27$ mA/cm^2) with 0.92 mA/cm^2 mismatched current density was reported.

5.1.4.3. Fill factor. Like I_{sc} and $V_{oc,}$ FF is also an important parameter that influences the efficiency (performance) of a solar cell. By varying the series and shunt resistances using simulation, M. Boccard and C. Ballif studied the variation in FF and its impact on the performance for single junction and c-Si/per TSCs (Boccard and Ballif, 2020). They demonstrated that FF losses are associated with high series resistance for single-junction solar cells, while for the tandem design, it has a small impact on FF. However, for the case of c-Si/per TSC, variations in parallel resistance strongly affect the FF of the tandem device relative to the single-junction device.

5.1.5. Selection of perovskite material, absorber thickness

$MAPbI_3$ is the most extensively used perovskite absorber material with a E_g of ≈1.55 eV. However, as mentioned earlier, this value is lower than the optimum value of ≈1.73 eV required for an ideal top sub-cell in c-Si/per monolithic tandems. A corresponding increase in Voc can be achieved by improving the bandgap while maintaining material and interface quality. By replacing iodide with bromide, the bandgap of $MAPbI_3$ based perovskites can easily be tuned between 1.55 and over 2 eV (Eperon et al., 2014). However, stability issues were raised in these compounds regarding photoinduced phase segregation and phase separation (Slotcavage et al., 2016; Hoke et al., 2015; Brunetti et al., 2016; Barker et al., 2017). Reports were demonstrated related to phase stability by introducing perovskite materials having Cs and FA cations, replacing methylammonium either partially or fully (Saliba et al., 2016b). McMeekin et al. (2016) demonstrated PCE of 17% for PSC with a V_{oc} of 1.2 V (near to the theoretical value of 1.42 V) by introducing ($FA_{0.83}Cs_{0.17}Pb(I_{0.6}Br_{0.4})_3$) absorber material with an optical bandgap of 1.74 eV. Beal et al. (2016) studied the stability issues in perovskite absorbers and exhibited the evaporation of methylammonium cation under thermal treatment during the process, and proposed cesium as a possible replacement to improve the thermal stability. By employing $CsPb(Br_xI_{1-x})_3$ as an absorber layer, they enhanced thermal and optical stability with stabilized PCE of 6.5% and a bandgap of 1.9 eV. However, due to the nonoptimized deposition process and a very thin absorber layer (∼ 150 nm), the cell performance was limited to reduced FF, J_{sc}, and V_{oc}. With a bandgap of 1.73 eV, the $CsPbI_3$ based composition was found to be a capable choice for tandem applications (Ahmad et al., 2017). However, the instability of its photoactive phase at room temperature is a major issue (Frolova et al., 2016).

Issues limiting the photocurrent in the perovskite top sub-cell are the thickness and layer quality of the perovskite absorber layer. The top perovskite absorber layer should be thin enough to pass light to the bottom silicon sub-cell more efficiently. Jäger and fellows investigated the relationship between perovskite layer thickness and the top cell (regular and inverted structures) bandgap in the tandem configuration (Jäger et al., 2017). Their results indicate (Fig. 14) that perovskite absorber layer thickness should be ≈1.3 μm (inverted structure) and ≈1.5 μm (regular structure) for an ideal bandgap of 1.73 eV to yield an efficiency of over 30%. However, achieving this amount of thickness at an experimental level is challenging while maintaining high material quality.

5.1.6. Wide bandgap perovskite solar cells

The theoretically attainable efficiency (radiative limit) for both c-Si/per tandem structures can be determined using detailed-balance calculations. The efficiency limit for both configurations was found to be around 45%, with steeply decreasing values for top cell bandgaps in the case of the two-terminal tandem cell because of the current matching limitation. The ideal top cell bandgap for 2-T and 4-T structures is 1.73 and 1.82 eV, respectively (Fig. 15) (Dupre et al., 2018). Even though the optimal top cell bandgap for ideal 2-T tandem cells is 1.73 eV, current matching can still be achieved in devices with bandgaps of 1.6–1.65 eV. Jäger et al. (2021) and Bowman et al. (2021) studied the current matching in 2-T tandem cells using luminescent coupling (LC). They concluded the utilization of 1.60–1.65 eV bandgap perovskites for optimal performance and that LC minimizes the effect

Table 6
Inter-band tunneling/recombination junction wise Efficiency Table. (PCE values are taken from reverse scan direction). * Certified by Fraunhofer or NREL.

Recombination Junction	Perovskite Cell	Silicon Cell	J_{sc} (mA/cm^2)	V_{oc} (V)	FF	PCE (%)	Area (cm^2)	Ref
n^{++}/p^{++} Si	$MAPbI_3$	Homo-junction	11.5	1.58	0.75	13.7*	1.00	Mailoa et al. (2015)
nc-Si:H(n^+)/ nc-Si:H(p^+)	$CsFAPbI_{3-x}Br_x$	SHJ	16.8 16.5 16.5	1.75 1.78 1.77	0.76 0.74 0.65	22.8 21.8 19.1	0.25 1.43 12.96	Sahli et al. (2018a)

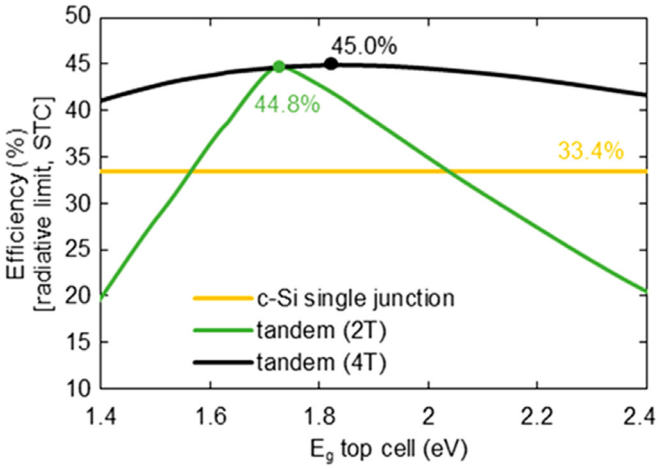

Fig. 15. Radiative-limit efficiency of tandems (two-terminal and four-terminal configurations) with a c-Si bottom cell (Eg = 1.12 eV at 25 °C) as a function of the top cell bandgap.
Source: Reprinted (adapted) with permission from Dupre et al. (2018).
© 2018 American Chemical Society.

of current mismatch. Since the current matching is not required in the 4-T design, the optimal top cell bandgap is much wider in this class. Based on the comparison of reported data on bandgap tunability between 1.2 and 2.4 eV and their effects on perovskite device performance, Unger et al. (2017) demonstrated higher values of V_{oc} for bandgaps of ≈1.7 eV and lower V_{oc} for larger bandgaps due to strong deviations attributed to phase separation. Jaysankar et al. (2018) have examined the factors affecting V_{oc} in wide-bandgap mixed halide PSCs. In their work, $CsFAPbI_{3-x}Br_x$ based PSC with a bandgap of 1.72 eV was demonstrated, which showed V_{oc} of 1.22 eV.

5.1.7. Inter-band tunneling/recombination junction

In 2-T c-Si/per TSCs, the top and bottom sub-cells are combined in series through intermediate layers or tunneling or recombination junction, which enable the charge recombination between the two sub-cells. As mentioned earlier, a variety of TCOs was employed as intermediate layers. However, several drawbacks are associated with these TCOs, such as losses due to high parasitic absorption above 800 nm wavelength (because of free-carrier absorption) (Holman et al., 2012), high reflection at the TCO/silicon interface as a result of inadequate refractive index matching with silicon (Grant et al., 2016), and high lateral conductivity, encouraging shunt paths through the top cell (Sahli et al., 2018a).

The first report on inter-band tunneling junction was demonstrated by J. P. Mailoa and co-fellows (Mailoa et al., 2015). They used p^{++}/n^{++} silicon tunnel junction deposited through PECVD and demonstrated 13.7% efficiency to enable electrical coupling between the two sub-cells with reduced parasitic absorption. However, this work was limited due to high parasitic absorption generated by the spiro-OMeTAD layer and required high annealing temperature unsuitable with SHJ based technology. Owing to low temperature (< 200 °C) processing and compatibility with SHJ, Sahli et al. (2018a) employed hydrogenated nc-Si:H as a recombination junction between two sub-cells to mitigate optical losses as produced by TCOs. This recombination junction exhibited higher shunt resistances enabled 2-T c-Si/per TSCs to achieve 18% steady-state efficiency for a 12.96 cm^2 large size active area. Table 6 demonstrates detailed information about top and bottom sub-cells, including J–V parameters and device areas.

5.2. 4-T Si/Perovskite

5.2.1. Optical absorption

In 4-T c-Si/per TSCs, the top and bottom sub-cells are optically connected and electrically isolated with each other. Unlike 2-T c-Si/per TSCs, in this design, the two sub-cells are independent of each other; therefore, a more significant number of transparent electrodes are required to pass the light efficiently from top to bottom cell. These transparent electrodes transmit the light from top to bottom cell and play a critical role in optical absorption, as these electrodes absorb a significant part of the incident light.

5.3. Stability issues

Since the beginning of c-Si/per TSCs development, stability has remained a significant issue. In a 2-T tandem design, the two subcells are arranged in series; the failure of one subcell or the recombination layer will degrade complete TSCs. The two parallelly connected subcells in 4-T TSCs are only optically coupled. If one of the two subcells fails electronically, the device's overall performance will be harmed, but it will continue to function with reduced power output. Furthermore, the PSCs degradation under UV light is also a primary cause of instability (Lee et al., 2016). The UV layers pass directly through the PSC, causing instability in the PSC and, as a result, TSCs. This will lead to the degradation of complete TSCs in 2-T and low-performance output in 4-T (mechanically stacked) configurations. However, in the case of 4-T optically coupled TSCs, the UV layers can be directly passed to the bottom silicon cell through a beam splitter, reducing the chances of PSC degradation and thus improving TSCs performance. The stability issues for perovskite-based tandem devices are mainly attributed to the following factors:

1. Perovskite material stability
2. Stability of charge transport layers and electrodes
3. Thermal and environmental stability
4. Bias dependent degradation mechanisms

5.3.1. Perovskite material stability

The perovskite layer must retain its crystallographic phase during device operation in PV applications. At room temperature, the $MAPbI_3$ exhibits a tetragonal phase, and at an operational temperature range of ≈60 °C of a PV module, phase transition shifts to a cubic phase. The volatility of methylammonium cation from the cell under thermal stress has also been reported (Conings et al., 2015). In addition, with partial substitution of the iodide with bromide, the increase in the bandgap of $MAPbI_3$ based PSCs was demonstrated to design new compounds. However, due

to phase segregation, these new compounds exhibited instability under light (Hoke et al., 2015). Therefore, this is clear evidence that these absorber layers will not be a considerable choice towards commercialization. Improvements in terms of structural stability were demonstrated by introducing larger cations like FA as a substitution to methylammonium cation. With a composition of FA–MA mixed-cation and I–Br mixed halide, a certified PCE of up to 22.1% was achieved for single-junction PSCs. However, thermal instability is a major concern for this type of composition. Among the numerous factors influencing the stability of PSCs, ion migration in perovskites is intrinsic and cannot be eliminated through device encapsulation. PSCs have been shown to experience ion migration, which causes photocurrent hysteresis and is commonly regarded as one of the contributing factors for device instability (Miyano et al., 2016; Yuan and Huang, 2016). However, it is unconfirmed yet if ions in hybrid perovskites, notably the freely mobile (I^-), can drift through the recombination layer to the bottom cell. If this occurs during operation of a tandem cell, the immobilized ions will certainly destroy the underneath layers of the bottom cells, consequently affecting the device's operational stability.

5.3.2. Stability of charge transport layers and electrodes

Besides the stability of the perovskite absorber layer, stability related to charge transport layers and electrodes is also an important factor and needs proper attention for long-term device performance. Degradation issues that limit the stability and hence device performance originate from dopants and additives, i.e., 4-tert-butylpridine used in spiro-OMeTAD, which degrades $MAPbI_3$ into PbI_2 (Li et al., 2014). Similarly, deterioration of spiro-OMeTAD contact with the perovskite absorber layer upon annealing has also been reported (Malinauskas et al., 2015). Additionally, during annealing or under illumination, the reaction of ZnO with the perovskite layer exhibited deprotonation of methylammonium cations (Yang et al., 2015a). Since in single-junction PSCs, opaque metal rear electrodes were used. Research groups demonstrated strong decay in cell performance due to these rear metal electrodes. Factors affecting the device performance include degradation of perovskite absorber (hydroiodide, methylammonium iodide (MAI)) by corrosive reactions and redox reactions of perovskite absorber material with metal electrodes (Ag, Al, Au) (Zhao et al., 2016), and migration of metal particles into the organic charge transport layer (Kato et al., 2015; Domanski et al., 2016; Sanehira et al., 2016). To avoid these various interactions, transparent electrodes are considered a suitable replacement with metal electrodes due to their excellent transparency, conductivity, and chemical stability (towards reactions with many materials and possible degradation).

Moreover, the effective resistivity of TCOs against water and oxygen penetration and possible volatility of ions in the perovskite material mark them as potential candidates for Si/per TSCs (Bush et al., 2016). To avoid damaging underlying soft layers, buffer layers are used for sputtered TCO electrodes. Werner et al. (2015a,c) demonstrated thermally evaporated MoO_x as a buffer layer for efficient hole extraction. Similarly, Bush et al. (2016) reported AZO nanoparticles as an effective buffer layer for electron extraction. However, due to possible corrosive interface reaction of such layers with perovskite absorber and evaporation of many metal oxides, environmental sensitivity, and stability concerns were raised (Schulz et al., 2016; Werner et al., 2016c; Brinkmann et al., 2017; Leijtens et al., 2017; Zhao et al., 2017).

5.3.3. Thermal & environmental stability

The degradation of perovskite layer when exposed to water, oxygen, heat, and light is the main cause of stability issues for perovskite-based tandem devices. Device thermal stability is an important factor in the successful development of c-Si/per TSCs. A solar cell should be thermally stable such that it should remain stable at >100 °C annealing temperature and be able to pass damp-heat test standards. With mixed cations using FA, Cs, and Rb, better stability was reached. Bush et al. (2017) reached 23.6% efficiency using a 1.63 eV mixed cation mixed halide absorber containing FA and Cs ($Cs_{0.17}FA_{0.83}Pb(Br_{0.17}I_{0.83})_3$) with improved thermal stability. In addition, the fabricated single-junction device demonstrated stable behavior at a 1000-hours damp heat test under a temperature of 85 °C and relative humidity (RH) of 85%. Qiu et al. (2018) developed 2-T c-Si/per TSCs based on $FAMACsPbI_{3-x}Br_x$ as the top sub-cell absorber layer. The device exhibited long-term stability and retained more than 85% of original efficiency after 500 h stability test. Shen et al. (2018) demonstrated $Cs_{0.05}Rb_{0.05}FA_{0.765}MA_{0.135}PbI_{2.55}Br_{0.45}$ multi cation perovskite with bandgap of 1.63 eV in a 2-T monolithic c-Si/per TSC. The stabilized efficiencies of 22.9% and 24.1% were reported for the homojunction and passivating contact heterojunction tandems, respectively. The semitransparent PSCs maintained ∼89% of its original behavior after 1414-hours with 85 °C and 85% RH test conditions.

5.3.4. Bias dependent degradation

Bias dependent degradation is also an important factor in the PSCs and significantly affects the device performance under different bias conditions. The bias condition has an impact on the device's internal fields, current, and charge carrier accumulation. Several studies have revealed bias-dependent degradation in PSCs owing to intrinsic ion migration within the absorber layer, extrinsic ion migration, and radical formation due to electron accumulation (Khenkin et al., 2019). Ion migration can take place via interstitial ion hopping or vacancy migration. Similarly, the extrinsic ionic migration into and out of the active layer was observed in PSCs. For instance, under forward bias condition, oxygen ions released from TiO_2 promoted partial amorphization and decomposition of the absorber layer. Also, external ion migration could be destructive if absorber ions drift to the contact layers. For example, it has been demonstrated that I^- corrodes adjacent layers (Akbulatov et al., 2017). To predict the probability of metal ions infiltrating into the perovskite layer, W. Ming and fellows calculated energy barriers for the diffusion of common back electrode metals (Ming et al., 2018). They demonstrated that Ag^+, Au^+, Co^+, Cu^+, Ni^+, and Pd^+ could easily migrate into $MAPbI_3$ perovskite via interstitial sites. Domanski et al. (2018) proposed radical formation via bond breakage by collected charge carriers and investigated the effect of operating conditions on the PSCs degradation. They suggested that photo-degradation at open-circuit (OC) was higher than at short-circuit (SC) in a protective atmosphere. Likewise, Bryant et al. (2016) demonstrated a more comprehensive theory to describe the increased degradation rate at OC (under light) and forward biasing (in the dark in the air). They proposed that superoxide is formed when oxygen reacts with accumulated photo-generated electrons.

5.4. Upscaling

Developing perovskite-based TSCs at a large scale is essential for technology commercialization. At the initial level, most c-Si/per, including the 2-T and 4-T structures with record efficiencies, were developed on small active areas of typically ≤ 1 cm^2. So far, the devices that have achieved record-breaking efficiencies have been made using laboratory-scale processes such as perovskite cell spin-coating and anti-solvent dropping methods. These methods are not suitable for large-scale fabrication due to their insufficient solvent coverage, which results in low-quality pinhole perovskite layers. A transition of fabrication processes to

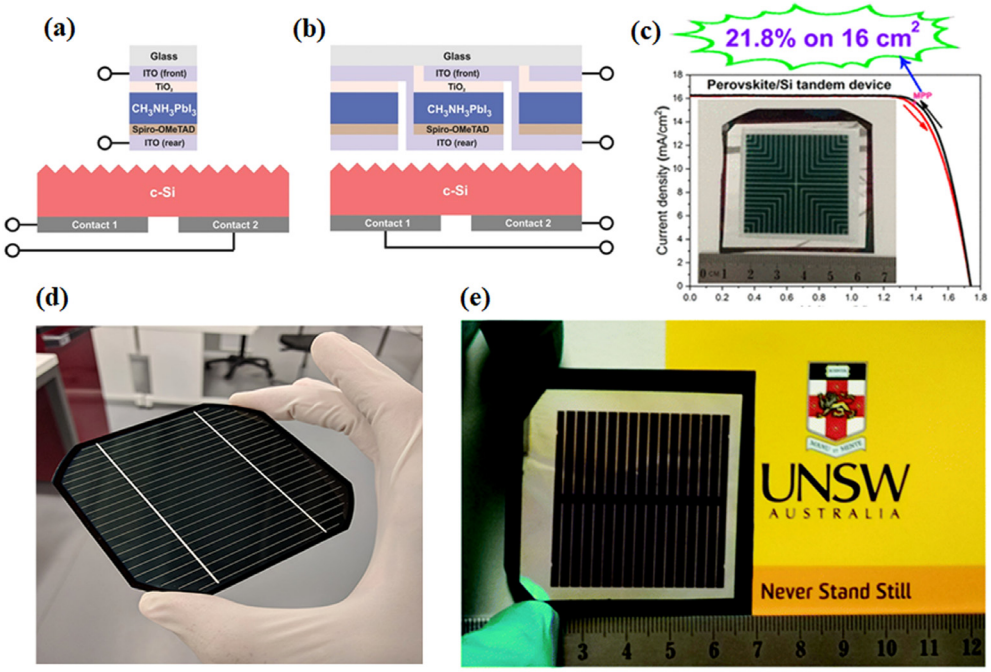

Fig. 16. Schematic diagram of the 4-T c-Si/per TSCs with p–i–n configuration based $MAPbI_3$ top sub-cell and an IBC c-Si bottom sub-cell a) cell-on-cell and b) module-on-cell architectures. Reproduced with permission Jaysankar et al. (2017). Copyright 2017, WILEY. Photos of developed c-Si/perovskite tandem devices. c) a 21.8% efficient fabricated monolithic c-Si/perovskite tandem device based on homojunction bottom silicon sub-cell. Reprinted (adapted) with permission from Zheng et al. (2018b). Copyright 2018, American Chemical Society. d) Photo of a large-area cell after being cut down to a pseudo square shape. Reprinted with permission from Kamino et al. (2019). Copyright 2019, American Chemical Society. e) A photo of a c-Si/perovskite tandem device with 16 cm^2 area, developed at the UNSW, Australia.
Source: Republished with permission of Royal Society of Chemistry, from Zheng et al. (2018a).

large-scale deposition techniques such as blade coating, solution processes, printing, and spray coating is desired to address this challenge for perovskite cells. Similarly, large-scale printing techniques such as inkjet printing, slot-die coating, and roll-to-roll printing can be utilized for large-scale perovskite solar module developments and consequently tandem technology. Thanks to continuous and dedicated research efforts, due to which, first upscaling step towards 2-T c-Si/per tandem cell of >1 cm^2 area was demonstrated by Werner et al. (2015c) in 2015, in which they reported 19.2% efficiency for 1.22 cm^2 device area. Similarly, the first report towards large-scale fabrication beyond laboratory scale was published in 2017, when Sahli et al. (2018a) demonstrated 2-T c-Si/per TSCs by employing nc-Si:H layer as a recombination junction using $Cs_{0.19}FA_{0.81}Pb(Br_{0.22}I_{0.78})_3$ perovskite layer. They achieved 18% stable efficiency for 5 × 5 cm^2 device structure with an aperture area of 12.96 cm^2. In 2017, Jaysankar et al. (2017) developed a scalable 4-T c-Si/per TSC by adopting a module-on-cell concept, where a perovskite solar module with interconnected sub-cells is combined with a Si solar cell (Zhang et al., 2015). Initially, a cell-on-cell structure with an aperture area of 0.13 cm^2 (Fig. 16 a) was developed. Later on, module-on-cell architecture was fabricated by combining a semitransparent $MAPbI_3$ perovskite solar module having an aperture area of 4 cm^2 on top of an IBC c-Si solar cell with the same area (Fig. 16 b). A total efficiency of 20.2% (12% of the perovskite module and 8.2% of an IBC silicon bottom cell) was demonstrated by mechanically stacked device. In 2018, Zheng et al. (2018a) successfully integrated a low-temperature processed planar $MAPbI_3$ PSC on a homojunction silicon solar cell in a monolithic tandem device structure (Fig. 16e). Without using an additional interface layer on large areas (4 and 16 cm^2), they achieved stabilized efficiencies of 20.5% and 17.1% for 4 cm^2 and 16 cm^2 device areas, respectively. After some time, the same group demonstrated 21.8% steady-state efficiency with a cell area of 16 cm^2 (Fig. 16c) (Zheng et al., 2018b). The year 2019 would remain considered in the history of the c-Si/per TSCs because, largest device area of 57.4 cm^2 was demonstrated by Kamino et al. (2019), in which certified PCE value of 22.6% was achieved for 2-T c-Si/per TSC using screen printing (Fig. 16d). Despite significant advancements in large-scale fabricated TSCs, their performance is still inferior to that of highly efficient c-Si/per TSCs and need proper attention.

6. Future trends in Si/PSC tandems

c-Si/per TSCs have made remarkable progress in a few years of rigorous research and have exhibited promising routes to boost the efficiency of state-of-the-art single-junction PV technologies. At laboratory scale, the certified highest efficiency of 29.80% for 2-T c-Si/per TSCs is produced using top-cell with an area of 1.016 cm^2, outperforming well-developed perovskite and silicon single-junction solar cells. The roadmap for successful commercialization at large-scale production demands consistent performance according to industrial protocols. $MAPbI_3$ based perovskites have been deployed broadly in TSCs. However, volatility and phase segregation issues limit their application towards commercialization. On the other hand, cesium and rubidium-based multiple cation perovskites have shown remarkable development in TSCs and improved the device performance, including stability. The ideal bandgap for the perovskite absorber to pair with a Si bottom cell is ∼ 1.6–1.7 eV in a tandem arrangement. Based on the comparison of reported data, the PCE in the 4-T design lags behind 2-T, requiring additional attention. The use of expensive organic charge transport materials in PSCs has long been a source of instability issues, necessitating a call for all-inorganic charge transport layers. In addition, the SHJ technology with a high Voc of up to 0.750 V could be an appropriate

choice for bottom cells in tandem design with perovskite top cells. However, the corresponding parameters of SHJ bottom cells used in tandem cells are lower than that of high-performance single-junction SHJ cells. Therefore, there is still a potential for advancement in TSCs using SHJ bottom cells.

Towards successful development and commercialization of c-Si/per TSCs, following are the few challenges that need to be addressed first for future considerations.

1. Stability
2. Light Trapping/Surface Texturing
3. Cost-effectiveness
4. Material Toxicity

6.1. Stability

Long-term stability issues are important factors requiring further studies towards the market entry of c-Si/per TSCs. Since the emergence of perovskite materials, stability has remained an important and challenging factor in PSCs. During the past few years, various research groups have shown considerable research progress based on perovskite device stability. Thanks to continuous and dedicated scientific efforts, from hundreds to thousands of hours of stability data as per standardized degradation protocols has been reported. To be compatible with crystalline silicon bottom cells in tandem configuration, top PSCs must be stable after 25–30 years. Future considerations for the long-term stability of charge transport layers and electrodes will be required by overcoming their reaction with other layers used in solar cells. A significant development related to material stability was reported after employing inorganic cations such as Cs (Beal et al., 2016; Saliba et al., 2016b; Huang et al., 2017; Syzgantseva et al., 2017) and Rb (Duong et al., 2016a,b; Saliba et al., 2016a; Duong et al., 2017; Kim et al., 2017). Cs and Rb cations-based devices maintained 95% of their initial performance after hundreds of hours of MPPT (Saliba et al., 2016a,b). When combined with MA or FA, a significant improvement in the structural stability of the perovskite absorber layer was reported. Devices based on $CsFAMAPbBr_xI_{3-x}$ absorbers exhibited thermal stability at annealing temperatures of up to 130 °C without degradation as well as enhanced resistance to photo-oxidation and moisture-induced degradation (Li et al., 2015; Bush et al., 2016; McMeekin et al., 2016; Wang et al., 2017). Therefore, $CsFAMAPbBr_xI_{3-x}$ based material could be a promising choice for thermally and environmentally stable devices.

6.2. Light trapping/surface texturing

Effective light management is a key challenge for developing efficient TSCs. Absorber materials with indirect bandgaps, such as crystalline silicon absorb weak light near their absorption edge. Light trapping strategies would have to be employed to harvest the maximum amount of light. To achieve this, texturing both interfaces of the silicon wafer is the most common strategy for c-Si solar cells. Werner et al. (2016b) have demonstrated an increase of 0.77 mA cm^{-2} current in the bottom cell for wavelength range >1000 nm by texturing the rear side of the wafer. Reports based on double-sided texturing of the bottom silicon wafer have exhibited the highest current, achieved by reduced reflection and by light trapping of infrared light in the bottom cell. However, the deposition of solution-processed perovskite layers on top of textured surfaces is crucial and needs proper attention from the research community.

6.3. Cost-effectiveness

c-Si/per TSCs will exhibit their economic superiority over single-junction solar cells provided the gains in their efficiency override the cost required for additional fabrication steps, the balance of systems, and power electronics. Techno-economic analyses for the Si/per tandem technology reveal a > ≈15% relative boost in efficiency, suggesting the ability of this design to reduce the cost per watt peak (W_p) at the module level. There is an added value to a higher-efficiency module as a 4% absolute increase in module efficiency can reduce the area-related balance-of-systems costs by ∼US$0.03 per W_p and US$0.06 per W_p for utility-scale and rooftop solar installations, respectively (Leijtens et al., 2018; Werner et al., 2018). With over 26% efficiency offered by single-junction Si solar cells, c-Si/per tandem will have to demonstrate over 30% efficiencies as a remarkable cost-competitive candidate in the PV market. Factors influencing the overall cost of c-Si/per tandem technology at a large scale include materials cost (perovskites, electrodes, and expensive HTLs), fabrication cost, encapsulation cost, etc. Cost related to polished bottom silicon wafers is another important issue and needs attention. So, reduced cost factors should be considered for large-scale tandem device fabrication. With the prosperous development of c-Si/per tandem in recent years, we believe that the commercialization of this field, which provides one of the most promising approaches to produce cheaper solar electricity, can be obtained in the near future.

6.4. Encapsulation and reliability testing

Reliable encapsulation schemes such as glass/glass encapsulation by a polymer encapsulant and a butyl rubber or polyisobutylene edge sealant (for which thermal stability of at least ≈ 120–160 °C is a requirement) would need to be employed. Additionally, towards the market entry, Si/per TSCs will have to qualify reliability protocols as per IEC standards, such as damp heat test at (1000 h at 85% relative humidity and 85 °C) (Bush et al., 2017), thermal cycling (–40 °C to 85 °C, 200 cycles) (Cheacharoen et al., 2018), and extended light soaking tests at 1 sun illumination. Furthermore, an efficient encapsulation that preserves all by-products of degradation is essential.

6.5. Material toxicity

In perovskites, material toxicity, particularly of lead (Pb) content, is another serious issue towards a sustainable and lead-free environment. Concerns over environmentally friendly perovskite composition need further detailed investigation towards commercialization of Si/per tandem technology on a large scale. Therefore, research towards lead-free or lead-less PSCs has already started, although device efficiencies still lie far behind those of state-of-the-art lead-containing compounds. Various potential materials such as tin (Sn) and bismuth (Bi) have been employed to replace Pb. However, on one side, Sn-based PCSs exhibit high J_{sc} of around 20 to 25 mA cm^{-2} due to their low bandgaps, but on the other side, their V_{oc} of about 0.5 V is low compared to that of 1.1 V of Pb based counterparts. The reason behind this low V_{oc} is due to heavy p-type doping, attributed to facile and undesirable oxidization of Sn^{2+} to Sn^{4+} due to poor chemical stability (Ke and Kanatzidis, 2019). Similarly, Bi-based perovskites demonstrated low efficiencies due to small J_{sc} values; these low J_{sc} values were attributed to the lack of a continuous structural network (Yang et al., 2017). Therefore, encapsulating Pb-based PSCs is essential for reducing overall environmental impact and preventing Pb leakage.

7. Concluding remarks

Over the past few years, the combination of perovskite solar cells (PSCs) with crystalline silicon solar cells in tandem configuration has shown tremendous performance towards cost-effective solar to electricity conversion. This tandem technology has demonstrated the potential to achieve the theoretical S–Q limit of single-junction silicon solar cells with an additional moderate cost. Efficiency values are improving with developments in 2-T and 4-T c-Si/per TSCs. In just a few years, over 29 and 28% efficiencies at laboratory scale have been reported for 2-T and 4-T c-Si/per TSCs, respectively. Thanks to continuous and dedicated research efforts, light management strategies have been developed to overcome losses related to light reflection and boost the harvesting of light efficiency. Furthermore, with the emergence of new materials and the composition of perovskite absorber layers, stability is also improving. As a result, many devices have passed the stability test and standardized protocols as prescribed by Electrotechnical Commission (IEC). However, the stability of PSCs is still far behind those of bottom silicon solar cells. Therefore, further development is required to address issues related to the stability of PSCs to justify 25-year warranties according to industrial standards protocols. In addition, large-scale devices have been fabricated by employing solution-processable techniques such as screen printing, ink-jet printing, slot-die coating, and blade-coating. Similarly, the toxicity problem in PSCs is also gaining considerable research focus. Though, a few gaps are present which need proper attention to enhance the overall performance of tandem structures and their successful entry into the PV market. We believe that with devoted research efforts, c-Si/per TSC technology will lead the future of PV technology in the years to come.

CRediT authorship contribution statement

Ehsan Raza: Data curation, Formal analysis, Writing - original draft, Writing - review & editing, Validation, Methodology, Software. **Zubair Ahmad:** Conceptualization, Funding acquisition, Formal analysis, Methodology, Project administration, Supervision, Validation, Writing - review & editing.

Declaration of competing interest

The authors declare that they have no known competing financial interests or personal relationships that could have appeared to influence the work reported in this paper.

Acknowledgments

This work was supported by the National Priorities Research Program under grant No. [NPRP11S-1210–170080] from the Qatar National Research Fund (a member of the Qatar Foundation). The findings made herein are solely the responsibility of the authors. The article processing charges (APCs) are funded by the Qatar National Library, Qatar.

References

Ahmad, W., et al., 2017. Inorganic CsPbI3 perovskite-based solar cells: A choice for a tandem device. Solar RRL 1 (7), 1700048.
Ahn, J., et al., 2017. Metal-nanowire-electrode-based perovskite solar cells: Challenging issues and new opportunities. Adv. Energy Mater. 7 (15), 1602751.
Akbulatov, A.F., et al., 2017. Effect of electron-transport material on light-induced degradation of inverted planar junction perovskite solar cells. Adv. Energy Mater. 7 (19), 1700476.
Al-Ashouri, A., et al., 2020. Monolithic perovskite/silicon tandem solar cell with> 29% efficiency by enhanced hole extraction. Science 370 (6522), 1300–1309.
Albrecht, S., et al., 2016. Monolithic perovskite/silicon-heterojunction tandem solar cells processed at low temperature. Energy Environ. Sci. 9 (1), 81–88.
Alharbi, F.H., Kais, S., 2015. Theoretical limits of photovoltaics efficiency and possible improvements by intuitive approaches learned from photosynthesis and quantum coherence. Renew. Sustain. Energy Rev. 43, 1073–1089.
Bailie, C.D., et al., 2015. Semi-transparent perovskite solar cells for tandems with silicon and CIGS. Energy Environ. Sci. 8 (3), 956–963.
Barker, A.J., et al., 2017. Defect-assisted photoinduced halide segregation in mixed-halide perovskite thin films. ACS Energy Lett. 2 (6), 1416–1424.
Battaglia, C., et al., 2016. High-efficiency crystalline silicon solar cells: status and perspectives. Energy Environ. Sci. 9 (5), 1552–1576.
Beal, R.E., et al., 2016. Cesium lead halide perovskites with improved stability for tandem solar cells. J. Phys. Chem. Lett. 7 (5), 746–751.
Belisle, R.A., et al., 2016. Minimal effect of the hole-transport material ionization potential on the open-circuit voltage of perovskite solar cells. ACS Energy Lett. 1 (3), 556–560.
Bett, A.J., et al., 2019. Two-terminal perovskite silicon tandem solar cells with a high-Bandgap perovskite absorber enabling voltages over 1.8 V. Progress in photovoltaics: research and applications.
Boccard, M., Ballif, C., 2020. Influence of the subcell properties on the fill factor of two-terminal perovskite–silicon tandem solar cells. ACS Energy Lett. 5 (4), 1077–1082.
Bowman, A.R., et al., 2021. Relaxed current matching requirements in highly luminescent perovskite tandem solar cells and their fundamental efficiency limits. ACS Energy Lett. 6 (2), 612–620.
Brinkmann, K., et al., 2017. Suppressed decomposition of organometal halide perovskites by impermeable electron-extraction layers in inverted solar cells. Nature Commun. 8 (13938).
Brunetti, B., et al., 2016. On the thermal and thermodynamic (in) stability of methylammonium lead halide perovskites. Sci. Rep. 6 (31896).
Bryant, D., et al., 2016. T. Chotchunang atchaval, S. Wheeler, JR Durrant, SA Haque. Energy Environ. Sci. 9, 1655.
Bush, K.A., et al., 2016. Thermal and environmental stability of semi-transparent perovskite solar cells for tandems enabled by a solution-processed nanoparticle buffer layer and sputtered ITO electrode. Adv. Mater. 28 (20), 3937–3943.
Bush, K.A., et al., 2017. 23.6%-Efficient monolithic perovskite/silicon tandem solar cells with improved stability. Nat. Energy 2 (4), 17009.
Bush, K.A., et al., 2018. Minimizing current and voltage losses to reach 25% efficient monolithic two-terminal perovskite–silicon tandem solar cells. ACS Energy Lett. 3 (9), 2173–2180.
Cariou, R., et al., 2018. Iii–V-on-silicon solar cells reaching 33% photoconversion efficiency in two-terminal configuration. Nat. Energy 3 (4), 326–333.
Cheacharoen, R., et al., 2018. Design and understanding of encapsulated perovskite solar cells to withstand temperature cycling. Energy Environ. Sci. 11 (1), 144–150.
Chen, B., et al., 2016. Efficient semitransparent perovskite solar cells for 23.0%-efficiency perovskite/silicon four-terminal tandem cells. Adv. Energy Mater. 6 (19), 1601128.
Chen, Z., et al., 2018. Methylammonium, formamidinium and ethylenediamine mixed triple-cation perovskite solar cells with high efficiency and remarkable stability. J. Mater. Chem. A 6 (36), 17625–17632.
Chen, B., et al., 2019. Grain engineering for perovskite/silicon monolithic tandem solar cells with efficiency of 25.4%. Joule 3 (1), 177–190.
Chen, B., et al., 2020. Blade-coated perovskites on textured silicon for 26%-efficient monolithic perovskite/silicon tandem solar cells. Joule.
Chu, Q.-Q., et al., 2019. Highly stable carbon-based perovskite solar cell with a record efficiency of over 18% via hole transport engineering. J. Mater. Sci. Technol. 35 (6), 987–993.
Conings, B., et al., 2015. Intrinsic thermal instability of methylammonium lead trihalide perovskite. Adv. Energy Mater. 5 (15), 1500477.
De Bastiani, M., et al., 2021. Efficient bifacial monolithic perovskite/silicon tandem solar cells via bandgap engineering. Nat. Energy 6 (2), 167–175.
De Wolf, S., et al., 2012. High-efficiency silicon heterojunction solar cells: A review. Green 2 (1), 7–24.
Descoeudres, A., et al., 2020. The versatility of passivating carrier-selective silicon thin films for diverse high-efficiency screen-printed heterojunction-based solar cells. Prog. Photovolt., Res. Appl. 28 (6), 569–577.
Dewi, H.A., et al., 2019a. Four-terminal perovskite on silicon tandem solar cells optimal measurements schemes. Energy Technol..
Dewi, H.A., et al., 2019b. Highly efficient semitransparent perovskite solar cells for four terminalPerovskite-silicon tandems. ACS Appl. Mater. Interfaces 11 (37), 34178–34187.
Domanski, K., et al., 2016. Not all that glitters is gold: metal-migration-induced degradation in perovskite solar cells. ACS Nano 10 (6), 6306–6314.
Domanski, K., et al., 2018. Systematic investigation of the impact of operation conditions on the degradation behaviour of perovskite solar cells. Nat. Energy 3 (1), 61–67.
Duong, T., et al., 2016a. Semitransparent perovskite solar cell with sputtered front and rear electrodes for a four-terminal tandem. IEEE J. Photovolt. 6 (3), 679–687.

Duong, T., et al., 2016b. Structural engineering using rubidium iodide as a dopant under excess lead iodide conditions for high efficiency and stable perovskites. Nano Energy 30, 330–340.
Duong, T., et al., 2017. Rubidium multication perovskite with optimized bandgap for perovskite-silicon tandem with over 26% efficiency. Adv. Energy Mater. 7 (14), 1700228.
Duong, T., et al., 2020. High efficiency perovskite-silicon tandem solar cells: Effect of surface coating versus bulk incorporation of 2D perovskite. Adv. Energy Mater. 10 (9), 1903553.
Dupre, O., et al., 2018. Field performance versus standard test condition efficiency of tandem solar cells and the singular case of perovskites/silicon devices. J. Phys. Chem. Lett. 9 (2), 446–458.
Eperon, G.E., et al., 2014. Formamidinium lead trihalide: a broadly tunable perovskite for efficient planar heterojunction solar cells. Energy Environ. Sci. 7 (3), 982–988.
Escarré, J., et al., 2012. Geometric light trapping for high efficiency thin film silicon solar cells. Sol. Energy Mater. Sol. Cells 98, 185–190.
Essig, S., et al., 2017. Raising the one-sun conversion efficiency of III–V/si solar cells to 32.8% for two junctions and 35.9% for three junctions. Nat. Energy 2 (9), 17144.
Fan, R., et al., 2017. towards full solution processed perovskite/si monolithic tandem solar device with PCE exceeding 20%. Solar RRL 1 (11), 1700149.
Franklin, E., et al., 2016. Design, fabrication and characterisation of a 24.4% efficient interdigitated back contact solar cell. Prog. Photovolt., Res. Appl. 24 (4), 411–427.
Frolova, L.A., et al., 2016. Highly efficient all-inorganic planar heterojunction perovskite solar cells produced by thermal coevaporation of CsI and PbI2. J. Phys. Chem. Lett. 8 (1), 67–72.
Fu, F., et al., 2015. Low-temperature-processed efficient semi-transparent planar perovskite solar cells for bifacial and tandem applications. Nature Commun. 6 (8932).
Fu, F., et al., 2016. High-efficiency inverted semi-transparent planar perovskite solar cells in substrate configuration. Nat. Energy 2 (1), 16190.
Gharibzadeh, S., et al., 2020. 2D/3D heterostructure for semitransparent perovskite solar cells with engineered bandgap enables efficiencies exceeding 25% in four-terminal tandems with silicon and CIGS. Adv. Funct. Mater. 30 (19), 1909919.
Glunz, S., et al., 2001. Minority carrier lifetime degradation in boron-doped Czochralski silicon. J. Appl. Phys. 90 (5), 2397–2404.
Grant, D., et al., 2016. Design guidelines for perovskite/silicon 2-terminal tandem solar cells: an optical study. Opt. Express 24 (22), A1454–A1470.
Green, M.A., 2016. Commercial progress and challenges for photovoltaics. Nat. Energy 1 (1), 1–4.
Guo, F., et al., 2015. High-performance semitransparent perovskite solar cells with solution-processed silver nanowires as top electrodes. Nanoscale 7 (5), 1642–1649.
Haug, F.-J., Ballif, C., 2015. Light management in thin film silicon solar cells. Energy Environ. Sci. 8 (3), 824–837.
Herz, L.M., 2017. Charge-carrier mobilities in metal halide perovskites: fundamental mechanisms and limits. ACS Energy Lett. 2 (7), 1539–1548.
Hoke, E.T., et al., 2015. Reversible photo-induced trap formation in mixed-halide hybrid perovskites for photovoltaics. Chem. Sci. 6 (1), 613–617.
Holman, Z.C., et al., 2012. Current losses at the front of silicon heterojunction solar cells. IEEE J. Photovolt. 2 (1), 7–15.
Hossain, M.I., et al., 2018. Nanophotonic design of perovskite/silicon tandem solar cells. J. Mater. Chem. A 6 (8), 3625–3633.
Hossain, M.I., et al., 2019. Perovskite/silicon tandem solar cells: from detailed balance limit calculations to photon management. Nano-Micro Lett. 11 (1), 58.
Hou, F., et al., 2019a. Inverted pyramidally-textured PDMS antireflective foils for perovskite/silicon tandem solar cells with flat top cell. Nano Energy 56, 234–240.
Hou, F., et al., 2019b. Monolithic perovskite/silicon-heterojunction tandem solar cells with open-circuit voltage of over 1.8 V. ACS Appl. Energy Mater. 2 (1), 243–249.
Huang, J., et al., 2017. Sequential introduction of cations deriving large-grain CsxFA1- xPbI3 thin film for planar hybrid solar cells: Insight into phase-segregation and thermal-healing behavior. Small 13 (10), 1603225.
Jäger, K., et al., 2017. Numerical optical optimization of monolithic planar perovskite-silicon tandem solar cells with regular and inverted device architectures. Opt. Express 25 (12), A473–A482.
Jäger, K., et al., 2021. Perovskite/silicon tandem solar cells: Effect of luminescent coupling and bifaciality. Solar RRL 5 (3), 2000628.
Jaysankar, M., et al., 2017. Four-terminal perovskite/silicon multijunction solar modules. Adv. Energy Mater. 7 (15), 1602807.
Jaysankar, M., et al., 2018. Minimizing voltage loss in wide-bandgap perovskites for tandem solar cells. ACS Energy Lett. 4 (1), 259–264.
Jeong, J., et al., 2021. Pseudo-halide anion engineering for α-FAPbI 3 perovskite solar cells. Nature 592 (7854), 381–385.
Jošt, M., et al., 2017. Efficient light management by textured nanoimprinted layers for perovskite solar cells. ACS Photon. 4 (5), 1232–1239.
Jošt, M., et al., 2018. Textured interfaces in monolithic perovskite/silicon tandem solar cells: advanced light management for improved efficiency and energy yield. Energy Environ. Sci. 11 (12), 3511–3523.
Jošt, M., et al., 2020. Monolithic perovskite tandem solar cells: A review of the present status and advanced characterization methods towards 30% efficiency. Adv. Energy Mater. 1904102.
Jung, J.W., et al., 2015. High-performance semitransparent perovskite solar cells with 10% power conversion efficiency and 25% average visible transmittance based on transparent CuSCN as the hole-transporting material. Adv. Energy Mater. 5 (17), 1500486.
Kamino, B.A., et al., 2019. Low-temperature screen-printed metallization for the scale-up of two-terminal perovskite–silicon tandems. ACS Appl. Energy Mater..
Kanda, H., et al., 2016. Interface optoelectronics engineering for mechanically stacked tandem solar cells based on perovskite and silicon. ACS Appl. Mater. Interfaces 8 (49), 33553–33561.
Kanda, H., et al., 2018. Effect of silicon surface for perovskite/silicon tandem solar cells: flat or textured? ACS Appl. Mater. Interfaces 10 (41), 35016–35024.
Kato, Y., et al., 2015. Silver iodide formation in methyl ammonium lead iodide perovskite solar cells with silver top electrodes. Adv. Mater. Interfaces 2 (13), 1500195.
Ke, W., Kanatzidis, M.G., 2019. Prospects for low-toxicity lead-free perovskite solar cells. Nature Commun. 10 (1), 965.
Ke, W., et al., 2015. Efficient fully-vacuum-processed perovskite solar cells using copper phthalocyanine as hole selective layers. J. Mater. Chem. A 3 (47), 23888–23894.
Khenkin, M.V., et al., 2019. Bias-dependent degradation of various solar cells: lessons for stability of perovskite photovoltaics. Energy Environ. Sci. 12 (2), 550–558.
Kim, J., et al., 2017. Overcoming the challenges of large-area high-efficiency perovskite solar cells. ACS Energy Lett. 2 (9), 1978–1984.
Kim, C.U., et al., 2019. Optimization of device design for low cost and high efficiency planar monolithic perovskite/silicon tandem solar cells. Nano Energy 60, 213–221.
Kim, D., et al., 2020. Efficient, stable silicon tandem cells enabled by anion-engineered wide-bandgap perovskites. Science 368 (6487), 155–160.
Köhnen, E., et al., 2019. Highly efficient monolithic perovskite silicon tandem solar cells: analyzing the influence of current mismatch on device performance. Sustain Energy Fuels.
Köhnen, E., et al., 2021. 27.9% Efficient monolithic perovskite/silicon tandem solar cells on industry compatible bottom cells. Solar RRL 5 (7), 2100244.
Kojima, A., et al., 2009. Organometal halide perovskites as visible-light sensitizers for photovoltaic cells. J. Am. Chem. Soc. 131 (17), 6050–6051.
Lamanna, E., et al., 2020. Mechanically stacked, two-terminal graphene-based perovskite/silicon tandem solar cell with efficiency over 26%. Joule 4 (4), 865–881.
Lang, F., et al., 2015. Perovskite solar cells with large-area CVD-graphene for tandem solar cells. J. Phys. Chem. Lett. 6 (14), 2745–2750.
Lee, S.-W., et al., 2016. Uv degradation and recovery of perovskite solar cells. Sci. Rep. 6 (1), 1–10.
Leguy, A.M., et al., 2016. Experimental and theoretical optical properties of methylammonium lead halide perovskites. Nanoscale 8 (12), 6317–6327.
Leijtens, T., et al., 2017. Towards enabling stable lead halide perovskite solar cells; interplay between structural, environmental, and thermal stability. J. Mater. Chem. A 5 (23), 11483–11500.
Leijtens, T., et al., 2018. Opportunities and challenges for tandem solar cells using metal halide perovskite semiconductors. Nat. Energy 3 (10), 828–838.
Li, W., et al., 2014. Montmorillonite as bifunctional buffer layer material for hybrid perovskite solar cells with protection from corrosion and retarding recombination. J. Mater. Chem. A 2 (33), 13587–13592.
Li, Z., et al., 2015. Stabilizing perovskite structures by tuning tolerance factor: formation of formamidinium and cesium lead iodide solid-state alloys. Chem. Mater. 28 (1), 284–292.
Li, Y., et al., 2017. Reflective perovskite solar cells for efficient tandem applications. J. Mater. Chem. C 5 (1), 134–139.
Lin, Y., et al., 2017. Matching charge extraction contact for wide-bandgap perovskite solar cells. Adv. Mater. 29 (26), 1700607.
Lipovšek, B., et al., 2018. Microtextured light-management foils and their optimization for planar organic and perovskite solar cells. IEEE J. Photovolt. 8 (3), 783–792.
Liu, J., et al., 2016. Identification and mitigation of a critical interfacial instability in perovskite solar cells employing copper thiocyanate hole-transporter. Adv. Mater. Interfaces 3 (22), 1600571.
Liu, J., et al., 2021. 28.2%-Efficient, outdoor-stable perovskite/silicon tandem solar cell. Joule 5 (12), 3169–3186.
Löper, P., et al., 2015. Organic–inorganic halide perovskite/crystalline silicon four-terminal tandem solar cells. Phys. Chem. Chem. Phys. 17 (3), 1619–1629.
Macdonald, D., Geerligs, L., 2004. Recombination activity of interstitial iron and other transition metal point defects in p-and n-type crystalline silicon. Appl. Phys. Lett. 85 (18), 4061–4063.

Mailoa, J.P., et al., 2015. A 2-terminal perovskite/silicon multijunction solar cell enabled by a silicon tunnel junction. Appl. Phys. Lett. 106 (12), 121105.
Malinauskas, T., et al., 2015. Enhancing thermal stability and lifetime of solid-state dye-sensitized solar cells via molecular engineering of the hole-transporting material spiro-OMeTAD. ACS Appl. Mater. Interfaces 7 (21), 11107–11116.
Manzoor, S., et al., 2017. Improved light management in planar silicon and perovskite solar cells using PDMS scattering layer. Sol. Energy Mater. Sol. Cells 173, 59–65.
Mazzarella, L., et al., 2019. Infrared light management using a nanocrystalline silicon oxide interlayer in monolithic perovskite/silicon heterojunction tandem solar cells with efficiency above 25%. Adv. Energy Mater. 9 (14), 1803241.
McMeekin, D.P., et al., 2016. A mixed-cation lead mixed-halide perovskite absorber for tandem solar cells. Science 351 (6269), 151–155.
Ming, W., et al., 2018. Formation and diffusion of metal impurities in perovskite solar cell material CH3NH3PbI3, implications on solar cell degradation and choice of electrode. Adv. Sci. 5 (2), 1700662.
Miyano, K., et al., 2016. Hysteresis, stability, and ion migration in lead halide perovskite photovoltaics. J. Phys. Chem. Lett. 7 (12), 2240–2245.
Momblona, C., et al., 2016. Efficient vacuum deposited pin and nip perovskite solar cells employing doped charge transport layers. Energy Environ. Sci. 9 (11), 3456–3463.
Nagashima, T., et al., 2000. Three-terminal tandem solar cells with a back-contact type bottom cell. In: Conference Record of the Twenty-Eighth IEEE Photovoltaic Specialists Conference-2000 (Cat. No. 00CH37036). IEEE.
Nogay, G., et al., 2019. 25.1%-Efficient monolithic perovskite/silicon tandem solar cell based on ap-type monocrystalline textured silicon wafer and high-temperature passivating contacts. ACS Energy Lett. 4 (4), 844–845.
NREL, N., 2019. Best research-cell efficiency chart.
NREL, 2021. https://www.nrel.gov/pv/assets/pdfs/cell-pv-eff-emergingpv-rev211214.pdf.
Park, I.J., et al., 2019. A three-terminal monolithic perovskite/si tandem solar cell characterization platform. Joule 3 (3), 807–818.
Peng, J., et al., 2017. Efficient indium-doped TiOx electron transport layers for high-performance perovskite solar cells and perovskite-silicon tandems. Adv. Energy Mater. 7 (4), 1601768.
Pujari, N.S., et al., 2018. International Technology Roadmap for Photovoltaic (ITRPV) Results 2017 Including Maturity Report, 2018 Ninth Edition 2018 ITRPV.
PV, O., 2018. https://www.oxfordpv.com/news/oxford-pv-perovskite-solar-cell-achieves-28-efficiency.
PV, O., 2020. https://www.oxfordpv.com/sites/default/files/2020-12/Oxford%20PV%20hits%20new%20world%20record%2021%20December%202020.pdf.
Qiu, Z., et al., 2018. Monolithic perovskite/si tandem solar cells exceeding 22% efficiency via optimizing top cell absorber. Nano Energy 53, 798–807.
Quiroz, C.O.R., et al., 2018. Balancing electrical and optical losses for efficient 4-terminal si–perovskite solar cells with solution processed percolation electrodes. J. Mater. Chem. A 6 (8), 3583–3592.
Rau, U., et al., 2014. Thermodynamics of light management in photovoltaic devices. Phys. Rev. B 90 (3), 035211.
Rehman, W., et al., 2015. Charge-carrier dynamics and mobilities in formamidinium lead mixed-halide perovskites. Adv. Mater. 27 (48), 7938–7944.
Richter, A., et al., 2013. Reassessment of the limiting efficiency for crystalline silicon solar cells. IEEE J. Photovolt. 3 (4), 1184–1191.
Rohatgi, A., et al., 2020. 26.7% Efficient 4-terminal perovskite–silicon tandem solar cell composed of a high-performance semitransparent perovskite cell and a doped poly-Si/Siox passivating contact silicon cell. IEEE J. Photovolt..
Sahin, A.D., et al., 2007. Thermodynamic analysis of solar photovoltaic cell systems. Sol. Energy Mater. Sol. Cells 91 (2–3), 153–159.
Sahli, F., et al., 2018a. Improved optics in monolithic perovskite/silicon tandem solar cells with a nanocrystalline silicon recombination junction. Adv. Energy Mater. 8 (6), 1701609.
Sahli, F., et al., 2018b. Fully textured monolithic perovskite/silicon tandem solar cells with 25.2% power conversion efficiency. Nature Mater. 17 (9), 820.
Saliba, M., et al., 2016a. Incorporation of rubidium cations into perovskite solar cells improves photovoltaic performance. Science 354 (6309), 206–209.
Saliba, M., et al., 2016b. Cesium-containing triple cation perovskite solar cells: improved stability, reproducibility and high efficiency. Energy Environ. Sci. 9 (6), 1989–1997.
Sanehira, E.M., et al., 2016. Influence of electrode interfaces on the stability of perovskite solar cells: reduced degradation using MoO x/Al for hole collection. ACS Energy Lett. 1 (1), 38–45.
Santbergen, R., et al., 2016. Minimizing optical losses in monolithic perovskite/c-Si tandem solar cells with a flat top cell. Opt. Express 24 (18), A1288–A1299.
Santbergen, R., et al., 2019. Optimization of three-terminal perovskite/silicon tandem solar cells. IEEE J. Photovolt. 9 (2), 446–451.
Schulz, P., et al., 2016. High-work-function molybdenum oxide hole extraction contacts in hybrid organic–inorganic perovskite solar cells. ACS Appl. Mater. Interfaces 8 (46), 31491–31499.
Schulze, P.S., et al., 2020. 25.1% High-efficient monolithic perovskite silicon tandem solar cell with a high band gap perovskite absorber. Solar RRL.
Science, W.o., 2021. Web of science search for 'perovskite solar cells' in the title.
Shanmugam, N., et al., 2020. Anti-reflective coating materials: A holistic review from PV perspective. Energies 13 (10), 2631.
Shen, H., et al., 2018. In situ recombination junction between p-Si and TiO2 enables high-efficiency monolithic perovskite/Si tandem cells. Sci. Adv. 4 (12), eaau9711.
Shockley, W., Queisser, H.J., 1961. Detailed balance limit of efficiency of p–n junction solar cells. J. Appl. Phys. 32 (3), 510–519.
Slotcavage, D., et al., 2016. ACS Energy Lett. 1, 1199.
Söderström, T., et al., 2009. Asymmetric intermediate reflector for tandem micromorph thin film silicon solar cells. Appl. Phys. Lett. 94 (6), 063501.
Stranks, S.D., et al., 2013. Electron–hole diffusion lengths exceeding 1 micrometer in an organometal trihalide perovskite absorber. Science 342 (6156), 341–344.
Syzgantseva, O.A., et al., 2017. Stabilization of the perovskite phase of formamidinium lead triiodide by methylammonium, Cs, and/or Rb doping. J. Phys. Chem. Lett. 8 (6), 1191–1196.
Taguchi, M., et al., 2013. 24.7% Record efficiency HIT solar cell on thin silicon wafer. IEEE J. Photovolt. 4 (1), 96–99.
Tao, Y., Rohatgi, A., 2017. High-efficiency front junction n-type crystalline silicon solar cells. Nanostruct. Solar Cells 93.
Tress, W., 2017. Perovskite solar cells on the way to their radiative efficiency limit–Insights into a success story of high open-circuit voltage and low recombination. Adv. Energy Mater. 7 (14), 1602358.
Unger, E., et al., 2017. Roadmap and roadblocks for the band gap tunability of metal halide perovskites. J. Mater. Chem. A 5 (23), 11401–11409.
Uzu, H., et al., 2015. High efficiency solar cells combining a perovskite and a silicon heterojunction solar cells via an optical splitting system. Appl. Phys. Lett. 106 (1), 013506.
Wang, Z., et al., 2017. S. vanReenen, k. Wojciechowski, JB Patel, MB Johnston and HJ Snaith. Adv. Mater 29, 1604186.
Wang, Z., et al., 2019. 27%-Efficiency four-terminal perovskite/silicon tandem solar cells by sandwiched gold nanomesh. Adv. Funct. Mater..
Werner, J., et al., 2015a. Sputtered rear electrode with broadband transparency for perovskite solar cells. Sol. Energy Mater. Sol. Cells 141, 407–413.
Werner, J., et al., 2015b. Towards ultra-high efficient photovoltaics with perovskite/crystalline silicon tandem devices. In: 31st European Photovoltaic Solar Energy Conference and Exhibition.
Werner, J., et al., 2015c. Efficient monolithic perovskite/silicon tandem solar cell with cell area > 1 cm2. J. Phys. Chem. Lett. 7 (1), 161–166.
Werner, J., et al., 2016a. Zinc tin oxide as high-temperature stable recombination layer for mesoscopic perovskite/silicon monolithic tandem solar cells. Appl. Phys. Lett. 109 (23), 233902.
Werner, J.r.m., et al., 2016b. Efficient near-infrared-transparent perovskite solar cells enabling direct comparison of 4-terminal and monolithic perovskite/silicon tandem cells. ACS Energy Lett. 1 (2), 474–480.
Werner, J.r.m., et al., 2016c. Parasitic absorption reduction in metal oxide-based transparent electrodes: application in perovskite solar cells. ACS Appl. Mater. Interfaces 8 (27), 17260–17267.
Werner, J., et al., 2018. Perovskite/silicon tandem solar cells: Marriage of convenience or true love story?–an overview. Adv. Mater. Interfaces 5 (1).
Wu, Y., et al., 2017. Monolithic perovskite/silicon-homojunction tandem solar cell with over 22% efficiency. Energy Environ. Sci. 10 (11), 2472–2479.
Xu, J., et al., 2020a. Triple-halide wide–band gap perovskites with suppressed phase segregation for efficient tandems. Science 367 (6482), 1097–1104.
Xu, Q., et al., 2020b. Light management in monolithic perovskite/silicon tandem solar cells. Solar RRL 4 (2), 1900206.
Yamaguchi, M., et al., 2018. A review of recent progress in heterogeneous silicon tandem solar cells. J. Phys. D: Appl. Phys. 51 (13), 133002.
Yang, J., et al., 2015a. Origin of the thermal instability in CH3NH3PbI3 thin films deposited on ZnO. Chem. Mater. 27 (12), 4229–4236.
Yang, Y., et al., 2015b. Multilayer transparent top electrode for solution processed perovskite/Cu (In, Ga)(Se, S) 2 four terminal tandem solar cells. ACS Nano 9 (7), 7714–7721.
Yang, S., et al., 2017. Recent advances in perovskite solar cells: efficiency, stability and lead-free perovskite. J. Mater. Chem. A 5 (23), 11462–11482.
Yang, D., et al., 2021. 28.3%-Efficiency perovskite/silicon tandem solar cell by optimal transparent electrode for high efficient semitransparent top cell. Nano Energy 84, 105934.
Yoshikawa, K., et al., 2017a. Silicon heterojunction solar cell with interdigitated back contacts for a photoconversion efficiency over 26%. Nat. Energy 2 (5), 17032.
Yoshikawa, K., et al., 2017b. Exceeding conversion efficiency of 26% by heterojunction interdigitated back contact solar cell with thin film Si technology. Sol. Energy Mater. Sol. Cells 173, 37–42.
You, P., et al., 2015. Efficient semitransparent perovskite solar cells with graphene electrodes. Adv. Mater. 27 (24), 3632–3638.

Yuan, Y., Huang, J., 2016. Ion migration in organometal trihalide perovskite and its impact on photovoltaic efficiency and stability. Acc. Chem. Res. 49 (2), 286–293.
Zhang, D., et al., 2015. Design of 4-terminal solar modules combining thin-film wide-bandgap top cells and c-Si bottom cells. Energy Procedia 77, 500–507.
Zhang, D., et al., 2018. High efficiency 4-terminal perovskite/c-Si tandem cells. Sol. Energy Mater. Sol. Cells 188, 1–5.
Zhao, J., et al., 1999. 24 · 5% Efficiency silicon PERT cells on MCZ substrates and 24 · 7% efficiency PERL cells on FZ substrates. Prog. Photovolt., Res. Appl. 7 (6), 471–474.
Zhao, L., et al., 2016. Redox chemistry dominates the degradation and decomposition of metal halide perovskite optoelectronic devices. ACS Energy Lett. 1 (3), 595–602.
Zhao, J., et al., 2017. Self-encapsulating thermostable and air-resilient semitransparent perovskite solar cells. Adv. Energy Mater. 7 (14), 1602599.
Zheng, J., et al., 2018a. Large area efficient interface layer free monolithic perovskite/homo-junction-silicon tandem solar cell with over 20% efficiency. Energy Environ. Sci. 11 (9), 2432–2443.
Zheng, J., et al., 2018b. 21.8% Efficient monolithic perovskite/homo-junction-silicon tandem solar cell on 16 cm2. ACS Energy Lett. 3 (9), 2299–2300.
Zheng, J., et al., 2019. Large area 23%-efficient monolithic perovskite/homo-junction-silicon tandem solar cell with enhanced UV stability using down-shifting material. ACS Energy Lett..
Zhengshan, J.Y., et al., 2015. PVMirror: a new concept for tandem solar cells and hybrid solar converters. IEEE J. Photovolt. 5 (6), 1791–1799.
Zhu, S., et al., 2018a. Solvent engineering to balance light absorbance and transmittance in perovskite for tandem solar cells. Solar RRL 2 (11), 1800176.
Zhu, S., et al., 2018b. Transparent electrode for monolithic perovskite/silicon-heterojunction two-terminal tandem solar cells. Nano Energy 45, 280–286.